Title
Nonlinear Optical Spectroscopy of Ions at Aqueous Interfaces

Author
Devlin, Shane William

Publication Date
2023

Peer reviewed|Thesis/dissertation

Nonlinear Optical Spectroscopy of Ions at Aqueous Interfaces

By
Shane W. Devlin

A dissertation submitted in partial satisfaction of the
requirements for the degree of
Doctor of Philosophy
in
Chemistry
in the
Graduate Division
of the
University of California, Berkeley

Committee in charge:
Professor Richard J. Saykally, chair
Professor David T. Limmer
Professor Roya Maboudian

Spring 2023

Abstract
Nonlinear Optical Spectroscopy of Ions at Aqueous Interfaces
By
Shane W. Devlin
Doctor of Philosophy in Chemistry
University of California, Berkeley
Professor Richard J. Saykally, chair

That selected ions have an energetic preference to reside at the air-water interface, rather than in the bulk, is a relatively new development in our understanding of aqueous interfaces. While significant experimental and theoretical advances have been made in this field in recent years, the underlying physics, which existing models of ion solvation and ion partitioning are based upon, is still not completely understood. The benefits of a rich understanding of interfacial phenomena are many-fold, including enhancing our knowledge of atmospheric aerosol chemistry, accelerated reactions in "on-water" catalysis, and many biological interactions. The contents of this thesis describe efforts to deepen the detailed understanding of ion adsorption to air-water and water-hydrophobe interfaces through the use of nonlinear spectroscopy tools, which exclusively probe ions and water molecules at liquid interfaces.

Chapter 1 gives a historical overview of the field of ions at liquid interfaces, beginning with original models of ion adsorption developed by Wagner, Onsager, and Samaras, based on the physics of image charge repulsion. In this model, *all* ions were predicted to be expelled from the liquid-vapor boundary. This model was eventually revisited following new measurements from the atmospheric chemistry community, which indicated that certain ions were active at the air-water interface. At the end of this chapter, a new description of ion adsorption, focusing on the mechanism of what drives ions to the air-water interface, is presented.

Chapter 2 describes the nonlinear spectroscopy tools that are used in this thesis: Deep UV Second Harmonic Generation (DUV-SHG) and broadband Deep UV Electronic Sum-Frequency Generation (DUV-ESFG) spectroscopy. This section begins by outlining the theoretical framework for nonlinear spectroscopy, starting from the bulk polarization term that describes the response of a material under an applied electric field, expanding that to second-order, and elucidating the necessary

requirements for generating SH and SF photons. The experimental designs for these techniques as well as data collection and analysis are discussed in detail. The end of this chapter discusses the Langmuir model of adsorption, used to extract thermodynamic information, such as the Gibbs free energy of adsorption, from spectroscopic SH data. A derivation of this formalism is given and, importantly, the limitations of this model are discussed regarding the systems being studied.

Chapter 3 applies the above-mentioned surface sensitive spectroscopies to study a system of central environmental and atmospheric interest, the aqueous carbonate system. In particular, DUV-SHG is used to investigate the surface partitioning of the carbonate and bicarbonate anions to the air-water interface. It is determined from the SH data and application of the Langmuir model that the doubly charged carbonate anion is more strongly attracted to the air-water interface than is the singly charged bicarbonate, an observation that diametrically disagrees with current models of ion adsorption. The latter half of this chapter includes molecular dynamics simulation results which give insight to this unintuitive phenomenon.

Chapter 4 describes experiments and theory to study the adsorption of a prototypical inorganic anion, SCN^-, to two water-hydrophobe interfaces, water-toluene and water-decane. DUV-SHG determined that the Gibbs free energy of adsorption to these interfaces were equal within error, and were also equal to both the air-water and water-graphene interfaces. Charge-Transfer-To-Solvent (CTTS) spectra of the anion at these interfaces were measured by DUV-ESFG and revealed that the solvation environment around the anion at these disparate interfaces was essentially the same. However, MD simulations revealed a strikingly different mechanism of adsorption to the water-toluene and water-decane interfaces than was deduced for air-water and water-graphene.

Chapter 5 describes new methods to study ion adsorption to buried liquid-liquid interfaces. A planar liquid sheet jet, developed at the SLAC National Accelerator Laboratory, is used for the generation of thin planar liquid sheets for study with DUV-SHG spectroscopy measurements. The experimental methodology and mathematical framework for interpreting spectroscopic SH measurements from these liquid sheets is given in detail. This new technology is then used to study the adsorption of SCN^- to the water-heptane interface. Temperature dependent measurements of the Gibbs free energy are presented, which permits experimental

determination of the enthalpic and entropic components of the overall Gibbs free energy for these prototype oil-water interfaces.

Chapter 6 applies DUV-ESFG to the study of a biologically relevant chromophore, phenol, at the air-water interface. The $\left|\chi^{(2)}\right|^2$ interfacial spectrum of phenol indicates a red-shift of the lower-energy transition, as a result of a unique solvation environment prevailing at the surface, in comparison to the bulk spectrum. Accompanying calculations and two-photon absorption spectra are presented which give insight into this unique solvation behavior.

Acknowledgements

There are many people I owe an enormous thank you to for their support, friendship, and love over the last 5 years - far more than those mentioned by name in this section.

First, I want to thank my advisor, Rich Saykally, who has helped to shape my general approach to science, how I think critically about problems, and most importantly how to have fun while doing it all. Completing a PhD can be a tiring and overwhelming journey, but Rich was always full of wild experimental ideas to keep things interesting. I knew from the first time I met Rich that working for him would be a lot of fun, and I could not have made a better choice for my PhD advisor. I will miss taking breaks from work to throw the baseball around and sipping on cappuccinos from Coffee Lab (thanks for always paying for those..) while we chatted about science.

To all of the members of the Saykally group who made showing up to work every day not only a lot of fun, but also intellectually stimulating: I am indebted to you. Hikaru Mizuno was a great friend and mentor when I first joined the group and I owe much of my success to his guidance early on. Frank Bernal has been one of my best friends since we started graduate school together, and it has been an absolute pleasure to have a friend to puzzle over data with, and also to drink Berkeley's finest beers with, on a regular basis. Erika Riffe was an extremely welcome addition to the group following Frank and I, and I am glad that we could bond over the greatness that is Tom Brady, through our respective football teams.

Going back to my time as an undergraduate student at Boston University, Dr. Richard Andino was a tremendous mentor to me as I first started getting involved with research. I could not have had a more patient, thoughtful, and intelligent mentor for those three years working with Richard. If not for him, I would not have chosen to pursue graduate school. I am lucky to still consider him a close friend to this day.

Of course, all of my collaborators over the years are owed an enormous thank you, for none of this work could have been completed without them. Towards the end of my PhD, I had a very fruitful collaboration with Jake Koralek and DJ Hoffman from SLAC, and I learned an incredible amount from the two of them. Craig Schwartz has always been an inspiring scientist to me, and my conversations &

collaborations with him over the years always left me feeling refreshed and excited about tackling new and challenging problems. Ilan Benjamin and Tod Pascal's research groups contributed molecular dynamics simulations to some of my published work, and I thank them for helping make sense out of messy nonlinear spectroscopy data.

Life outside of the lab in Berkeley hasn't been so bad either. Alex Prophet has been a great friend over the years and I am thankful for many nights at Tap Haus shooting pool, for late-night bike rides down to McNally's Irish pub, and for afternoons betting on the horse races at Golden Gate Fields. Mira Liu has been an inspiring source of creativity over the years through her devotion to crafts of all sorts, and helped to consistently put the "warm" in Warm Wednesdays.

Although I have lived far from the east coast, I am thankful for the many friends from home who made an effort to keep in touch. Kevin, Tyler, and Anthony have been great friends since high school, and their visits to the west coast have been some of my favorite memories.

My family has also been a tremendous source of support throughout all of this. From their many visits to the west coast and constant encouragement, I was able to keep in perspective that the stressful minutia of graduate school are not as important as they seem in the moment. In particular, my grandfathers, John Mackin and John Devlin, introduced me to science at a young age, and I am thankful they helped set me on the path that has led to where I am now. My older brother, Pat Devlin, always opened the doors to his home in Reno Nevada for me when I needed a few days away from the lab.

Most importantly, my parents, Patrick and Cindy Devlin, have always served as a source of inspiration to me for their tireless work ethic. My father has worked nonstop over the years to support 5 children through college and allowed them to study the subject of their choosing. My mother, while raising 5 children, went back to college and completed her nursing degree. Her late nights of studying at the kitchen table were formative in my appreciation for learning and education. While my college and graduate school studies have been somewhat of a mystery to them, they are largely responsible for any success I have happened to stumble upon.

And lastly, Scout, to whom I owe a great debt of gratitude. Thank you for moving across the country with me to start this scary and exciting new journey. The experiences we have shared together in Berkeley, and all over California, have been

wonderful, and I would not trade them for anything. Through the many stresses of graduate school, you have been a constant source of joy and comfort, and I am grateful to have had you by my side through it all.

Table of Contents

Chapter 1: Introduction

Water is present in all three of its phases of matter across a very narrow range of temperature and pressure, making liquid water, ice, and water vapor essential to life under ambient conditions. Unsurprisingly, scientists for centuries have been studying water and the unique properties of the water phase diagram to gain a better understanding of the natural world around us.

Equally important as the understanding of "bulk" water and its ubiquity as a universal solvent are the many interfaces it can form in the presence of other media. The most prevalent of these in the natural environment is the air-water interface, which governs the chemistry occurring at the ocean surface as well as in atmospheric aerosols, for example. Over the last two decades, there has been significant revived interest in the study of the air-water interface and, in particular, for developing a thermodynamic description for the behavior of simple, inorganic salt solutions at this phase boundary. A current understanding of the field should first begin from a historical perspective.

1.1 Ions at Interfaces: A Historical Depiction

The study of ions at interfaces has for a long time been of interest to physical chemists. As early as 1910, Heydweiler and his students reported a comprehensive study of monovalent salts that increased the surface tension of pure water as a function of salt concentration, via the capillary rise method.[1] Others, such as Jones and Ray, verified and expanded these experimental data sets in the following decades.[2] What was then needed was a model to interpret the experimental results.

Luckily, a quantitative description of ion adsorption phenomena can be understood from basic thermodynamics. First, the interface must be defined; one common method being to use the Gibb's Dividing Surface (GDS). The GDS is an infinitely sharp boundary of zero thickness between two media, and is located such that the solvent has net zero excess. Expressed another way, the GDS is a plane perpendicular to the surface normal, located where the average density of the liquid falls to ½ of its bulk value. In using this description, one can easily express the surface excess of a component i in a biphasic system at constant temperature and pressure:

$$\Gamma_i = -\frac{1}{RT}\left(\frac{\partial \gamma}{\partial c_i}\right)_{T,p} \quad (1.1)$$

Here, Γ_i is the surface excess of component i in the system, γ is the measured surface tension, and c_i is the concentration of component i. Equation 1.1 emphasizes that an increase in the surface tension results in a negative surface excess (depletion) and a decrease in surface tension results in positive surface excess (adsorption). The experimental surface tension data available at the time were therefore interpreted to conclude that all ions are repelled from the air-water interface, as they uniformly increased the surface tension of pure water.

A mathematical description to interpret these observations was first put forth by Wagner[3], and then improved upon by Onsager and Samaras[4], through their description of electrostatic image charge forces. Given an interface between two media, medium 1 and medium 2, with the respective dielectric constants ε_1 and ε_2, the following expression was derived to calculate the force that an ion approaching the interface experiences:

$$q_{image} = \frac{(\varepsilon_1 - \varepsilon_2)}{(\varepsilon_1 + \varepsilon_2)} q_{ion} \quad (1.2)$$

Here, q_{ion} is the charge of the ion and q_{image} is the image charge force that is exerted when the ion is in the interface region. When the ion is placed in the medium with the higher dielectric (such as is the case of a dissolved electrolyte approaching the air-water interface) the image charge force has the same sign as the charge on the ion, and the ion experiences image charge *repulsion.* When the ion is placed in the medium with a lower dielectric (such as an ion in water approaching a water-metal interface), the image charge force has the opposite sign and the ion experiences image charge *attraction*. This model was used to explain the observation of increased surface tension for inorganic salts in water, and was a well-accepted theorem: ions are repelled from the air-water interface.

Despite the acceptance of this model to interpret the available surface tension data, there were still inconsistencies that needed to be reconciled. For instance, the Langmuir isotherms were strongly dependent on the identity of the anion (i.e. all of the sodium halide salts exhibited different slopes). However, according to the model presented by Wagner, Onsager, and Samaras, all of these monovalent salts should have experienced the same repulsion from the interface. Nonetheless, this simple description of ion adsorption persisted for decades.

1.2 Contradiction With Atmospheric Chemistry Measurements

It was not until the mid 1980's that the model proposed by Wagner, Onsager, and Samaras began to be revisited, in light of repeated field measurements from the atmospheric chemistry community. Consistently, measurements of ozone depletion in the arctic were correlated with increases in bromine-containing compounds in the atmosphere. For example, Barrie et al. reported large drops in ground-level atmospheric ozone concentrations from ~40 ppb to ~0 ppb after the polar sunrise and linked these ozone depletion events to catalytic reactions with BrO_x compounds from the arctic ocean.[5] Similarly, Impey et al reported high levels of photolyzable bromine in the form of BrO and HOBr coinciding with ozone drops. They also detected high levels of Br_2 present at the end of ozone depletion events and hypothesized that these increased concentrations were coming from processes occurring at the snowpack surface.[6] Despite the observation that drops in ozone were correlated with increases in atmospheric bromine, there was not a well-accepted mechanism for what was driving this behavior. To further confuse the picture, it was not understood why the same processes were not occurring with chlorine compounds, given that chlorine is present in much higher concentrations in the ocean and snowpack.

To address these questions, Hunt et al used aerosol chamber experiments and kinetic modeling to study the reaction of gaseous ozone with aqueous sodium bromide particles.[7] They reported that the reaction of ozone with aqueous bromide generates significant amounts of Br_2, at rates much faster than those predicted using bulk kinetic constants. They proposed a kinetic model wherein the reaction must be occurring between gaseous ozone and bromide anions residing at the surface of the aqueous sodium bromide particles. These newly-included surface reactions gave much better agreement between their modeling and experimental data. Their work was further supported by molecular dynamics simulations that highlighted the surface affinity of bromide, as well as long residence times of ozone at the interface, which allowed for the reactions to occur.

1.3 Molecular Simulations of Ion Adsorption

The measurements coming from the atmospheric chemistry community caused many people to question the validity of the Wagner, Onsager, and Samaras model of interfacial ion adsorption. The evidence suggested that ozone depletion events were

due to reactions occurring at the surface of aqueous aerosols above the arctic ocean and snowpack, even though the models predicted that the interface should be devoid of bromide ions. In light of this, theoretical chemists began to use molecular simulations to revisit this subject to see if they could refine the understanding of ion adsorption.

An early study conducted in 2000 by Knipping et al combined experiment and theory to study the reaction of deliquesced sodium chloride aerosols in the presence of ozone.[8] They used differential optical absorption spectroscopy and mass spectrometry to follow the kinetics of the gas phase species, and observed chlorine gas production only after the system was irradiated with UV light, which produced OH radicals from ozone, and then reacted with chloride anions. The initial production rate of chlorine gas scaled with the surface area of the aerosol particles, a key indication that a surface mediated process was active. To support these measurements, molecular dynamics simulations of sodium chloride particles of variable size were conducted, although the main findings reported were those from a slab geometry. The authors found that sodium cations were strongly repelled from the interface, but that the chloride anions occupied a significant portion of the slab surface, and attributed these different surface affinities mainly to ion size: viz. the small sodium cation fit nicely into the hydrogen bond network of water, whereas the large chloride did not, and thus it was expelled to the surface. It is important to note that the authors investigated two potential models in this study, and found that the model which included explicit polarizabilities for water and the ions produced results that more strongly agreed with the experimental data.

Shortly after this work, Jungwirth and Tobias published a landmark paper, wherein they used MD simulations with a polarizable model to investigate the surface behavior of aqueous sodium halide solutions (NaF, NaCl, NaBr, NaI).[9] Specifically, they calculated the relative density profiles of 1.2 M electrolyte solutions as a function of distance from the surface, and showed systematically that surface affinity was positively correlated with ion size and polarizability; i.e. small fluoride anions were strongly repelled from the interface, but larger halides showed some degree of surface adsorption. Bromide and iodide even showed enhanced concentrations in the outermost layer of the air-water interface, relative to their bulk concentration. The sodium counter cation was repelled from the interface for all solutions, however the larger halides (Br^- and I^-) dragged significantly more sodium towards the surface than

did Cl^- and F^-. The authors attributed the surface affinity of bromide and iodide to anisotropic solvation at the interface, which generated significant dipole moments on the ions. These strong dipole-dipole bonding arrangements conferred energetic benefits over the weaker ion-dipole interactions in the bulk.

In all cases, beyond the enhanced surface population of the anion, there was found to be a subsurface depletion of ions. When the surface excess was integrated through this entire interfacial region, the surface population was depleted relative to the bulk. In this way, the interpretation from thermodynamics over the previous 70 years still held. Through the *entire* interfacial region, there is a net depletion of ions. This study was a key to meshing the microscopic structure of the interface learned from simulation with the macroscopic surface tensions measurement. From this evolved understanding, new solute-partitioning models were constructed from the Gibbs-Duhem equation, and were used to calculate the surface concentration of atmospherically relevant ions.[10] Additionally, simulations predicted certain properties of the interface that could be tested with a new class of experiment.

1.4 Surface-Sensitive Spectroscopy of Ions at Interfaces

A detailed section on the theory and practice of surface sensitive, nonlinear spectroscopy will be given in Chapter 2. This section will present a historical narrative of surface sensitive spectroscopy and how it has led to our current understanding of ion adsorption chemistry.

While the new simulations referenced above gave unprecedented detail about the interface, what was also needed was experimental confirmation of enhanced ion populations. Additionally, simple, yet important questions such as "how does the hydrogen bonding structure of the interface change upon addition of electrolytes?" were unable to be answered with the current arsenal of experiments. Classical methods such as surface tension measurements lacked the molecular specificity that was required to answer such questions, as they probed much deeper into the interface than where the ion enhancement was proposed to be occurring. Similarly, while kinetic experiments of aerosols particles were able to discern that surface processes were occurring, they still had significant contributions from the bulk phase, as well as other confounding variables that were difficult to disentangle.

The solution to answering these questions was an entirely new class of experiment, which had recently come into practice through the development of

ultrafast laser systems. Second-order nonlinear spectroscopies are inherently surface sensitive under the electric dipole approximation, meaning a signal is only generated from a non-centrosymmetric environment.[11] Since interfaces naturally break inversion symmetry, these spectroscopies offer a way to clearly distinguish inherently weak surface signals from much larger bulk responses. Two of these techniques that are commonly employed to study interfaces are second harmonic generation (SHG) and vibrational sum-frequency generation (vSFG) spectroscopy. SHG is typically used as a photon-counting technique, however vSFG uses an IR pulse that is tuned into resonance with molecular vibrations, and can therefore measure vibrational *spectra* of the interface. Both of these techniques report on the outermost water layers, circa 1 nm.[11,12]

The first SHG measurement of the neat air-water interface was conducted by the Eisenthal group in 1988, wherein they probed the absolute SHG phase of water to determine the net dipole orientation at the surface.[13] Five years later in 1993, the first vibrational spectrum of the air-water interface was published by Shen and coworkers, which offered unprecedented detail about the molecular structure at the surface.[14] Specifically, they confirmed that on average, 20% of all water molecules at the interface orient with an OH bond projecting into the vapor phase.

Shortly after, vSFG began to focus on the perturbation that dissolved electrolytes induce at the air-water interface. Schultz et al. studied large, polyatomic anions such as NO_3^- and SO_4^{2-} and their respective acids. They found that these solutions minimally disrupted the hydrogen bonding network in the interface, and did not perturb the outermost surface monolayer of dangling OH bonds.[15,16] In 2004, Raymond and Richmond investigated the effects of NaF, NaCl, NaBr, and NaI on the interfacial water structure. While they reported larger spectral changes corresponding to anion size in the low energy region of the spectrum, they also reported negligible changes to the uncoupled, dangling OH mode. Their interpretation was therefore that even larger and more polarizable anions, such as Br^- and I^-, did not reside in the top-most water layer, in contrast with the prediction from Jungwirth and Tobias' MD simulations.[17] Others investigated the behavior of strong acid/base solutions, highlighting the stronger surface affinity of hydronium for the interface relative to hydroxide.[18,19] The debate over surface pH and molecular structure under acidic and basic conditions is still one that is intensely ongoing. Additionally, significant

progress was made in understanding the detailed molecular structure at the neat interface as well as in the presence of electrolytes.[12,20,21]

VSFG was crucial to developing a deep understanding of the air-water interface. However, an important consideration to these experiments is that vSFG reports on the interfacial water structure, and therefore information on the ion population at the surface is *indirectly inferred.*

For an alternative perspective, Petersen and Saykally developed deep ultraviolet SHG (DUV-SHG), a technique that exploits anion resonances in the deep UV to *directly probe* the interfacial ion population. Using DUV-SHG, they reported the first direct confirmation of enhanced ion concentration at the air-water interface for a highly polarizable anion (N_3^-).[22] By measuring the second harmonic intensity as a function of anion concentration, and fitting the experimental data to a modified Langmuir adsorption model, they determined the Gibbs free energy of adsorption for azide to be ~ –10 kJ/mol. Using this same technique, they measured the adsorption free energy for several anions, which are given in Table 1.

Table 1.1: Surface Affinity of Anions To the Air-water Interface as Measured by DUV-SHG

Anion	Gibbs Free Energy of Adsorption (kJ/mol)
N_3^-	-9.9 ± 0.3 [22]
I^-	-3.4 [23]
Br^-	-1.4 [24]
SCN^-	-7.5 ± 0.1 [25]
NO_2^-	-17.8 [26]

To further develop the understanding of ion adsorption, electronic interfacial *spectra*, which could report information on the solvation environment of the ions at the interface, were needed. For this, Rizzuto and Saykally developed broadband deep ultraviolet electronic sum frequency generation spectroscopy (DUV-ESFG), a technique adapted from Yamaguchi and Tahara[27]. This spectroscopy combines a broadband white light continuum pulse and a narrowband UV pulse to measure spectra in the deep UV with a single laser pulse. By tuning the UV photon to be resonant with the charge transfer to solvent transition of many common anions, one

can probe the interfacial solvation environment of the ion. This was first applied to study the iodide anion at the air-water interface, and it was reported that there was a significant redshift and linewidth narrowing of the J = 3/2 transition, as well as a drastic intensity loss and redshift in the J = 1/2 transition, when compared to the bulk spectrum.[28] The authors speculated this linewidth narrowing to be a result of an increased lifetime of the J = 3/2 state at the interface, due to a change in the solvation environment. This understanding was later refined, when 2PA spectroscopy and calculations showed the intensity difference to be a consequence of selection rules for ESFG spectroscopy.[29] This technique was also used to refine our understanding of the sodium nitrite system at the air-water interface. Previous SHG measurements had reported the formation of contact ion pairs at the interface, as well as a redshift in the interfacial absorption spectrum. DUV-ESFG instead showed no change in the interfacial spectrum, and accompanying calculations showed minimal ion pairing. [30]

Given these different experimental techniques, a multifaceted approach to studying the air-water interface was in full force; vSFG reported on the interfacial water structure, and led to advancements in our understanding of the hydrogen bonding network at the interface. DUV-SHG and DUV-ESFG probed ions directly, reporting thermodynamic information as well as information on the solvation environment.

1.5 Developing a Mechanism of Ion Adsorption

An open question that remained was in describing the molecular origins for the experimentally confirmed ion adsorption. Since the early work of Jungwirth and Tobias, many had been working on developing a mechanism for what drives ions towards or away from hydrophobic boundaries.

Baer and Mundy studied the adsorption of the iodide anion to the air-water interface, and reported that the first solvation shell and polarization response of the anion were crucial ingredients for ion adsorption, and that quantum chemical treatment of the interaction potentials might be necessary for a deeper understanding.[31] Similar conclusions were drawn by Levin and colleagues, who reproduced surface tension data and surface affinities from a dielectric continuum theory approach that focused on the ion size and polarization response.[32,33] Geissler and Vanhoucke identified a balance of strong opposing forces for ion adsorption, via volume exclusion and the polarization response in dense polar liquids (water and a

stockmayer liquid), which were nearly equal in magnitude. Additionally, while their simulations used a GDS, they highlighted that the force exerted by an ion near the liquid phase boundary is more than sufficient to distort the shape of the interface, engendering changes in local solvent density near the ion.[34] They cautioned that properly capturing the solvent response and understanding the driving forces for ion adsorption would require a method to model interfacial fluctuations. Shortly after this, the instantaneous liquid interface concept was introduced by Willard and Chandler.[35]

As described in the previous section, DUV-SHG was proven to be a highly useful tool for extracting thermodynamic information on ion adsorption. However, like the surface tension measurements described earlier, it provided a macroscopic thermodynamic perspective, which on its own lacked molecular specificity. To overcome this, Saykally and Geissler combined DUV-SHG with state of the art simulations, and revisited the adsorption of the thiocyanate anion to report the molecular-level details that were unavailable from experiment alone. Specifically, they deconvoluted the enthalpic and entropic contributions to the overall Gibbs free energy and determined the mechanistic driving force for the adsorption of weakly-solvated anions to the air-water interface: 1) solvent repartitioning, viz. the shedding of one or two solvating waters, which can form stronger hydrogen bonds as part of the bulk water network, provides an enthalpic benefit. 2) the presence of the ion at the interface dampens capillary wave fluctuations, which entropically impedes adsorption. The loss in entropy is much smaller than the enthalpic gain from solvent repartitioning, making this an energetically favorable process. This work was crucial in highlighting the specific role that ion hydration enthalpy plays in the adsorption process, i.e. that weakly-solvated ions tend to be the most surface active, and strongly-solvated ions tend to be repelled from the interface, roughly following the Hofmeister scale. More so, this was a large step forward in enhancing our understanding of adsorption beyond atomic factors, such as size and polarizability.

It is important to note that the mechanism of specific ion adsorption is still debated in the literature[36,37], and our understanding of what drives ions towards or away from interfaces will continue to evolve with new experimental and theoretical studies.

1.6 Conclusions

From the early days of Heydweiler and Jones and Ray, our understanding of ion adsorption has drastically evolved. For example, it is now well-accepted that certain ions have a strong preference to reside at the air-water interface versus the bulk solution. Over the course of the last 20 years, authors have rationalized the surface affinity of selected ions through various properties of the ion and the solvent. What is presently clear, however, is that large, polarizable, and weakly-solvated ions tend to be the most surface active. Disentangling *exactly* what drives ions towards the interface of a dense, polar liquid is a complex challenge and more theoretical and experimental work is still required to develop a generalized mechanism of ion adsorption. Having such a complete description of ion adsorption and ion solvation will benefit many fields of chemistry and physics, including atmospheric aerosol chemistry, geochemistry, catalysis, and biology.

Additionally, there are many advances that remain to be made in the field. The nature and effects of ion pairing in a reduced dielectric environment, such as an interface, and the consequences for ion adsorption, is still an open question with important consequences for many systems. The study of liquid-liquid interfaces that form between water and non-polar liquids is also highly relevant to many systems in biology and the environment. Both of these questions are studied in the later chapters of this thesis.

References

(1) Heydweiler, A. Interdependence of the Physical Properties of Solutions. II. Surface Tension and Electrical Conductivity of Aqueous Salt-Solutions. Ann. d. Phys. 1910, 4 (33), 145–185. *Ann. d. Phys* **1910**, *4* (33), 145–185.

(2) Jones, G.; Ray, W. A. The Surface Tension of Solutions of Electrolytes as a Function of the Concentration. I. A Differential Method for Measuring Relative Surface Tension. *J. Am. Chem. Soc.* **1937**, *59* (1), 187–198. https://doi.org/10.1021/ja01280a048.

(3) Wagner, Carl. *Phys. Zeitschrift* **1924**, *25*, 474.

(4) Onsager, L.; Samaras, N. N. T. The Surface Tension of Debye-Hückel Electrolytes. *J. Chem. Phys.* **1934**, *2* (8), 528–536. https://doi.org/10.1063/1.1749522.

(5) Barrie, L. A.; Bottenheim, J. W.; Schnell, R. C.; Crutzen, P. J.; Rasmussen, R. A. Ozone Destruction and Photochemical Reactions at Polar Sunrise in the Lower

Arctic Atmosphere. *Nature* **1988**, *334* (6178), 138–141. https://doi.org/10.1038/334138a0.

(6) G. A. Impey; Mihele, C.M.; Anlauf, K.G.; Barrie, L.A.; Hastie, D.R.; Shepson, P. B. Measurements of Photolyzable Halogen Compounds And Bromine Radicals During the Polar Sunrise Experiment 1977. *J. Atmo. Chem.* **1999**, No. 34, 21–37.

(7) Hunt, S. W.; Roeselová, M.; Wang, W.; Wingen, L. M.; Knipping, E. M.; Tobias, D. J.; Dabdub, D.; Finlayson-Pitts, B. J. Formation of Molecular Bromine from the Reaction of Ozone with Deliquesced NaBr Aerosol: Evidence for Interface Chemistry. *J. Phys. Chem. A* **2004**, *108* (52), 11559–11572. https://doi.org/10.1021/jp0467346.

(8) Knipping, E. M.; Lakin, M. J.; Foster, K. L.; Jungwirth, P.; Tobias, D. J.; Gerber, R. B.; Dabdub, D.; Finlayson-Pitts, B. J. Experiments and Simulations of Ion-Enhanced Interfacial Chemistry on Aqueous NaCl Aerosols. *Science* **2000**, *288* (5464), 301–306. https://doi.org/10.1126/science.288.5464.301.

(9) Jungwirth, P.; Tobias, D. J. Molecular Structure of Salt Solutions: A New View of the Interface with Implications for Heterogeneous Atmospheric Chemistry. *J. Phys. Chem. B* **2001**, *105* (43), 10468–10472. https://doi.org/10.1021/jp012750g.

(10) Pegram, L. M.; Record, M. T. Partitioning of Atmospherically Relevant Ions between Bulk Water and the Water/Vapor Interface. *Proc. Natl. Acad. Sci.* **2006**, *103* (39), 14278–14281. https://doi.org/10.1073/pnas.0606256103.

(11) Robert W. Boyd. *Nonlinear Optics*; Academic Press, 2020.

(12) Raymond, E. A.; Tarbuck, T. L.; Brown, M. G.; Richmond, G. L. Hydrogen-Bonding Interactions at the Vapor/Water Interface Investigated by Vibrational Sum-Frequency Spectroscopy of HOD/H_2O/D_2O Mixtures and Molecular Dynamics Simulations. *J. Phys. Chem. B* **2003**, *107* (2), 546–556. https://doi.org/10.1021/jp021366w.

(13) Goh, M. C.; Hicks, J. M.; Kemnitz, K.; Pinto, G. R.; Heinz, T. F.; Eisenthal, K. B.; Bhattacharyya, K. Absolute Orientation of Water Molecules at the Neat Water Surface. *J. Phys. Chem.* **1988**, *92* (18), 5074–5075. https://doi.org/10.1021/j100329a003.

(14) Du, Q.; Superfine, R.; Freysz, E.; Shen, Y. R. Vibrational Spectroscopy of Water at the Vapor/Water Interface. *Phys. Rev. Lett.* **1993**, *70* (15), 2313–2316. https://doi.org/10.1103/PhysRevLett.70.2313.

(15) Shultz, M. J.; Schnitzer, C.; Simonelli, D.; Baldelli, S. Sum Frequency Generation Spectroscopy of the Aqueous Interface: Ionic and Soluble Molecular Solutions. *Int. Rev. Phys. Chem.* **2000**, *19* (1), 123–153. https://doi.org/10.1080/014423500229882.

(16) Schultz, M. J.; Baldelli, S.; Schnitzer, C.; Simonelli, D. Aqueous Solution/Air Interfaces Probed with Sum Frequency Generation Spectroscopy. *J. Phys. Chem. B* **2002**, *106* (21), 5313–5324. https://doi.org/10.1021/jp014466v.

(17) Raymond, E. A.; Richmond, G. L. Probing the Molecular Structure and Bonding of the Surface of Aqueous Salt Solutions. *J. Phys. Chem. B* **2004**, *108* (16), 5051–5059. https://doi.org/10.1021/jp037725k.

(18) Tarbuck, T. L.; Ota, S. T.; Richmond, G. L. Spectroscopic Studies of Solvated Hydrogen and Hydroxide Ions at Aqueous Surfaces. *J. Am. Chem. Soc.* **2006**, *128* (45), 14519–14527. https://doi.org/10.1021/ja063184b.

(19) Mucha, M.; Frigato, T.; Levering, L. M.; Allen, H. C.; Tobias, D. J.; Dang, L. X.; Jungwirth, P. Unified Molecular Picture of the Surfaces of Aqueous Acid, Base, and Salt Solutions. *J. Phys. Chem. B* **2005**, *109* (16), 7617–7623. https://doi.org/10.1021/jp0445730.

(20) Tarbuck, T. L.; Richmond, G. L. Adsorption and Reaction of CO_2 and SO_2 at a Water Surface. *J. Am. Chem. Soc.* **2006**, *128* (10), 3256–3267. https://doi.org/10.1021/ja057375a.

(21) Walker, D. S.; Hore, D. K.; Richmond, G. L. Understanding the Population, Coordination, and Orientation of Water Species Contributing to the Nonlinear Optical Spectroscopy of the Vapor–Water Interface through Molecular Dynamics Simulations. *J. Phys. Chem. B* **2006**, *110* (41), 20451–20459. https://doi.org/10.1021/jp063063y.

(22) Petersen, P. B.; Saykally, R. J. Confirmation of Enhanced Anion Concentration at the Liquid Water Surface. *Chem. Phys. Lett.* **2004**, *397* (1–3), 51–55. https://doi.org/10.1016/j.cplett.2004.08.049.

(23) Petersen, P. B.; Saykally, R. J. Probing the Interfacial Structure of Aqueous Electrolytes with Femtosecond Second Harmonic Generation Spectroscopy. *J. Phys. Chem. B* **2006**, *110* (29), 14060–14073. https://doi.org/10.1021/jp0601825.

(24) Onorato, R. M.; Otten, D. E.; Saykally, R. J. Measurement of Bromide Ion Affinities for the Air/Water and Dodecanol/Water Interfaces at Molar

Concentrations by UV Second Harmonic Generation Spectroscopy. *J. Phys. Chem. C* **2010**, *114* (32), 13746–13751. https://doi.org/10.1021/jp103454r.

(25) Petersen, P. B.; Saykally, R. J.; Mucha, M.; Jungwirth, P. Enhanced Concentration of Polarizable Anions at the Liquid Water Surface: SHG Spectroscopy and MD Simulations of Sodium Thiocyanide. *J. Phys. Chem. B* **2005**, *109* (21), 10915–10921. https://doi.org/10.1021/jp050864c.

(26) Otten, D. E.; Onorato, R.; Michaels, R.; Goodknight, J.; Saykally, R. J. Strong Surface Adsorption of Aqueous Sodium Nitrite as an Ion Pair. *Chem. Phys. Lett.* **2012**, *519–520*, 45–48. https://doi.org/10.1016/j.cplett.2011.10.056.

(27) Yamaguchi, S.; Tahara, T. Precise Electronic $\chi^{(2)}$ Spectra of Molecules Adsorbed at an Interface Measured by Multiplex Sum Frequency Generation. *J. Phys. Chem. B* **2004**, *108* (50), 19079–19082. https://doi.org/10.1021/jp045306x.

(28) Rizzuto, A. M.; Irgen-Gioro, S.; Eftekhari-Bafrooei, A.; Saykally, R. J. Broadband Deep UV Spectra of Interfacial Aqueous Iodide. *J. Phys. Chem. Lett.* **2016**, *7* (19), 3882–3885. https://doi.org/10.1021/acs.jpclett.6b01931.

(29) Bhattacharyya, D.; Mizuno, H.; Rizzuto, A. M.; Zhang, Y.; Saykally, R. J.; Bradforth, S. E. New Insights into the Charge-Transfer-to-Solvent Spectrum of Aqueous Iodide: Surface versus Bulk. *J. Phys. Chem. Lett.* **2020**, *11* (5), 1656–1661. https://doi.org/10.1021/acs.jpclett.9b03857.

(30) Mizuno, H.; Oosterbaan, K. J.; Menzl, G.; Smith, J.; Rizzuto, A. M.; Geissler, P. L.; Head-Gordon, M.; Saykally, R. J. Revisiting the $\pi \rightarrow \Pi^*$ Transition of the Nitrite Ion at the Air/Water Interface: A Combined Experimental and Theoretical Study. *Chem. Phys. Lett.* **2020**, *751*, 137516. https://doi.org/10.1016/j.cplett.2020.137516.

(31) Baer, M. D.; Mundy, C. J. Toward an Understanding of the Specific Ion Effect Using Density Functional Theory. *J. Phys. Chem. Lett.* **2011**, *2* (9), 1088–1093. https://doi.org/10.1021/jz200333b.

(32) Levin, Y. Polarizable Ions at Interfaces. *Phys. Rev. Lett.* **2009**, *102* (14), 147803. https://doi.org/10.1103/PhysRevLett.102.147803.

(33) Levin, Y.; dos Santos, A. P.; Diehl, A. Ions at the Air-Water Interface: An End to a Hundred-Year-Old Mystery? *Phys. Rev. Lett.* **2009**, *103* (25), 257802. https://doi.org/10.1103/PhysRevLett.103.257802.

(34) Noah-Vanhoucke, J.; Geissler, P. L. On the Fluctuations That Drive Small Ions toward, and Away from, Interfaces between Polar Liquids and Their Vapors. *Proc.*

Natl. Acad. Sci. **2009**, *106* (36), 15125–15130. https://doi.org/10.1073/pnas.0905168106.

(35) Willard, A. P.; Chandler, D. Instantaneous Liquid Interfaces. *J. Phys. Chem. B* **2010**, *114* (5), 1954–1958. https://doi.org/10.1021/jp909219k.

(36) Ben-Amotz, D. Interfacial Solvation Thermodynamics. *J. Phys. Condens. Matter* **2016**, *28* (41), 414013. https://doi.org/10.1088/0953-8984/28/41/414013.

(37) Wang, Y.; Sinha, S.; Desai, P. R.; Jing, H.; Das, S. Ion at Air–Water Interface Enhances Capillary Wave Fluctuations: Energetics of Ion Adsorption. *J. Am. Chem. Soc.* **2018**, *140* (40), 12853–12861. https://doi.org/10.1021/jacs.8b06205.

Chapter 2: Experimental Methods

This chapter describes the necessary background to understand the application of nonlinear spectroscopy to study aqueous interfaces. For brevity, only the necessary details are given and the reader is referred to the many papers that have been written on the subject for a more detailed description. [1–5]

In the second half of this chapter, the Langmuir model of adsorption, which is used heavily in this thesis, is discussed.

2.1 Second Order Nonlinear Spectroscopy

Second-order nonlinear spectroscopy has been a powerful tool for the study of interfaces, as it has enabled a way to discern the small signals arising from the few molecular layers that comprise an interface from the much larger bulk response. This capability has only come into practice in recent decades with the advent of ultrafast laser systems, which can achieve the required high field strengths for generating a measurable second order response from a material. To understand this, we can begin with the bulk polarization, P(t), of a material under an applied electric field:

$$P(t) \propto \chi^{(1)}E(t) + \chi^{(2)}E(t)E(t) + \chi^{(3)}E(t)E(t)E(t) + \cdots \qquad (2.1)$$

Here, χ^n is the nth-order susceptibility of the material and E(t) is the applied electric field. At low intensity electric field strength, the polarization is dominated by the linear response of the material, $\chi^{(1)}$. Since the polarization expression is a series expansion, each successive term diminishes in magnitude and only at high input field strengths does the second order susceptibility, $\chi^{(2)}$, which is inherently weak, become measurable.

Two commonly used second-order spectroscopies are second harmonic generation (SHG) and sum-frequency generation (SFG). In these techniques, two photons are overlapped in time and space to generate a single photon at the sum of the two input frequencies. As can be seen in Equation 2.1, the strength of the second-order response depends on the square of the input electric field. We can express the second harmonic field as the following:

$$E(t) = Ee^{i\omega t} + Ee^{-i\omega t} \qquad (2.2)$$

$$|E(t)|^2 = 2E^2 + E^2e^{i2\omega t} + E^2e^{-2i\omega t} \qquad (2.3)$$

Here ω represents the frequency of the field and E is the amplitude. Equation 2.3 highlights that multiple processes result from the creation of a new photon, including a frequency-independent DC field and a coherent second harmonic photon. The same result can be shown for sum-frequency generation by replacing one of the input electric fields with a different frequency, but is omitted here for brevity.

A cartoon depiction of how this is achieved at the air-water interface is shown in Fig 2.1, along with the respective energy level diagrams.

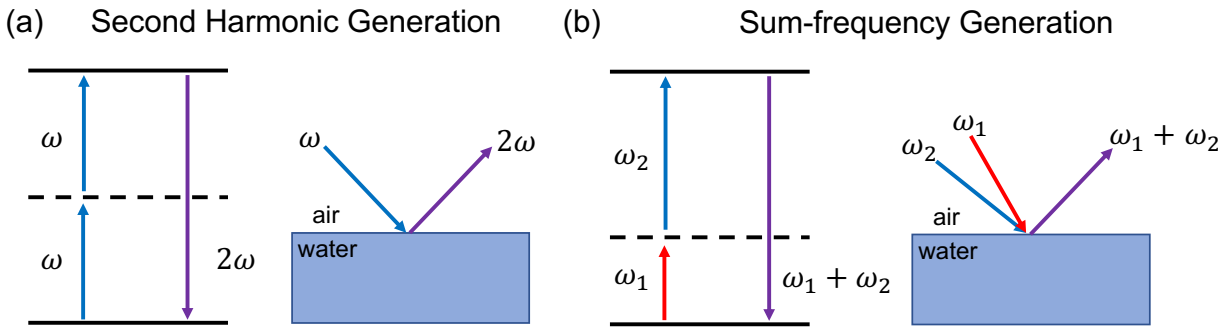

Figure 2.1: Energy level diagrams and cartoon depiction of experimental geometry for **(a)** second harmonic generation and **(b)** sum-frequency generation from the air-water interface

Under the electric dipole approximation, a $\chi^{(2)}$ signal can only be generated from a non-centrosymmetric environment, such as an interface.[3] This makes second-order spectroscopies highly surface selective. It can be easily demonstrated that $\chi^{(2)}$ vanishes in a medium with inversion symmetry by considering the second order polarization term:

$$P^{(2)}(t) = \chi^{(2)}_{i,j,k} * E(t)^2 \qquad (2.4)$$

In a centrosymmetric medium, we can invert the coordinates and rewrite Equation 2.4 as

$$-P^{(2)}(t) = \chi^{(2)}_{-i,-j,-k} * -E(t) * -E(t) \qquad (2.5)$$

By definition, under inversion symmetry, $\chi^{(2)}_{-i,-j,-k} = \chi^{(2)}_{i,j,k}$, therefore

$$-P^{(2)}(t) = \chi^{(2)}_{i,j,k} * E(t)^2 \quad (2.6)$$

Which leads to the following

$$-P^{(2)}(t) = P^{(2)}(t) \quad (2.7)$$

Equation 2.7 can only be true when $\chi^{(2)}_{i,j,k} = 0$, implying that the second-order response from a centrosymmetric environment (i.e. the bulk of a material) is necessarily zero. The same is true for all even-order spectroscopies.

$\chi^{(2)}_{i,j,k}$ is a third rank tensor, with 27 individual tensor elements. Changing the polarization of input light allows one to selectively probe various elements of $\chi^{(2)}_{i,j,k}$. In practice, due to the C_∞ symmetry of a planar interface, only four elements of $\chi^{(2)}_{i,j,k}$ are nonvanishing.[5]

2.2 Broadband Deep UV Electronic Sum Frequency Generation Spectroscopy

As discussed in the introduction chapter, the discovery that weakly-solvated ions were highly surface active reinvigorated the study of ions at interfaces.[6,7] In addition to measuring thermodynamic properties associated with ion adsorption, as was being done with DUV-SHG, interfacial *spectra* of ions were needed to help further refine the mechanism of ion adsorption.

For this purpose, Rizzuto et al developed Broadband Deep UV Electronic Sum Frequency Generation (DUV-ESFG) spectroscopy[8], extending the wavelength capabilities from a similar experimental design from Tahara et al.[9]t DUV-ESFG combines a narrowband UV photon with a white light continuum (WLC) to generate a broadband photon in the deep UV, capturing ~40 nm of spectral width. This technique allows interfacial electronic spectra to be collected over a considerable spectral range with a single laser pulse, enabling drastic improvements in signal to noise ratios and collection time when compared to measuring spectra with pointwise SHG measurements. Thereafter, quantitative measurements could be made of anion peak positions, intensities, and linewidths at the interface. When these interfacial spectra are compared to bulk absorption transitions and theoretical calculations, meaningful insight into the solvation environment of the ion at the interface can be

gained. The experimental design and layout for broadband DUV-ESFG is shown in Fig 2.2.

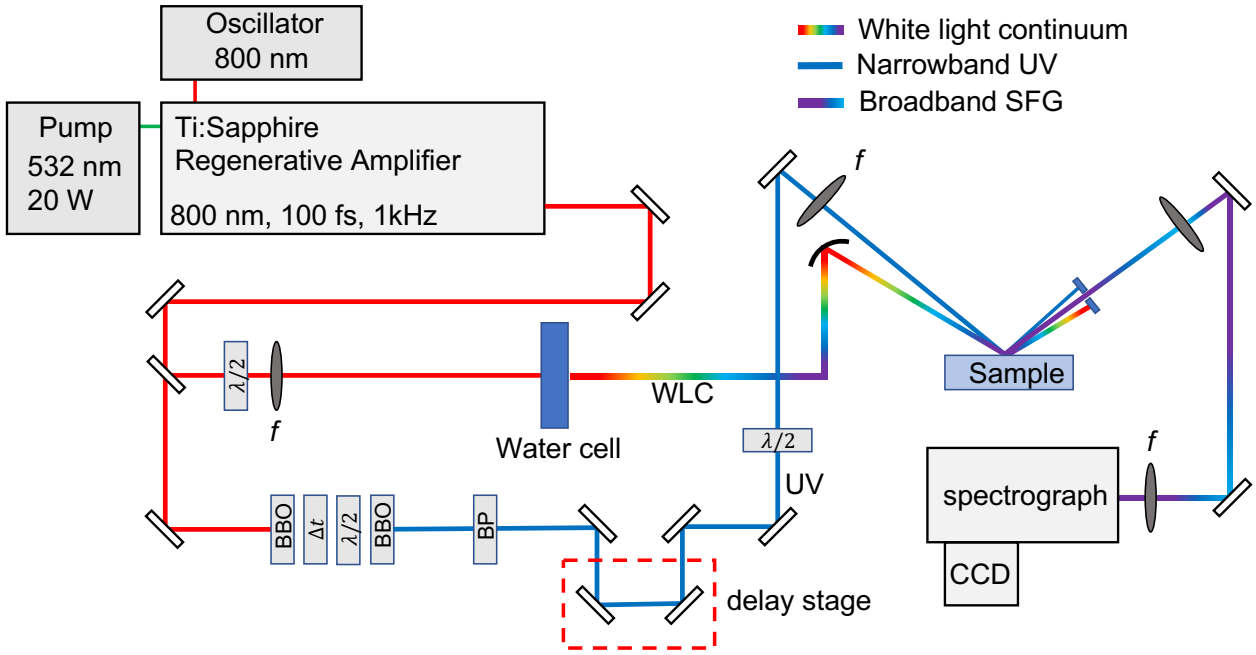

Figure 2.2: Experimental layout for broadband DUV-ESFG. BBO = β-barium borate, Δt = calcite delay plate, $\lambda/2$ = half-wave plate, BP = bandpass filter, f = focusing lens, CCD = charge coupled device.

The output of a commercial regenerative amplifier (Spectra Physics, 800 nm, 100 fs, 1kHz, 4 mJ/pulse) is split into two beam paths, to generate the two different input pulses. Beam path 1 is tightly focused into a continuously-flowing water cell to generate a broadband white light continuum (WLC) that spans ~600 – 1200 nm. This beam is directed towards the sample and is focused onto the air-water surface by a spherical mirror, to prevent chromatic aberrations of the broadband pulse. Beam path 2 is first passed through a β-barium borate (BBO) nonlinear crystal, which frequency doubles the 800 nm and generates 400 nm. A calcite delay plate (Δt) and half-wave plate ($\lambda/2$) then prepare the 800 nm and 400 nm beams to undergo sum-frequency generation in a second BBO crystal to generate the narrowband UV photon at 266 nm. A bandpass filter cleans the pulse and rejects any residual 800/400 nm light. The polarization of the UV photon is controlled with a half-wave plate prior to the sample and is then focused onto the water surface with a f=300 mm focusing lens. A delay

stage in the beam path of the UV photon allows one to control the timing of the pulse to ensure proper temporal overlap at the sample.

A 3-axis stage is used to house the sample, and helps achieve spatial overlap of the two input pulses. When temporal and spatial overlap is achieved, a coherent sum-frequency (SF) photon is generated in the phase-matched direction. The SF photon is spatially filtered from the two input pulses by a series of irises, and then collimated using a UV-fused silica lens. The SF photon is then focused by a CaF_2 lens and filtered with a UV bandpass filter before entering the spectrograph (SP-300i, Princeton Instruments) and being dispersed onto a thermoelectrically-cooled charge coupled device (CCD) (PIXIS 2KBUV, Princeton Instruments).

In the diagram as shown in Figure 2.2, the narrowband UV pulse is generated from a series of BBOs, resulting in a UV photon centered at 266nm. Our experimental set up also employs an optical parametric amplifier (OPA), extending the capability of this technique to access any wavelength in the UV-Vis from ~266-800 nm, which allows us to tune the UV input pulse or the SF photon to be resonant with a wide range of wavelengths.

To measure interfacial spectra of the anions, either one of the input pulses or the generated SF photon is required to be resonant with an electronic transition of the anion. Conveniently, many anions of interest possess a charge-transfer-to-solvent (CTTS) transition in the deep UV. CTTS transitions are broad, featureless bands in the UV and typically possess large extinction coefficients.[10] CTTS transitions are highly sensitive to the local chemical environment around the ion, which makes them an excellent reporter on interfacial solvation. Generally speaking, one can write the measured sum-frequency intensity as:

$$I_{SFG} \propto \left|\chi^{(2)}\right|^2 \propto |\chi^{(2)}_{water} + \chi^{(2)}_{anion}|^2 \quad (2.8)$$

Here the second order susceptibility has a contribution from both the water and the anion. In the wavelength regions employed herein, far from any resonance with water, only the contribution from the anion needs to be included. Under two-photon resonance conditions, the measured sum-frequency intensity (I_{SFG}) can then be written as[4]:

$$I_{SFG} \propto \left|\chi^{(2)}_{anion}\right|^2 \propto \frac{\left|\mu_{0,n} * (\alpha_{0,n})_{TPA}\right|^2}{(\omega_{SFG} - \omega_n)^2 + \Gamma^2} \quad (2.9)$$

Here, $\mu_{0,n}$ is the dipole transition matrix and $(\alpha_{0,n})_{TPA}$ is the two-photon absorption polarizability tensor for the ground (0) and excited states (n), and Γ represents the lifetime or linewidth of the transition; ω_i represents the frequency of the SFG photon and of the transition (n), respectively. From Equation 2.9, one can appreciate the selection rules governing electronic sum-frequency generation spectroscopy. A transition must be both one-photon and two-photon active in order to generate a SF signal.

For each signal scan, a background scan is taken wherein the two input pulses are separated in time and no SF photons are generated. This background is subtracted from the spectra to account for stray light or dark charge leaking into the CCD readout. Spectra are then baseline-corrected before being normalized to the response of a non-resonant GaAs sample. The normalization corrects for different efficiencies of optics across the broadband spectrum, as well as low light intensity on the wings of the WLC pulse due to its temporal chirp.

More specific data processing and sample preparation information are included in the individual chapters to which they are relevant.

2.3 Deep UV Second Harmonic Generation Spectroscopy

The output of a commercial regenerative amplifier (Spectra Physics, 800 nm, 100 fs, 1kHz, 4 mJ/pulse) is first passed through a telescope and a series of neutral density filters to narrow the beam waist and attenuate the power. The beam is directed through a BBO crystal to frequency-double the 800 nm into 400 nm, and a 400 nm band pass filter is used to filter out any residual 800 nm. Alternatively, the 800 nm can be directed into an optical parametric amplifier, for wavelength tunability in the UV. This incident light on the surface is referred to as the "fundamental". A half-wave plate and polarizer are used to control the input polarization of light. Prior to the sample, a rotating neutral density filter wheel modulates the input intensity and a beam sampler directs ~10% of the beam to a photodiode. This serves as the "reference", wherein the input intensity of the fundamental is monitored. The fundamental light is focused onto the water surface by a UV-fused silica lens. Coherent second harmonic (SH) photons are generated in the phase-matched

direction, which is colinear with the fundamental input reflection. After the sample, the SH is collimated with a UV grade CaF_2 lens and then filtered with an excimer mirror and a Pellin-Broca prism to spatially separate the fundamental and SH beams. The SH beam is focused into a monochromator(Acton SpectraPro 2150i) and PMT (Hamamatsu, R7154PHA) for photon counting. The readout from the PMT and photodiode is detected with a gated integration system (Stanford Research Systems) for both the SH and fundamental. The experimental design for DUV-SHG is shown in Figure 2.3

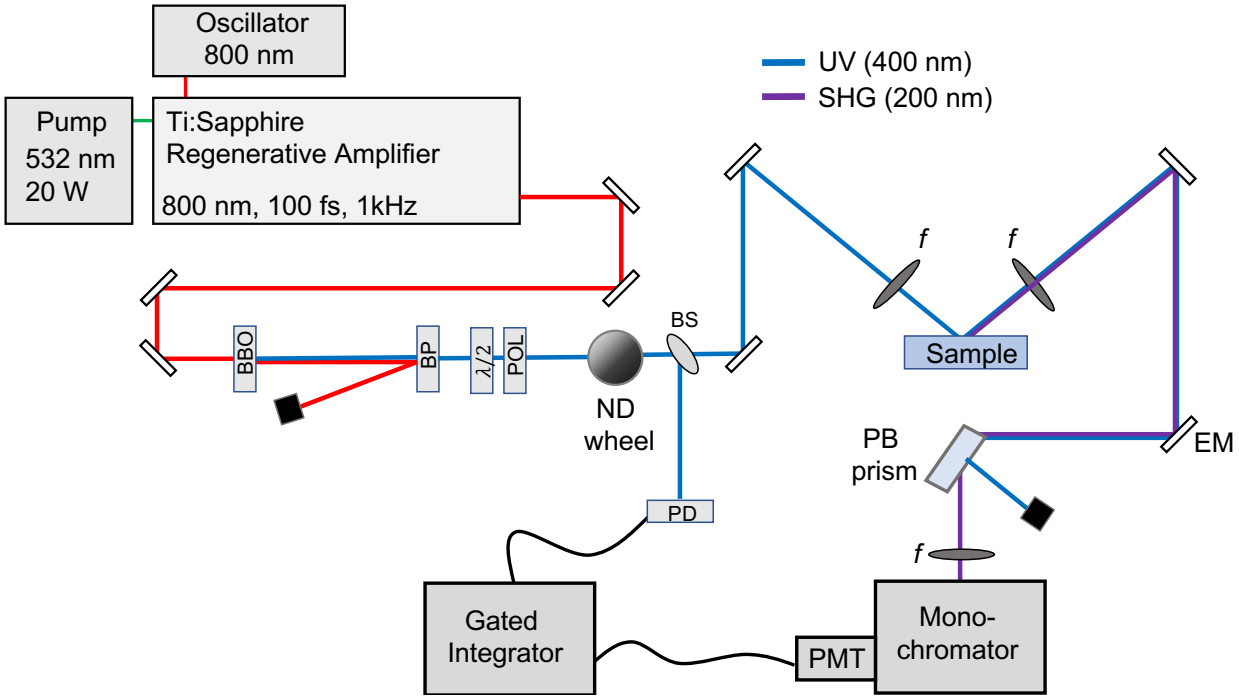

Figure 2.3 – Experimental layout for Deep UV Second Harmonic Generation spectroscopy. BBO = β-barium borate, BP = bandpass filter, $\lambda/2$ = half-wave plate, POL = 400 nm polarizer, ND = rotating neutral density filter wheel, BS = beam sampler, PD = photodiode, EM = excimer mirror, PB = Pellin-Broca prism, PMT = photomultiplier tube

In Section 2.1, it was shown that the generated SH field is dependent on the square of the input electric field. In practice, intensities are much easier to measure than electric field strengths, and the SH intensity can then be written as

$$\frac{I_{2\omega}}{I_{\omega}^{2}} = \left|\chi^{(2)}\right|^{2} \quad (2.10)$$

where $I_{2\omega}$ & I_{ω} are the intensities of the SH and the fundamental, respectively. Equation 2.10 indicates that correlating the intensity of the SH with the square of the input intensity provides a measure of the effective second-order response. Figure 2.4 shows the fundamental reference intensity and the second harmonic intensity being correlated in time.

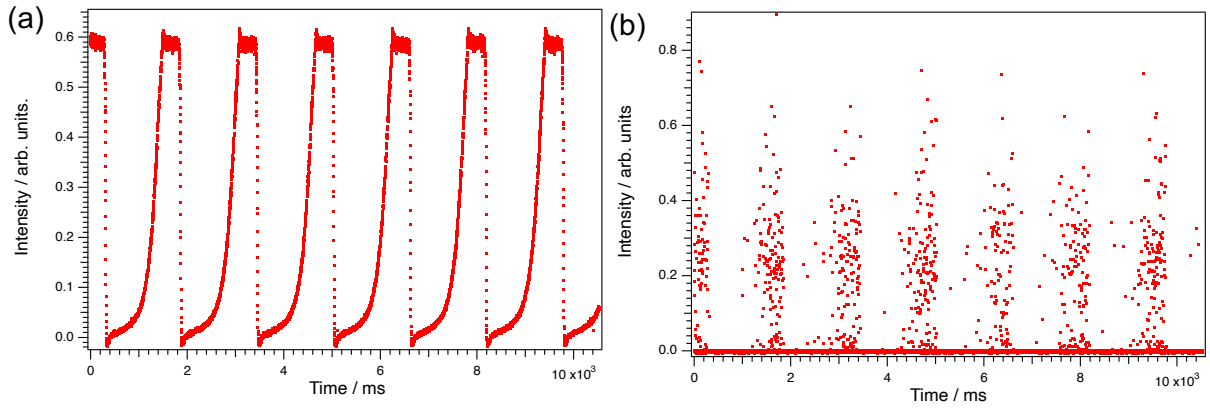

Figure 2.4 (a) Reference signal modulation and (b) Second harmonic generation intensity plotted as a function of time.

To process the SH signal, each event on the detector is treated as binary; viz. photon or no photon. This methodology allows us to use Poisson statistics to count the number of SH photons that are measured per laser pulse. Since SHG is an inherently weak process, the number of generated SH photons per laser shot is much less than one. We evaluate the SH intensity by counting the average number of SH photons $\langle k \rangle$, according to the following equation:

$$I_{2\omega} \propto \langle k \rangle \propto -\ln\left(\frac{N_{pulses}^{k=0}}{N_{pulses}^{total}}\right) \quad (2.11)$$

Here $N_{pulses}^{k=0}$ is the number of events with zero SH photons, and N_{pulses}^{total} is the total number of events. Evaluating Equation 2.11 for each value of squared input intensity (i.e. binning the reference and signal data) allows us to plot the square of the fundamental intensity against the SH intensity. As shown in Equation 2.10, fitting this

data via linear regression reveals the magnitude of $|\chi^{(2)}|^2$, and ensures that the measured response is exclusively coming from second harmonic generation and not a stray optical process.

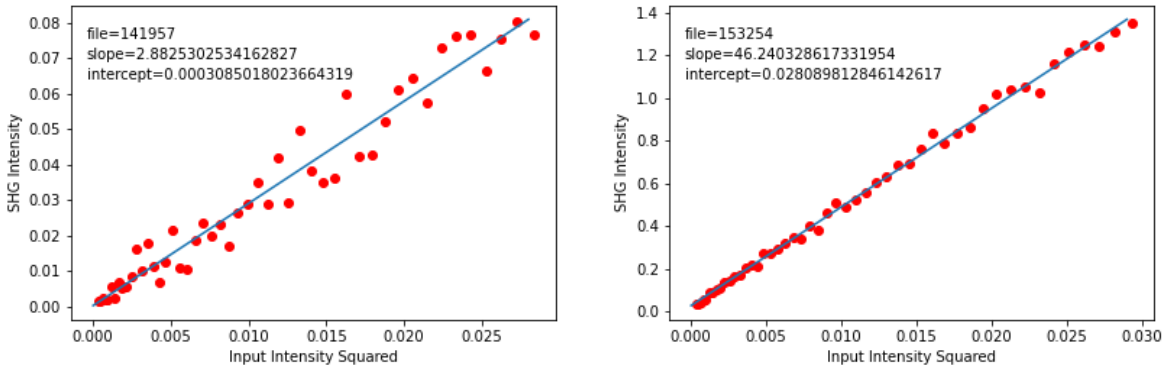

Figure 2.5 Linear regression fit of the second harmonic intensity, revealing the magnitude of $|\chi^{(2)}|^2$ for water (**left**) and 1.5 M NaSCN (**right**).

Figure 2.5 shows a linear regression fit to the SH intensity for water(left) and 1.5 M NaSCN(right). As is evident, the magnitude of $|\chi^{(2)}|^2$ is much smaller, and the correlation between fundamental and SH intensities weaker, for the pure water sample. This arises from the fact that for a SH wavelength of 200 nm, water is non-resonant. In comparison, the right-hand side of Figure 2.5 has a much larger slope value and the correlation between fundamental and SH is very strong, owing to resonant enhancement from the SCN^- CTTS transition, as well as appreciable amounts of the anion at the surface.

Specific information on sample preparation and data processing are included in the relevant chapters that follow.

2.4 Langmuir Adsorption Model

The Langmuir adsorption model has been in use for over 100 years and was originally developed to model the adsorption of gas molecules onto solid surfaces.[11] It is no surprise that Langmuir Irving won the Nobel Prize in 1932 for his work on the behavior of molecules at interfaces, given the widespread use of the Langmuir model

even today. Its application to SHG for understanding adsorption to aqueous interfaces is well established in the literature[6,7,12], and only a brief derivation and description is given here.

There are inherent assumptions built into the Langmuir model of adsorption[11] which should be discussed before deriving its mathematical form. These assumptions will be useful for developing a physical picture of ion adsorption (at least from a Langmuir perspective), and in realizing when these assumptions might break down in the systems studied in later chapters of this thesis work.

The first major assumption (1) is that adsorbate molecules bind to a flat surface. While this might be an appropriate approximation for many solids, the air-water interface is certainly far from smooth. Indeed, the neat air-water interface is well characterized by capillary wave fluctuations[13–15] and furthermore, the presence of ions at the interface can perturb these fluctuations[14]. This idea leads nicely into the second major assumption (2) that all binding sites at the surface are equivalent. One would expect that the fluctuations in solvent density at the surface as a result of capillary wave formation, would result in a broad distribution of adsorption energies. In particular, recent literature on molecular layering at the air-water interface would indicate that the depth of the adsorbate at the surface would be crucial for understanding the energetics of adsorption.[16–18] The third major assumption (3) is that there are no interactions at the interface between adsorbates in adjoining sites. This assumption seems likely to break down in the molar regimes of salt concentrations studied herein, particularly when one considers the reduced dielectric environment at the interface.[19,20] The last major assumption (4) is that only monolayer coverage is reached at the interface. For aqueous systems, the formation of electric double layers is an obvious breakdown of this assumption.[21–24] These are discussed in more detail in the relevant chapters of this thesis.

The second harmonic (SH) intensity can be written as:

$$I_{SH} \propto \left|\chi^{(2)}\right|^2 I_\omega^2 \quad (2.12)$$

Here $\chi^{(2)}$ is the second-order susceptibility and I_ω is the intensity of the fundamental light. $\chi^{(2)}$ is complex valued, and has a contribution from each component in the system:

$$\frac{I_{SH}}{I_\omega^2} \propto \left|\chi^{(2)}_{water} + \chi^{(2)}_{anion}\right|^2 \quad (2.13)$$

$\chi^{(2)}$ is dependent on the number density, N, as well as the effective hyperpolarizability, β^{eff}:

$$\frac{I_{SH}}{I_\omega^2} \propto \left|N_{water} * \beta^{eff}_{water} + N_{anion} * \beta^{eff}_{anion}\right|^2 \quad (2.14)$$

Water does not give a strong SH response, and we assume its contribution to the signal is real. However, because the anions are specifically chosen to be resonant at the SH wavelength, they have both real and imaginary components. We can group these contributions accordingly

$$\frac{I_{SH}}{I_\omega^2} \propto \left(N_{water} * \beta^{eff}_{water} + N_{anion} * Re\{\beta^{eff}_{anion}\right)^2 + \left(N_{anion} * Im\{\beta^{eff}_{anion}\}\right)^2 \quad (2.15)$$

and switch to using concentrations by dividing each term by N_{water}, since N_{anion} / N_{water} is a concentration:

$$\frac{I_{SH}}{I_\omega^2} \propto \left(\beta^{eff}_{water} + \frac{N_{anion}}{N_{water}} * Re\{\beta^{eff}_{anion}\}\right)^2 + \left(\frac{N_{anion}}{N_{water}} * Im\{\beta^{eff}_{anion}\}\right)^2 \quad (2.16)$$

We simplify the expression to:

$$\frac{I_{SH}}{I_\omega^2} \propto (A + N_s * B)^2 + (N_s * C)^2 \quad (2.17)$$

Here, the weak system response from water is represented by the non-resonant term A, B is the real component of the anion susceptibility, C is the imaginary component of the anion susceptibility, and N_s is the concentration of surface active anions.

To develop an expression for the number of surface active anions, N_s, we use the Langmuir adsorption model, wherein an anion in the bulk can exchange with a water at the surface, which is assumed to be a reversible process.

$$Anion_{bulk} + water_{surf} \leftrightarrow Anion_{surf} + water_{bulk} \quad (2.18)$$

Here, the subscripts *surf* and *bulk* refer to an anion/water molecule occupying a surface site or bulk site, respectively. We can write the equilibrium expression according to the concentration of each species as:

$$K_{ads} = \frac{[Anion]_{surf} * [water]_{bulk}}{[Anion]_{bulk} * [water]_{surf}} \quad (2.19)$$

If we assume a maximum number of surface sites, $[sites]_{max}$, the expression becomes:

$$K_{ads} = \frac{[Anion]_{surf} * [water]_{bulk}}{[Anion]_{bulk} * \left([sites]_{max} - [Anion]_{surf}\right)} \quad (2.20)$$

Rearranging for $[Anion]_{surf}$ gives:

$$N_s = [Anion]_{surf} = [sites]_{max} * \frac{[Anion]_{bulk}}{[water]_{bulk} * K_{ads}^{-1} + [Anion]_{bulk}} \quad (2.21)$$

Substituting N_s back into Equation 2.17, changing to mole fraction and using the relationship between the equilibrium adsorption rate and the Gibbs free energy gives:

$$\frac{I_{2\omega}}{I_{\omega}^2} \propto \left|\chi^{(2)}\right|^2 \propto \left(A + B\frac{X_{anion}}{(1 - X_{anion})e^{\frac{\Delta G}{RT}} + X_{anion}}\right)^2 + \left(C\frac{X_{anion}}{(1 - X_{anion})e^{\frac{\Delta G}{RT}} + X_{anion}}\right)^2 \quad (2.22)$$

This relates the observed SH intensity to the bulk anion concentration (X_{anion}) and the Gibbs free energy of adsorption (ΔG).

Figure 2.6 shows representative fits of Equation 2.22, for different values of (ΔG). Anion repulsion or weak adsorption (green and blue lines, respectively) are typically manifested as a linear increase in intensity with bulk anion concentration. Strong adsorption events (red and orange lines) are represented by a rapid rise in intensity at low anion concentration, and a subsequent asymptote as the maximum surface coverage is reached quickly.

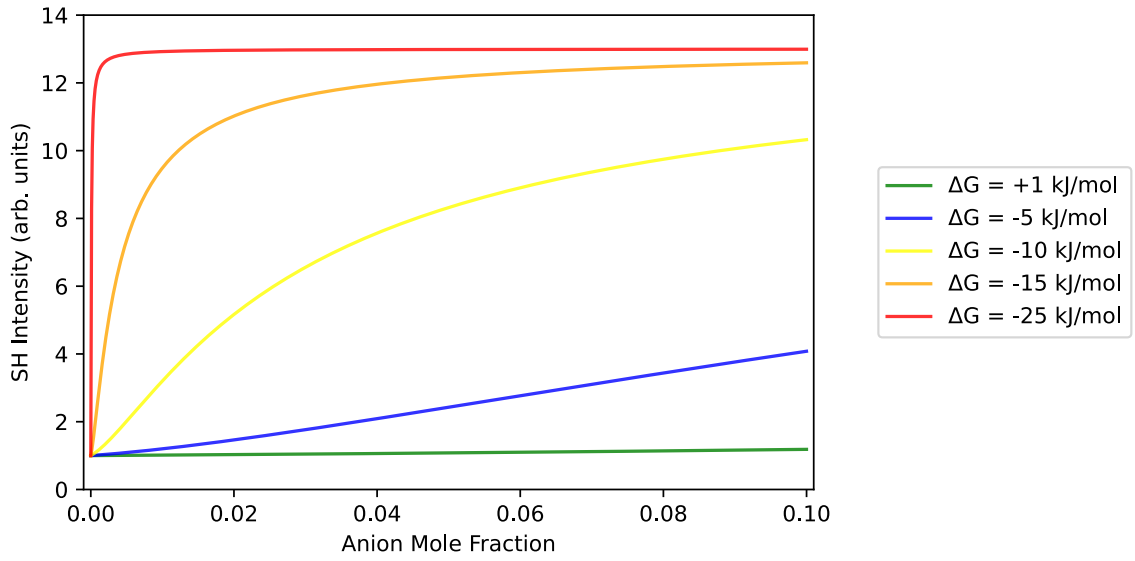

Figure 2.6 Representative Langmuir model fits from Equation 2.22. The parameters A, B, and C are all held equal to 1 and the parameter ΔG is varied.

References

(1) Bloembergen, N.; Pershan, P. S. Light Waves at the Boundary of Nonlinear Media. *Phys. Rev.* **1962**, *128* (2), 606–622. https://doi.org/10.1103/PhysRev.128.606.

(2) Shen, Y. R. Surface Contribution versus Bulk Contribution in Surface Nonlinear Optical Spectroscopy. *Appl. Phys. B* **1999**, *68* (3), 295–300. https://doi.org/10.1007/s003400050622.

(3) Robert W. Boyd. *Nonlinear Optics*; Academic Press, 2020.

(4) Moad, A. J.; Simpson, G. J. A Unified Treatment of Selection Rules and Symmetry Relations for Sum-Frequency and Second Harmonic Spectroscopies. *J. Phys. Chem. B* **2004**, *108* (11), 3548–3562. https://doi.org/10.1021/jp035362i.

(5) Lambert, A. G.; Davies, P. B.; Neivandt, D. J. Implementing the Theory of Sum Frequency Generation Vibrational Spectroscopy: A Tutorial Review. *Appl. Spectrosc. Rev.* **2005**, *40* (2), 103–145. https://doi.org/10.1081/ASR-200038326.

(6) Petersen, P. B.; Saykally, R. J. Confirmation of Enhanced Anion Concentration at the Liquid Water Surface. *Chem. Phys. Lett.* **2004**, *397* (1–3), 51–55. https://doi.org/10.1016/j.cplett.2004.08.049.

(7) Petersen, P. B.; Saykally, R. J.; Mucha, M.; Jungwirth, P. Enhanced Concentration of Polarizable Anions at the Liquid Water Surface: SHG Spectroscopy and MD

Simulations of Sodium Thiocyanide. *J. Phys. Chem. B* **2005**, *109* (21), 10915–10921. https://doi.org/10.1021/jp050864c.

(8) Rizzuto, A. M.; Irgen-Gioro, S.; Eftekhari-Bafrooei, A.; Saykally, R. J. Broadband Deep UV Spectra of Interfacial Aqueous Iodide. *J. Phys. Chem. Lett.* **2016**, *7* (19), 3882–3885. https://doi.org/10.1021/acs.jpclett.6b01931.

(9) Yamaguchi, S.; Tahara, T. Precise Electronic $\chi^{(2)}$ Spectra of Molecules Adsorbed at an Interface Measured by Multiplex Sum Frequency Generation. *J. Phys. Chem. B* **2004**, *108* (50), 19079–19082. https://doi.org/10.1021/jp045306x.

(10) Blandamer, M. J.; Fox, M. F. Theory and Applications of Charge-Transfer-to-Solvent Spectra. *Chem. Rev.* **1970**, *70* (1), 59–93. https://doi.org/10.1021/cr60263a002.

(11) Langmuir, I. THE ADSORPTION OF GASES ON PLANE SURFACES OF GLASS, MICA AND PLATINUM. *J. Am. Chem. Soc.* **1918**, *40* (9), 1361–1403. https://doi.org/10.1021/ja02242a004.

(12) Petersen, P. B.; Saykally, R. J. Probing the Interfacial Structure of Aqueous Electrolytes with Femtosecond Second Harmonic Generation Spectroscopy. *J. Phys. Chem. B* **2006**, *110* (29), 14060–14073. https://doi.org/10.1021/jp0601825.

(13) Willard, A. P.; Chandler, D. Instantaneous Liquid Interfaces. *J. Phys. Chem. B* **2010**, *114* (5), 1954–1958. https://doi.org/10.1021/jp909219k.

(14) Wang, Y.; Sinha, S.; Desai, P. R.; Jing, H.; Das, S. Ion at Air–Water Interface Enhances Capillary Wave Fluctuations: Energetics of Ion Adsorption. *J. Am. Chem. Soc.* **2018**, *140* (40), 12853–12861. https://doi.org/10.1021/jacs.8b06205.

(15) Noah-Vanhoucke, J.; Geissler, P. L. On the Fluctuations That Drive Small Ions toward, and Away from, Interfaces between Polar Liquids and Their Vapors. *Proc. Natl. Acad. Sci.* **2009**, *106* (36), 15125–15130. https://doi.org/10.1073/pnas.0905168106.

(16) Yu, C.-C.; Seki, T.; Chiang, K.-Y.; Tang, F.; Sun, S.; Bonn, M.; Nagata, Y. Polarization-Dependent Heterodyne-Detected Sum-Frequency Generation Spectroscopy as a Tool to Explore Surface Molecular Orientation and Ångström-Scale Depth Profiling. *J. Phys. Chem. B* **2022**, *126* (33), 6113–6124. https://doi.org/10.1021/acs.jpcb.2c02178.

(17) Odendahl, N. L.; Geissler, P. L. Local Ice-like Structure at the Liquid Water Surface. *J. Am. Chem. Soc.* **2022**, *144* (25), 11178–11188. https://doi.org/10.1021/jacs.2c01827.

(18) Kessler, J.; Elgabarty, H.; Spura, T.; Karhan, K.; Partovi-Azar, P.; Hassanali, A. A.; Kühne, T. D. Structure and Dynamics of the Instantaneous Water/Vapor Interface Revisited by Path-Integral and Ab Initio Molecular Dynamics Simulations. *J. Phys. Chem. B* **2015**, *119* (31), 10079–10086. https://doi.org/10.1021/acs.jpcb.5b04185.

(19) Chiang, K.-Y.; Seki, T.; Yu, C.-C.; Ohto, T.; Hunger, J.; Bonn, M.; Nagata, Y. The Dielectric Function Profile across the Water Interface through Surface-Specific Vibrational Spectroscopy and Simulations. *Proc. Natl. Acad. Sci.* **2022**, *119* (36), e2204156119. https://doi.org/10.1073/pnas.2204156119.

(20) Fumagalli, L.; Esfandiar, A.; Fabregas, R.; Hu, S.; Ares, P.; Janardanan, A.; Yang, Q.; Radha, B.; Taniguchi, T.; Watanabe, K.; Gomila, G.; Novoselov, K. S.; Geim, A. K. Anomalously Low Dielectric Constant of Confined Water. *Science* **2018**, *360* (6395), 1339–1342. https://doi.org/10.1126/science.aat4191.

(21) Tissot, H.; Olivieri, G.; Gallet, J.-J.; Bournel, F.; Silly, M. G.; Sirotti, F.; Rochet, F. Cation Depth-Distribution at Alkali Halide Aqueous Solution Surfaces. *J. Phys. Chem. C* **2015**, *119* (17), 9253–9259. https://doi.org/10.1021/jp512695c.

(22) Levin, Y.; dos Santos, A. P.; Diehl, A. Ions at the Air-Water Interface: An End to a Hundred-Year-Old Mystery? *Phys. Rev. Lett.* **2009**, *103* (25), 257802. https://doi.org/10.1103/PhysRevLett.103.257802.

(23) Li, J.; Wang, F. Surface Penetration without Enrichment: Simulations Show Ion Surface Propensities Consistent with Both Elevated Surface Tension and Surface Sensitive Spectroscopy. *J. Phys. Chem. B* **2019**, *123* (33), 7197–7203. https://doi.org/10.1021/acs.jpcb.9b04424.

(24) Olivieri, G.; Parry, K. M.; D'Auria, R.; Tobias, D. J.; Brown, M. A. Specific Anion Effects on Na^+ Adsorption at the Aqueous Solution–Air Interface: MD Simulations, SESSA Calculations, and Photoelectron Spectroscopy Experiments. *J. Phys. Chem. B* **2018**, *122* (2), 910–918. https://doi.org/10.1021/acs.jpcb.7b06981.

Chapter 3: Investigation of the Aqueous Carbonate System to the Air-water Interface

This work is adapted from Devlin, S. W.; Chen, A. A.; Jamnuch, S.; Xu, Q.; Qian, J.; Pascal, T. A.; Saykally, R. J. Agglomeration Drives the Reversed Fractionation of Aqueous Carbonate and Bicarbonate at the Air-Water Interface.ArXiv, 2023. https://doi.org/10.48550/ARXIV.2301.05786.

Amanda Chen, Sasawat Jamnuch and Professor Tod Pascal from the UC San Diego Department of Chemistry provided the MD simulations. Jian Qian and Qiang Xu from the Lawrence Berkeley National Laboratory performed the Xray calculations.

3.1 Introduction

Chemistry occurring at aqueous interfaces governs many important phenomena, e.g. reactions in atmospheric aerosols[1,2] and the uptake of gases at the ocean surface[3], as well as myriad biological processes. Reactions occurring at such an interface are often quite distinct from the same processes occurring in the corresponding bulk. Accordingly, much attention has addressed interfacial chemistry to understand the physical origins engendering these differences, with factors such as dielectric constants[4–6], unique hydrogen-bonding networks[7,8], electric double layer formation[9–11], electric fields[12], etc., being invoked to rationalize the observed behavior.

The discovery that anions with weak hydration enthalpies can have strongly enhanced concentrations in the interfacial region is a relatively new phenomenon[13], which initially contradicted classical electrostatic theory and the interpretation of many "surface sensitive" experiments, e.g. the change in surface tension of water upon addition of salt[14]. Several inconsistencies have since been reconciled, and our understanding is now much more complete, with even the detailed mechanism of adsorption for weakly-hydrated, monovalent anions to water-hydrophobe interfaces being quite well established.[15–17] However, the picture remains unclear for strongly hydrated, polyatomic ions such as CO_3^{2-} and SO_4^{2-}, which generally experience stronger image charge repulsion from the water-hydrophobe boundary. Given the importance of many strongly hydrated, polyoxy anions (e.g. CO_3^{2-}, SO_4^{2-}, PO_4^{3-}, NO_3^-, XO_3^-, X=Cl, Br, I and their respective acids) in atmospheric, environmental, and biological systems, further investigation of their behavior at the air-water interface is clearly warranted.

Our focus herein is on the centrally important carbonate system, which has been studied extensively, dating back to solubility experiments conducted over 100 years ago.[18] The hydration structure and dynamics of carbonate species have been characterized with a number of different methods, including MD simulation[19,20], quantum calculations[21–23], and X-ray spectroscopy[24–28]. Similarly, surface sensitive nonlinear spectroscopies have been used to study the behavior of these important anions. An early vibrational sum-frequency generation (vSFG) study by Tarbuck and Richmond reported that Na_2CO_3 perturbs the air-water interface more than does $NaHCO_3$; however, the authors did not comment on the relative surface affinities of the two anions.[3] Allen et al. conducted phase-sensitive measurements and found an increase in H-down oriented interfacial waters in the presence of carbonate and concluded that the sodium counter cation resides closer to the air-water interface than does the anion, and that bicarbonate resides closer to the surface than carbonate.[29] MD simulations supported these findings.[30,31] It has also been reported recently that the carbonate system does not form a well-ordered electric double layer.[32] We note that these vSFG measurements monitor solute-induced changes in the OH spectrum of water and are therefore *indirect* measures of the interfacial ion population.

Lam et al. recently reported the reversed fractionation of carbonate and bicarbonate anions at the air-water interface using Ambient Pressure Xray Photoelectron Spectroscopy (AP-XPS).[25] They found higher concentrations of doubly-charged carbonate ions than singly-charged bicarbonate in the near-interfacial region, contrasting previous surface-sensitive measurements. Without detailed theory to interpret this surprising behavior, and given that AP-XPS is not rigorously a surface-sensitive technique, we herein revisit the subject of the interfacial adsorption behavior of the carbonate system. In particular, we aim to clarify the discrepancies that exist in the literature regarding the relative surface affinity of the carbonate and bicarbonate anions at the air-water interface, and to propose a molecular-level picture for their observed surface behavior.

In this work, we employ resonantly enhanced deep-UV second harmonic generation (DUV-SHG) spectroscopy to *directly* probe the carbonate and bicarbonate anions at the air-water interface, with much higher surface specificity than the AP-XPS experiment. We find, contrary to classical electrostatic theory and in agreement with our previous AP-XPS measurements, that the doubly-charged carbonate anion

does indeed exhibit a stronger preference for the air-water interface than does the singly-charged bicarbonate anion, and quantify this through the determination of the respective Gibbs free energies of adsorption. We performed molecular dynamics simulations (MD) to develop a detailed understanding of this interfacial behavior, and computed the population distribution and thermodynamic properties of HCO_3^- and CO_3^{2-} at the air-water interface. We find that transient agglomeration, in the case of Na_2CO_3 solutions, results in the formation of near-neutral, weakly solvated ion clusters which are highly surface active. Lastly, we simulate XPS binding energies of carbonate and bicarbonate at the air-water interface to help further interpret the experimental results from our previous AP-XPS experiments.

3.2 SHG And the Langmuir Adsorption Model

To directly probe the carbonate and bicarbonate anions at the air-water interface, we use resonantly-enhanced deep-UV second harmonic generation (DUV-SHG) spectroscopy. SHG is a second-order nonlinear spectroscopic technique, wherein two photons at frequency ω combine to form one photon at frequency 2ω. Symmetry requirements under the electric dipole approximation dictate that a SH photon is only generated in a noncentrosymmetric environment (i.e an interface) and from a non-centrosymmetric molecule, rendering SHG a highly surface specific technique.[33] The SH intensity is governed by the equation:

$$I_{SH} \propto \left|\chi^{(2)}\right|^2 I_\omega^2 \quad (3.1)$$

Here, $\chi^{(2)}$ is the second-order susceptibility, and I_{SH} and I_ω are the intensities of the second harmonic and fundamental beams, respectively. Both the anions and water have their respective susceptibility tensors, and contribute to the overall signal:

$$I_{SH} \propto \left|\chi^{(2)}_{anion} + \chi^{(2)}_{water}\right|^2 I_\omega^2 \quad (3.2)$$

The molecular responses for the anion and water are complex and contain both a real (non-resonant) and an imaginary (resonant) component. In the UV, the response from water is purely real. Therefore, under the two-photon-resonant conditions employed here, the resonant term from the anion should dominate the overall measured SH intensity. In the low solute concentration regime and/or under non-

resonant conditions, the signal from water and the solute need to be considered equally, which will be discussed in more detail later. We can express the resonant term for the anion as:

$$\chi^{(2)}_{anion} \propto N_{anion} < \beta_{anion} > \quad (3.3)$$

Here β_{anion} is the orientationally averaged hyperpolarizability and N represents the number density of the anion at the interface. Equation 3 emphasizes that changes in the number density, as well as the orientation of the resonant species will change the measured SH signal.

Because the signal depends on the relative concentration of the adsorbing solute, we can apply a simple Langmuir model to fit our experimental data. The use of a Langmuir model for SHG is well established[34] and only the important features are highlighted here. For a more thorough derivation, we refer the reader to Chapter 2. We parameterize the second order susceptibility as:

$$\left|\chi^{(2)}\right|^2 \propto |A + N_s(B + iC)|^2 \quad (3.4)$$

Here, A represents the non-resonant response from water, N_s is the number density of adsorbed anion, and B and C are the non-resonant and resonant susceptibilities of the anion, respectively. N_s is determined from a kinetic description of surface exchange, and related to the bulk anion concentration, X_{SCN^-}, and Gibbs free energy of adsorption, ΔG:

$$\frac{I_{2\omega}}{I_\omega^2} = \left|\chi^{(2)}\right|^2 \propto \left(A + B\frac{X_{SCN^-}}{(1 - X_{SCN^-})e^{\frac{\Delta G}{RT}} + X_{SCN^-}}\right)^2 + \left(C\frac{X_{SCN^-}}{(1 - X_{SCN^-})e^{\frac{\Delta G}{RT}} + X_{SCN^-}}\right)^2 \quad (3.5)$$

Thus, by measuring the second harmonic intensity as a function of anion concentration, the Gibbs free energy of adsorption can be determined.

3.3 Materials and Methods

Materials: All glassware was soaked overnight in Alnochromix (Alconox Inc.) cleaning solution and rinsed thoroughly with ultrapure (18.2 MΩ) water. Solutions were prepared by dissolving reagent grade sodium carbonate (Sigma Aldrich, >99% purity) and sodium bicarbonate (Sigma Aldrich, >99% purity) in ultrapure water.

Second Harmonic Generation Spectroscopy: The experimental design has been described in detail elsewhere[1], and only a brief description is given here. The output from a Ti-S regenerative amplifier (Spectra Physics Spitfire, 4 mJ, 100fs, 1kHz) is directed through a BBO crystal to generate light at 400 nm. The 400 nm light is then focused onto the surface of the solution using a f = 100mm lens at an angle of 60° relative to the surface normal. The fundamental and SH light are collected with a collimating lens, and the fundamental light is spectrally filtered using a laser line mirror and Pellin-Broca prism. The SH photons are then detected using a gated boxcar integrator (Stanford Research Systems), a monochromator (Acton SpectraPro 2150i), and a photomultiplier (Hamamatsu, R7154PHA) for photon counting. All SHG measurements are normalized relative to the SH response of pure water. Input polarization was controlled using a half-wave plate and a polarizer.

3.4 Results / Discussion

3.4.1 Second-Harmonic Generation Spectroscopy

Figure 3.1(a) shows the bulk absorption spectra of Na_2CO_3 and $NaHCO_3$ in water at 293 K, with both anions exhibiting molecular $\pi\pi^*$transitions in the deep UV. The geometries of the carbonate and bicarbonate anions in solution have been well characterized; quantum chemical calculations[21] and neutron diffraction[35] showed that the normally planar CO_3^{2-} anion exhibits broken symmetry in aqueous solution(D_{3h} → C_{3v}) due to interactions with the solvent. Raman spectroscopy studies in solution have also concluded that the first shell solvation environment is indeed itself asymmetric.[36] These properties of the carbonate and bicarbonate anions allow us to directly probe their relative concentrations in the interfacial region. A cartoon depiction of the experimental design is shown in Figure 3.1(b).

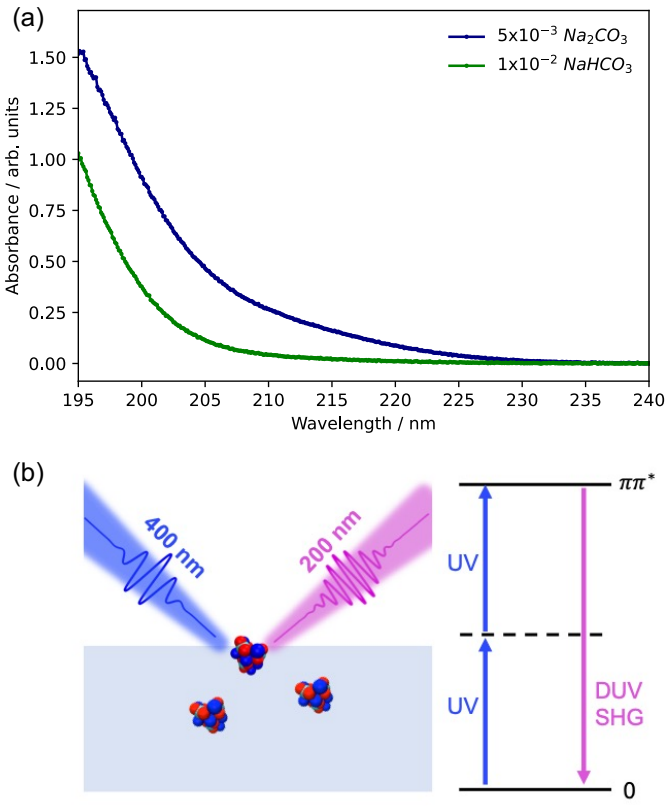

Figure 3.1: (a) Linear absorption spectra for $5x10^{-3}$M Na_2CO_3 (blue line) and $1x10^{-2}$M $NaHCO_3$ (green line) measured at 293 K. **(b)** Cartoon depiction of the experimental design showing generation of a second harmonic photon from a carbonate cluster residing at the liquid water surface. The energy level diagram highlights the resonant enhancement from being two-photon resonant with the molecular $\pi\pi^*$ transition of the carbonate and bicarbonate anions.

Figure 3.2(a) shows the normalized (relative to pure water) SH response of the carbonate anion at the air-water interface for 0-0.036 mole fraction (0-2.0 M) solutions of sodium carbonate. The intensities are measured in two polarization combinations (s-in, p-out and p-in, p-out), with both polarizations giving a fairly weak second-order response, ca. twice the response of pure water at a concentration of 2.0 M bulk concentration; this is likely due to the small extinction coefficient at 200 nm for carbonate when compared to other surface active anions such as SCN^- , which exhibits a much stronger SH response.[37] In the low concentration region from

0 – 0.0045 mole fraction (0-0.175 M), the measured SH response is slightly below or equal to that of pure water, indicating no appreciable amount of carbonate in the probe depth of SHG, as well as minimal re-orientation of interfacial water molecules.

Electrolyte solutions with normalized SHG values below the response of pure water have been observed previously in the low concentration limit, and the mechanism for this response is still debated in the literature. Explanations such as destructive interference between the resonant signal from the electrolyte and the non-resonant signal from water have been implicated[38,39]; however, more recent studies seem to point towards long range correlations extending from bulk water, induced by the electrolyte, as the cause of this behavior[40,41]. This phenomenon is most relevant for the discussion of the Jones-Ray Effect in sub-molar concentrations, and is not a focus of the present work.

Between 0.0045 – 0.018 mole fraction (0.175 – 1.0 M), the SH response begins to increase linearly with anion concentration, owing to resonant enhancement of carbonate as it accumulates in the interface, as well as alignment of interfacial water from the electric field of the anion. The latter contribution effectively increases the hyperpolarizability of water (see Eqn. 3), and is akin to a "thickening" of the interface.[42] Above 0.018 mole fraction (1.0-2.0 M), the SH response becomes asymptotic, as the surface becomes "saturated" and cannot accommodate any additional carbonate anions. The concentration range used in these experiments is limited by the solubility of sodium carbonate, which at room temperature is ~2M. The Langmuir adsorption model, as employed herein, gives an unconstrained, best fit to the data with a Gibbs free energy of adsorption of -11.1 ± 0.7 kJ/mol for both p-in, p-out and s-in, p-out polarization, with the uncertainty being one standard deviation.

In Figure 3.2(b), we compare the best fit of the Langmuir model for the carbonate anion (-11.1 ± 0.7 kJ/mol) with the output of the Langmuir model in the weak adsorption regime (-2 kJ/mol, orange line) and the repulsive regime (+2 kJ/mol, blue line). In order to obtain these fits corresponding to weak and repulsive adsorption, the Gibbs free energy was constrained to these values and the fitting parameters A,B,C were simultaneously solved for. Both the -2 and +2 kJ/mol fits increase linearly with increasing bulk anion concentration, and clearly do not adequately represent the observed curvature in the experimental data. In the weak and repulsive adsorption regime, the non-resonant parameter B increases, and the resonant parameter, C, becomes very small or even negative (see SI Table 1).

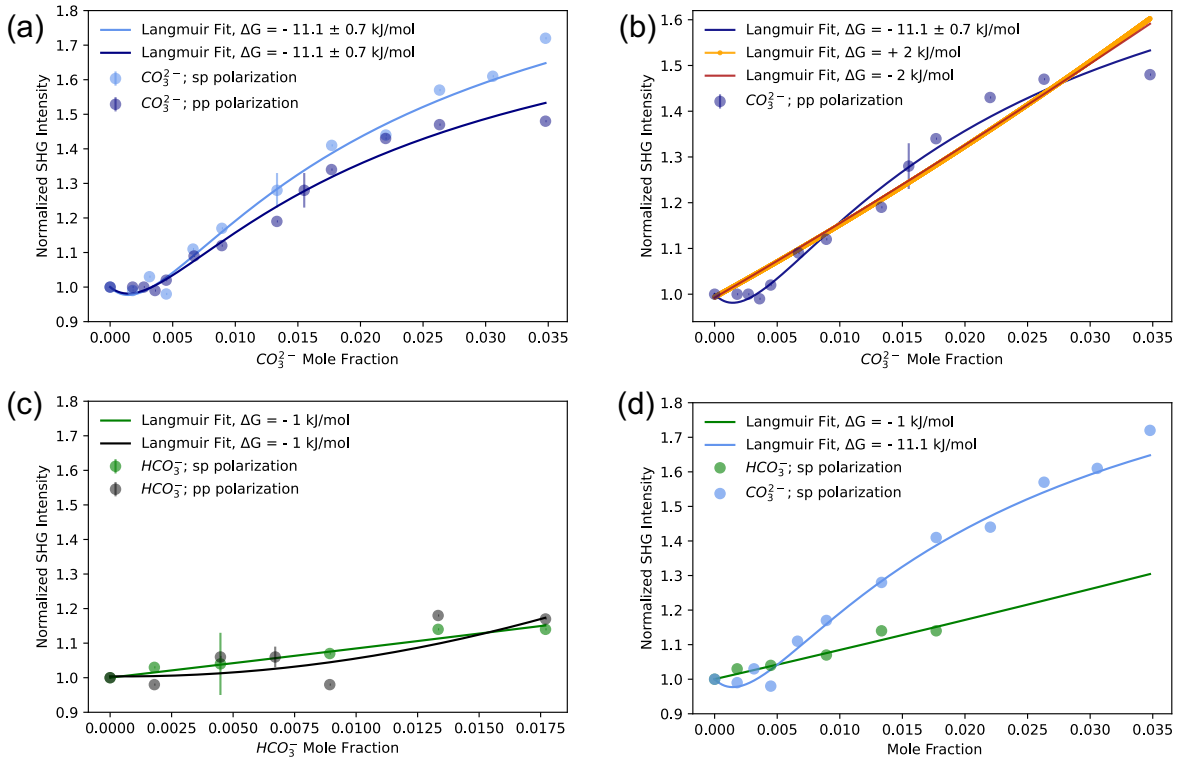

Figure 3.2: **(a)** Normalized SHG intensities for the carbonate anion at the air-water interface, measured at a SH wavelength of 200nm for *s*-in, *p*-out (light blue circles) and *p*-in, *p*-out (dark blue circles). For clarity, only one representative error bar for each data set is shown, which corresponds to one standard deviation. Each data set is fit to a Langmuir adsorption model, yielding Gibb's free energies of adsorption of -11.1 ± 0.7 kJ/mol. **(b)** Langmuir adsorption model shown for three different adsorption regimes for the carbonate anion: strong adsorption (dark blue), weak adsorption (red line), and repulsion (orange line). **(c)** Normalized SHG intensities of the bicarbonate anion at the air-water interface, measured at a SH wavelength of 200nm for *s*-in, *p*-out (green circles) and *p*-in, *p*-out (black circles). A Langmuir fit with the Gibb's free energy constrained to -1kJ/mol is shown for each data set. This value represents a minimum threshold for the Gibb's free energy. **(d)** SHG intensities for carbonate and bicarbonate. Extrapolation of the Gibbs free energy for the bicarbonate fit to concentrations of 2M reveals as SH response significantly weaker than that for carbonate.

Under the experimental conditions employed here, wherein the SH wavelength is resonant with the anion, these fitting parameters are unphysical - implying that the Langmuir model does not produce a representative fit to the data.

Figure 3.2(c) shows the normalized SH response of the bicarbonate anion from 0 – 0.0175 mole fraction (0 – 1.0 M) solutions of sodium bicarbonate. With both s- and p-input polarization, there is a weak, linear increase in the SH signal with increasing bulk anion concentration. This behavior, as mentioned above, is ascribed to a thickening of the interfacial layer via alignment of surface waters, and has been observed before in non-resonant studies of anions that are known to be repelled from the interface, e.g. the fluoride anion, F^-.[42]

A fit of the bicarbonate data to the Langmuir model does not converge, and therefore the Gibbs free energy cannot be determined from an unconstrained fit. Instead, in Figure 3.2(c), constrained fits with Gibbs free energies of -1 kJ/mol are shown for both data sets. This value of the Gibbs free energy corresponds to a weak adsorption event. More negative values of the Gibbs free energy (i.e. stronger adsorption) induce curvature in the fit that is not present in the experimental data; therefore, an upper limit of -1 kJ/mol is established. Less negative, and positive, values of the Gibb's free energy produce results that are identical to those of the -1 kJ/mol fit, viz. a shallow linear increase with increasing anion concentration. Therefore, while we cannot quantitatively determine the Gibbs free energy of adsorption for the bicarbonate anion, we can establish a range of values, with an upper limit of -1 kJ / mol, and less favorable values of adsorption being more likely.

Our DUV-SHG measurements indicate that the carbonate anion has a much stronger surface affinity for the air-water interface than does the bicarbonate anion, as shown in Figure 3.2d. On the basis of hydration free energy ($\Delta G_{hyd}(CO_3^{2-}) = -1315\frac{kJ}{mol}$ and $\Delta G_{hyd}(HCO_3^-) = -335\frac{kJ}{mol}$)[43], this behavior is indeed puzzling. It has been shown by both experiment and theory, that weakly-hydrated anions tend to be surface active, whereas strongly hydrated anions tend to be surface repelled, roughly following the Hofmeister series.[44,45] For example, anions that have been shown to have enhanced concentrations in the interfacial region, e.g. I^- and SCN^- , have hydration free energies of ca. -280 kJ/mol. The surface adsorption of such a strongly-hydrated anion as carbonate indeed seems unlikely, and we turn to MD simulations of these systems to help interpret these surprising experimental results.

3.4.2 Molecular Dynamics Simulations

Our analysis of molecular dynamics trajectories shows significant differences in the solvation structure between HCO_3^- and CO_3^{2-} species. Specifically, we find for solutions of Na_2CO_3 that CO_3^{2-} tends to form agglomerates with Na^+, resulting in clusters or chains, while in solutions of $NaHCO_3$, the HCO_3^- anion remains isolated (Figure 3.3(a) and 3.3(b)).

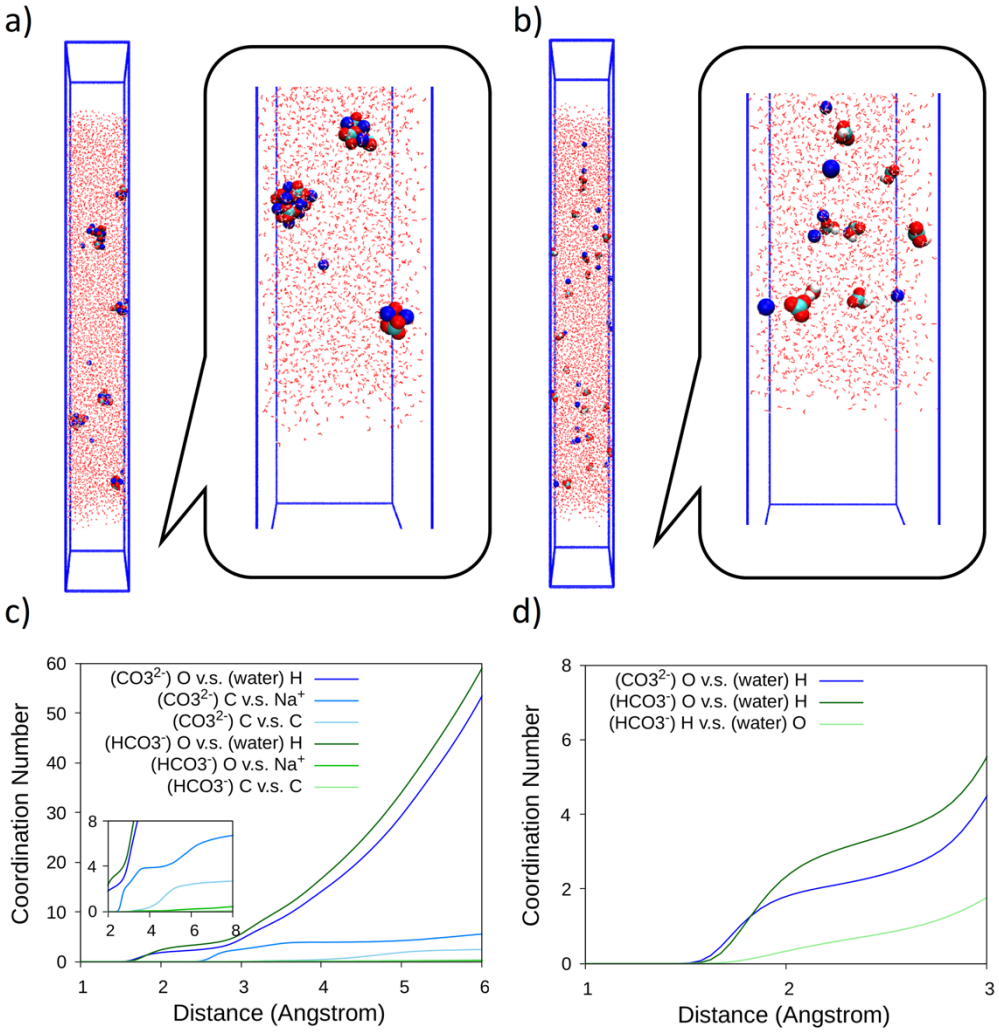

Figure 3.3: Molecular dynamics simulation snapshots for solutions of **(a)** Na_2CO_3 and **(b)** $NaHCO_3$.Panel **(a)** highlights the formation of agglomerates in solution. **(c)** and **(d)** show the coordination number for different atoms in carbonate and bicarbonate solution as a function of radial distance.

In Figures 3.3(c) and 3.3(d), we plot the coordination number of different atoms in carbonate and bicarbonate solutions as a function of radial distance. The CO_3^{2-} molecules on average have much higher coordination number with Na^+ and neighboring carbonates than does HCO_3^-. Additionally, Figure 3.3(d) highlights that the coordination numbers on average for both CO_3^{2-} and $HCO_3^-$with water are equal at short distances (up to 2 Å), and then larger for HCO_3^- at longer distances.

Given the large difference in hydration free energy for these anions, one would expect the carbonate-water coordination number to be significantly higher than for bicarbonate. Indeed, this has been observed in the radial distribution functions for carbonate and bicarbonate anions from MD simulation, with no counter cations present in the solutions.[20] The observed difference results from increased electron density on the oxygens of carbonate, coupled with higher prevalence of sodium cations, which compete with water for interaction in the solvation environment. In the case of bicarbonate, which has reduced electron density and half the number of sodium cations, interaction with the water is more likely. This behavior can be explained through the formation of a weakly solvated agglomerate for CO_3^{2-}. The $Na^+|\,CO_3^{2-}$ agglomerate, which is relatively neutral and weakly hydrated, leads to a higher propensity for the interface relative to the charged HCO_3^-.

That this agglomerate shows higher surface propensity than its non-clustered, charged counterpart, as well as bicarbonate, is in agreement with current descriptions of ion adsorption. Saykally and Geissler have shown that there is an enthalpic benefit for weakly-solvated ions to partition to the air-water interface, viz the shedding of one or two solvating waters which can then form stronger hydrogen bonds as part of the bulk water network. How capillary waves are influenced in the presence of this large agglomerate is still an open question, and could have important consequences for processes such as gas adsorption onto the liquid surface and evaporation kinetics.

Further insights into the surface enhancement of CO_3^{2-} were provided by means of 2D accelerated dynamics simulations. We consider a 2D free energy surface defined by the distance of the center of mass of a carbonate ion to the interface (Z = 0) and the C – C coordination number of the carbonate species given by Equation (3.6)

$$\sum_i \sum_{j \neq i} \frac{1-\left(\frac{r_{ij}-d_0}{r_0}\right)^n}{1-\left(\frac{r_{ij}-d_0}{r_0}\right)^m} \qquad (3.6)$$

The 2D free energy diagrams are shown in Figure 3.4. The energy requirement for fully solvated, isolated carbonate species to move from the bulk region to the air-water interface is lower in the case of CO_3^{2-}. This is due to the thermodynamically favorable formation of agglomerates, which leads to a lower energy barrier. In addition, their final agglomerated state is more stable than the HCO_3^- counterpart.

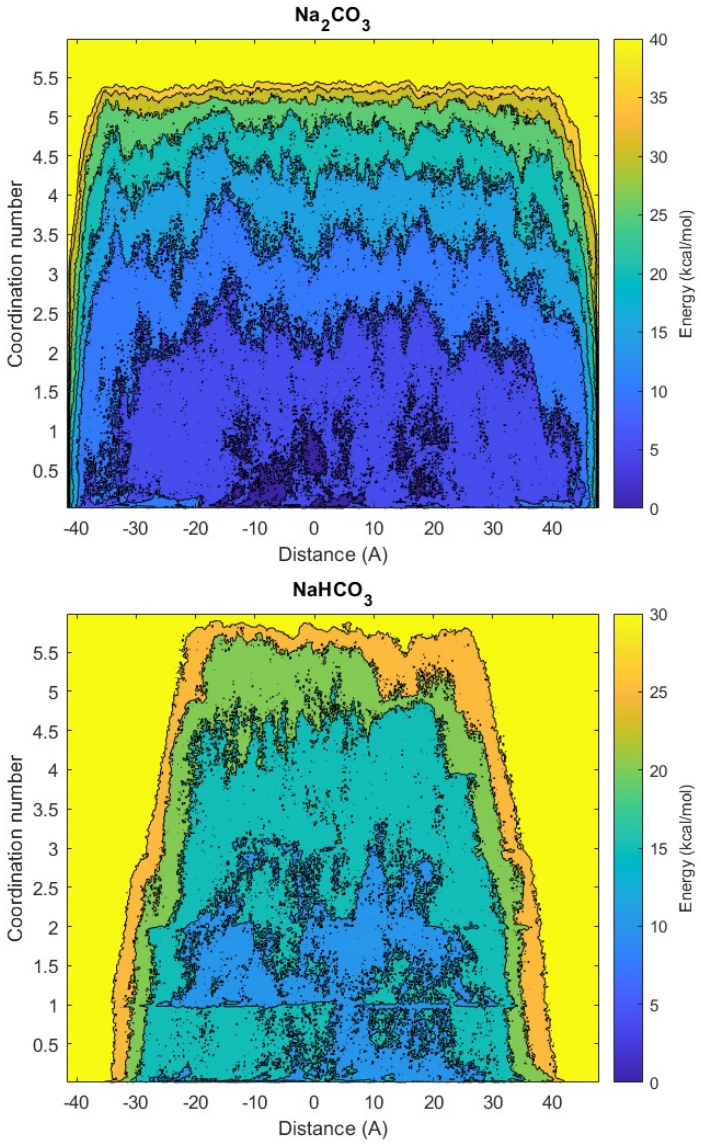

Figure 3.4: 2D Free energy surface of carbonate species as a function of distance from the bulk and coordination number. The coordination number is defined as the number of carbon atoms with in a distance of 3.5 Å.

We find a propensity for the carbonate species to agglomerate near the interface, forming near-neutral 2 – 3 Na^+/CO_3^{2-} clusters. These clusters exist in a

steady-state equilibrium with more extended, polymer-like chains. The chain state is driven by the binding of water molecules but is less favored at room temperature. Near the interface, the agglomerates incur a reduced H-bonding penalty, since interfacial waters are less tightly bound and have higher entropy, facilitating the carbonate agglomerates existence at the interface. On the other hand, due to the singly-charged bicarbonate's reduced electrostatic binding, it remains isolated and thus repelled from the surface. Therefore, we establish that the local nanostructure of the carbonate anion plays a crucial role in the final solvation state at the interface.

3.4.3 Confirmation of AP-XPS Measurements

As mentioned earlier, Lam et al. used AP-XPS to directly probe the carbon K-edge of

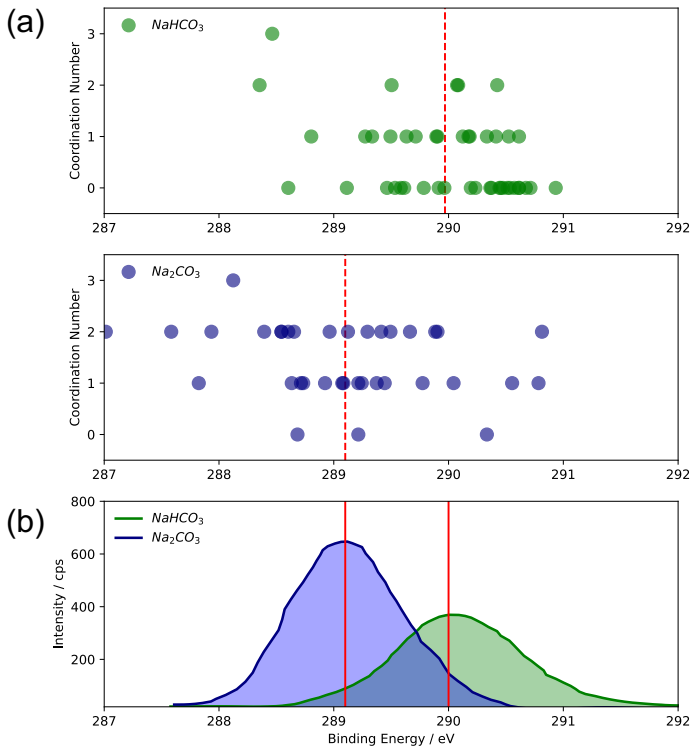

Figure 3.5: (a) Simulated XPS binding energies for C(1s) excitation of carbonate and bicarbonate at the air-water interface. Individual data points indicate the calculated binding energy and the associated coordination number to the anion. Calculated binding energies are "energy-aligned" to the experimental carbonate peak at 289.1 eV. **(b)** Xray Photoemission C(1s) binding energies with an incident photon energy of

490 eV, from 0.5 M solutions of $NaHCO_3$ and Na_2CO_3. Data in the bottom panel is reproduced from Lam et al. with permission from the authors.[25]

the carbonate and bicarbonate anions at the air-water interface and measure their relative concentrations (Figure 3.5(b)).[25] By tuning the input photon energy, they exploited different attenuation lengths of the emitted photoelectron and were able to achieve depth profiling as shallow as ~2 nm. Their findings agreed with those of the present study, viz. that CO_3^{2-} is more prevalent in the interface than HCO_3^- . However, as was noted above, AP-XPS probes deeper into the interface than do second-order spectroscopies. Even with a minimum electron attenuation length of 2 nm, there is significant signal measured from probe depths as deep as 5 nm.

An important consideration in XPS is the local environment of the excited atom, which has a significant effect on the measured binding energy. Given the different solvation environments between the bulk and surface, one might expect surface effects to modulate the spectra, viz binding energy shifts or transition narrowing/broadening. These shifts could influence the spectral fitting and thereby the relative concentrations of carbonate/bicarbonate reported by Lam et al. In order to address this concern, we calculate the C K-edge binding energies for carbonate and bicarbonate at the air-water interface, shown in Figure 3.5(a). Our calculations reveal that the XPS spectra were invariant to displacement of the anion relative to the air-water interface, as well as to the coordination number of the carbonate species. In Figure 3.5b (bottom panel) the AP-XPS spectra from Lam et al are reproduced. The relative shift between the experimental carbonate/bicarbonate spectral signatures agrees well with the shift in the calculated binding energies, with a difference of only ~0.1 eV, indicating indeed that the spectral fitting and relative concentrations reported by Lam are of the distinct carbonate/bicarbonate peaks, and not some convolution of the two due to spectral shifts. These findings imply that the results of the experiment are mainly dictated by the thermodynamics properties and concentration of carbonate species at the interface.

3.5 Implications for Atmospheric, Environmental, and Biological Sciences:

The relative partitioning of the carbonate and bicarbonate ions to the air-water interface is of significant environmental and atmospheric importance, for example in atmospheric aerosol droplet and ocean-surface chemistry. A key consideration to this subject, which has not been discussed in the present work, is the adsorption and dissolution of atmospheric CO_2 from the gas phase. We have previously addressed the solvation and hydrolysis of the species involved in this process by X-ray absorption spectroscopy[24,26,27], and molecular simulations have highlighted the importance that the interface plays in the adsorption of a polyoxy anion to liquid surfaces.[46]

The ocean serves as a large sink of CO_2 from the atmosphere, with approximately 30% of all anthropogenic CO_2 emissions being absorbed[47,48]. Following solvation into the liquid, carbon dioxide gas hydrolyzes to form carbonic acid, which can further exchange protons to form bicarbonate and carbonate, which is a pH dependent process[49]:

$$H_2CO_3(aq) + H_2O \leftrightarrow HCO_3^-(aq) + H_3O^+(aq) \quad (pK_a = 6.4) \quad (3.7)$$
$$HCO_3^-(aq) + H_2O \leftrightarrow CO_3^{2-}(aq) + H_3O^+(aq) \; (pK_a = 10.3\,) \quad (3.8)$$

Thus, an increase in atmospheric CO_2 could greatly impact marine ecosystems via ocean acidification, as given by Equations 3.7and 3.8 [50,51], and will shift the ratio of carbonate and bicarbonate anions present in ocean waters and at the air-ocean interface.

While the ocean has a large degree of buffering capacity, this effect could be quite drastic inside of aerosol droplets, which have high surface area to volume ratios. We have shown here that carbonate resides at the interface in higher quantity than does bicarbonate, and expect this partitioning to play an important role in influencing aerosol chemistry. It has been postulated that reaction kinetics can be enhanced at the surfaces of aerosol droplets[52,53], hence, the change in pH inside of droplets (and subsequent change in surface composition/structure) could disrupt or potentially further enhance these fact reactions. Furthermore, since mammalian respiration systems are also dependent on the buffering capacity of the carbonate system and help to regulate changes in blood pH, a rigorous understanding of carbonate and bicarbonate affinities for, and reactions at, the air-water interface would further illuminate these important topics.

3.6 Conclusions

In this work, we employed resonantly-enhanced DUV-SHG to directly probe the carbonate and bicarbonate anions at the air-water interface. By fitting the concentration dependence of the SH signal with a Langmuir adsorption model, we determined that the doubly-charged carbonate anion adsorbs more strongly to the surface than does singly-charged bicarbonate, in conflict with widely used models and general expectations. These measurements support our previous study of the carbonate system conducted by AP-XPS. We also describe MD simulations, which revealed that agglomerate formation of the highly charged $CO_3^{2-}$with Na^+ counterions is the driving force for its surface propensity, and that this same behavior is not found for the singly charged HCO_3^-. We hope that these new results will inspire further experiments and modeling for deeper insight into this vitally important chemical system.

References

(1) Jubb, A. M.; Hua, W.; Allen, H. C. Organization of Water and Atmospherically Relevant Ions and Solutes: Vibrational Sum Frequency Spectroscopy at the Vapor/Liquid and Liquid/Solid Interfaces. *Acc. Chem. Res.* **2012**, *45* (1), 110–119.

(2) Prophet, A.; Wilson, K. Competitive Adsorption and Reaction at the Air-Water Interface Studied by Iodide Ozonolysis in Microdroplets. **2022**.

(3) Tarbuck, T. L.; Richmond, G. L. Adsorption and Reaction of CO2 and SO2 at a Water Surface. *J. Am. Chem. Soc.* **2006**, *128* (10), 3256–3267.

(4) Sarhangi, S. M.; Waskasi, M. M.; Hashemianzadeh, S. M.; Matyushov, D. V. Effective Dielectric Constant of Water at the Interface with Charged C60 Fullerenes. *J. Phys. Chem. B* **2019**, *123* (14), 3135–3143.

(5) Cox, S. J.; Geissler, P. L. Dielectric Response of Thin Water Films: A Thermodynamic Perspective. *ArXiv Prepr. ArXiv220300575* **2022**.

(6) Fumagalli, L.; Esfandiar, A.; Fabregas, R.; Hu, S.; Ares, P.; Janardanan, A.; Yang, Q.; Radha, B.; Taniguchi, T.; Watanabe, K.; others. Anomalously Low Dielectric Constant of Confined Water. *Science* **2018**, *360* (6395), 1339–1342.

(7) Odendahl, N. L.; Geissler, P. L. Local Ice-like Structure at the Liquid Water Surface. *ArXiv Prepr. ArXiv220205883* **2022**.

(8) Pezzotti, S.; Galimberti, D. R.; Gaigeot, M.-P. 2D H-Bond Network as the Topmost Skin to the Air--Water Interface. *J. Phys. Chem. Lett.* **2017**, *8* (13), 3133–3141.

(9) Zhang, X.-X.; Li, X.-H.; Chen, M. Role of the Electric Double Layer in the Ice Nucleation of Water Droplets under an Electric Field. *Atmospheric Res.* **2016**, *178*, 150–154.

(10) Ong, S.; Zhao, X.; Eisenthal, K. B. Polarization of Water Molecules at a Charged Interface: Second Harmonic Studies of the Silica/Water Interface. *Chem. Phys. Lett.* **1992**, *191* (3–4), 327–335.

(11) Zhao, X.; Ong, S.; Eisenthal, K. B. Polarization of Water Molecules at a Charged Interface. Second Harmonic Studies of Charged Monolayers at the Air/Water Interface. *Chem. Phys. Lett.* **1993**, *202* (6), 513–520.

(12) Hao, H.; Leven, I.; Head-Gordon, T. Can Electric Fields Drive Chemistry for an Aqueous Microdroplet? *Nat. Commun.* **2022**, *13* (1), 1–8.

(13) Jungwirth, P.; Tobias, D. J. Molecular Structure of Salt Solutions: A New View of the Interface with Implications for Heterogeneous Atmospheric Chemistry. *J. Phys. Chem. B* **2001**. https://doi.org/10.1021/jp012750g.

(14) Onsager, L.; Samaras, N. N. T. The Surface Tension of Debye-Hückel Electrolytes. *J. Chem. Phys.* **1934**, *2* (8), 528–536.

(15) McCaffrey, D. L.; Nguyen, S. C.; Cox, S. J.; Weller, H.; Alivisatos, A. P.; Geissler, P. L.; Saykally, R. J. Mechanism of Ion Adsorption to Aqueous Interfaces: Graphene/Water vs. Air/Water. *Proc. Natl. Acad. Sci.* **2017**, *114* (51), 13369–13373.

(16) Otten, D. E.; Shaffer, P. R.; Geissler, P. L.; Saykally, R. J. Elucidating the Mechanism of Selective Ion Adsorption to the Liquid Water Surface. *Proc. Natl. Acad. Sci.* **2012**, *109* (3), 701–705.

(17) Devlin, S. W.; Benjamin, I.; Saykally, R. J. On the Mechanisms of Ion Adsorption to Aqueous Interfaces: Air-Water vs. Oil-Water. *Proc. Natl. Acad. Sci.* **2022**, *119* (42), e2210857119.

(18) Cameron, F. K.; Seidell, A. Solubility of Calcium Carbonate in Aqueous Solutions of Certain Electrolytes in Equilibrium with Atmospheric Air. *J. Phys. Chem.* **2002**, *6* (1), 50–56.

(19) Yadav, S.; Chandra, A. Structural and Dynamical Nature of Hydration Shells of the Carbonate Ion in Water: An Ab Initio Molecular Dynamics Study. *J. Phys. Chem. B* **2018**, *122* (4), 1495–1504.

(20) Kumar, P. P.; Kalinichev, A. G.; Kirkpatrick, R. J. Hydrogen-Bonding Structure and Dynamics of Aqueous Carbonate Species from Car- Parrinello Molecular Dynamics Simulations. *J. Phys. Chem. B* **2009**, *113* (3), 794–802.

(21) Vchirawongkwin, V.; Sato, H.; Sakaki, S. RISM-SCF-SEDD Study on the Symmetry Breaking of Carbonate and Nitrate Anions in Aqueous Solution. *J. Phys. Chem. B* **2010**, *114* (32), 10513–10519.

(22) Tho, N. M.; Ha, T. K. A Theoretical Study of the Formation of Carbonic Acid from the Hydration of Carbon Dioxide: A Case of Active Solvent Catalysis. *J. Am. Chem. Soc.* **1984**, *106* (3), 599–602.

(23) Kumar, P. P.; Kalinichev, A. G.; Kirkpatrick, R. J. Dissociation of Carbonic Acid: Gas Phase Energetics and Mechanism from Ab Initio Metadynamics Simulations. *J. Chem. Phys.* **2007**, *126* (20), 204315.

(24) England, A. H.; Duffin, A. M.; Schwartz, C. P.; Uejio, J. S.; Prendergast, D.; Saykally, R. J. On the Hydration and Hydrolysis of Carbon Dioxide. *Chem. Phys. Lett.* **2011**, *514* (4–6), 187–195.

(25) Lam, R. K.; Smith, J. W.; Rizzuto, A. M.; Karsl\io\uglu, O.; Bluhm, H.; Saykally, R. J. Reversed Interfacial Fractionation of Carbonate and Bicarbonate Evidenced by X-Ray Photoemission Spectroscopy. *J. Chem. Phys.* **2017**, *146* (9), 94703.

(26) Lam, R. K.; England, A. H.; Sheardy, A. T.; Shih, O.; Smith, J. W.; Rizzuto, A. M.; Prendergast, D.; Saykally, R. J. The Hydration Structure of Aqueous Carbonic Acid from X-Ray Absorption Spectroscopy. *Chem. Phys. Lett.* **2014**, *614*, 282–286.

(27) Lam, R. K.; England, A. H.; Smith, J. W.; Rizzuto, A. M.; Shih, O.; Prendergast, D.; Saykally, R. J. The Hydration Structure of Dissolved Carbon Dioxide from X-Ray Absorption Spectroscopy. *Chem. Phys. Lett.* **2015**, *633*, 214–217.

(28) Brown, M. A.; Lee, M.-T.; Kleibert, A.; Ammann, M.; Giorgi, J. B. Ion Spatial Distributions at the Air--and Vacuum--Aqueous K2CO3 Interfaces. *J. Phys. Chem. C* **2015**, *119* (9), 4976–4982.

(29) Hua, W.; Chen, X.; Allen, H. C. Phase-Sensitive Sum Frequency Revealing Accommodation of Bicarbonate Ions, and Charge Separation of Sodium and Carbonate Ions within the Air/Water Interface. *J. Phys. Chem. A* **2011**, *115* (23), 6233–6238.

(30) Ozdemir, O.; Karakashev, S. I.; Nguyen, A. V; Miller, J. D. Adsorption of Carbonate and Bicarbonate Salts at the Air--Brine Interface. *Int. J. Miner. Process.* **2006**, *81* (3), 149–158.

(31) Du, H.; Liu, J.; Ozdemir, O.; Nguyen, A. V; Miller, J. D. Molecular Features of the Air/Carbonate Solution Interface. *J. Colloid Interface Sci.* **2008**, *318* (2), 271–277.

(32) Roy, S.; Mondal, J. A. Kosmotropic Electrolyte (Na2CO3, NaF) Perturbs the Air/Water Interface through Anion Hydration Shell without Forming a Well-Defined Electric Double Layer. *J. Phys. Chem. B* **2021**, *125* (16), 3977–3985.

(33) Boyd, R. W. *Nonlinear Optics*; Academic press, 2020.

(34) Petersen, P. B.; Saykally, R. J. Confirmation of Enhanced Anion Concentration at the Liquid Water Surface. *Chem. Phys. Lett.* **2004**. https://doi.org/10.1016/j.cplett.2004.08.049.

(35) Kameda, Y.; Sasaki, M.; Hino, S.; Amo, Y.; Usuki, T. Neutron Diffraction Study on the Hydration Structure of Carbonate Ion by Means of 12C/13C Isotopic Substitution Method. *Phys. B Condens. Matter* **2006**, *385*, 279–281.

(36) Rudolph, W. W.; Fischer, D.; Irmer, G. Vibrational Spectroscopic Studies and Density Functional Theory Calculations of Speciation in the CO2—Water System. *Appl. Spectrosc.* **2006**, *60* (2), 130–144.

(37) Devlin, S. W.; McCaffrey, D. L.; Saykally, R. J. Characterizing Anion Adsorption to Aqueous Interfaces: Toluene--Water versus Air--Water. *J. Phys. Chem. Lett.* **2021**, *13*, 222–228.

(38) Petersen, P. B.; Johnson, J. C.; Knutsen, K. P.; Saykally, R. J. Direct Experimental Validation of the Jones--Ray Effect. *Chem. Phys. Lett.* **2004**, *397* (1–3), 46–50.

(39) Petersen, P. B.; Saykally, R. J. Probing the Interfacial Structure of Aqueous Electrolytes with Femtosecond Second Harmonic Generation Spectroscopy. ACS Publications 2006.

(40) Okur, H. I.; Chen, Y.; Wilkins, D. M.; Roke, S. The Jones-Ray Effect Reinterpreted: Surface Tension Minima of Low Ionic Strength Electrolyte Solutions Are Caused by Electric Field Induced Water-Water Correlations. *Chem. Phys. Lett.* **2017**, *684*, 433–442.

(41) Chen, Y.; Okur, H. I.; Gomopoulos, N.; Macias-Romero, C.; Cremer, P. S.; Petersen, P. B.; Tocci, G.; Wilkins, D. M.; Liang, C.; Ceriotti, M.; others.

Electrolytes Induce Long-Range Orientational Order and Free Energy Changes in the H-Bond Network of Bulk Water. *Sci. Adv.* **2016**, *2* (4), e1501891.

(42) Bian, H.; Feng, R.; Xu, Y.; Guo, Y.; Wang, H. Increased Interfacial Thickness of the NaF, NaCl and NaBr Salt Aqueous Solutions Probed with Non-Resonant Surface Second Harmonic Generation (SHG). *Phys. Chem. Chem. Phys.* **2008**, *10* (32), 4920–4931.

(43) Marcus, Y. Thermodynamics of Solvation of Ions. Part 5.—Gibbs Free Energy of Hydration at 298.15 K. *J. Chem. Soc. Faraday Trans.* **1991**, *87* (18), 2995–2999.

(44) Jungwirth, P.; Tobias, D. J. Specific Ion Effects at the Air/Water Interface. *Chem. Rev.* **2006**, *106* (4), 1259–1281.

(45) Jubb, A. M.; Hua, W.; Allen, H. C. Environmental Chemistry at Vapor/Water Interfaces: Insights from Vibrational Sum Frequency Generation Spectroscopy. *Annu Rev Phys Chem* **2012**, *63* (1), 107–130.

(46) Galib, M.; Limmer, D. T. Reactive Uptake of N2O5 by Atmospheric Aerosol Is Dominated by Interfacial Processes. *Science* **2021**, *371* (6532), 921–925.

(47) Sabine, C. L.; Feely, R. A.; Gruber, N.; Key, R. M.; Lee, K.; Bullister, J. L.; Wanninkhof, R.; Wong, C. S. L.; Wallace, D. W. R.; Tilbrook, B.; others. The Oceanic Sink for Anthropogenic CO2. *science* **2004**, *305* (5682), 367–371.

(48) Gruber, N.; Clement, D.; Carter, B. R.; Feely, R. A.; Van Heuven, S.; Hoppema, M.; Ishii, M.; Key, R. M.; Kozyr, A.; Lauvset, S. K.; others. The Oceanic Sink for Anthropogenic CO2 from 1994 to 2007. *Science* **2019**, *363* (6432), 1193–1199.

(49) Langmuir, D. Aqueous Environmental. *Geochem. Prentice Hall Up. Saddle River NJ* **1997**, *600*.

(50) Hoegh-Guldberg, O.; Poloczanska, E. S.; Skirving, W.; Dove, S. Coral Reef Ecosystems under Climate Change and Ocean Acidification. *Front. Mar. Sci.* **2017**, *4*, 158.

(51) Cao, L.; Caldeira, K.; Jain, A. K. Effects of Carbon Dioxide and Climate Change on Ocean Acidification and Carbonate Mineral Saturation. *Geophys. Res. Lett.* **2007**, *34* (5).

(52) Lee, J. K.; Kim, S.; Nam, H. G.; Zare, R. N. Microdroplet Fusion Mass Spectrometry for Fast Reaction Kinetics. *Proc. Natl. Acad. Sci.* **2015**, *112* (13), 3898–3903.

(53) Lee, J. K.; Banerjee, S.; Nam, H. G.; Zare, R. N. Acceleration of Reaction in Charged Microdroplets. *Q. Rev. Biophys.* **2015**, *48* (4), 437–444.

Chapter 4: Ion Adsorption to Water-Hydrophobe Interfaces

This chapter is adapted with permission from Devlin, S. W.; McCaffrey, D. L.; Saykally, R. J. *J. Phys. Chem. Lett.* **2022,** 13, 1, 222-228. and Devlin, S. W.; Benjamin, I.; Saykally, R. J. *Proc. Natl. Acad. Sci.* **2022,** 119 (42), e2210857119.

Molecular dynamics simulations were conducted by Professor Ilan Benjamin from the UC Santa Cruz Department of Chemistry.

4.1 Introduction

Over the last two decades, our understanding of the nature of aqueous interfaces has evolved dramatically. In contradiction to recently prevailing "conventional wisdom", it is now well-accepted that certain ions preferentially adsorb to the interfacial region, and can even have enhanced concentrations relative to the bulk.[1,2] That this ion behavior can have profound effects on the chemistry observed in the natural world is obvious. For example, the depletion of ozone at the surface of arctic sea ice[3,4], the formation of acid rain and reactions in atmospheric aerosols[5,6], and the uptake of CO_2 and other gases at the ocean surface[7] are all dynamic processes influenced by ion adsorption, not to mention myriad biological processes. Any attempt to understand these, and other, important systems must first establish a detailed understanding of the fundamental behavior of ions at interfaces.

To this end, nonlinear spectroscopies have been essential. Most commonly, the water structure adjacent to a hydrophobic phase is studied via vibrational sum-frequency generation, and chemical information is inferred by monitoring changes in the OH spectrum[8–13], as has been demonstrated by the Shen, Richmond, Allen, Roke, and Bonn groups, among others. An alternative approach is to directly probe a suitable resonant ionic chromophore that resides in the interfacial layer, which can then yield fundamental thermodynamic information regarding ion adsorption and solvation structure.[14–20]

In addition, theoretical modeling of these systems has proven to be crucial for interpreting the spectroscopic data and developing a detailed chemical understanding of these interfaces. Along with the work of Jungwirth and Tobias, early theoretical studies focused on polarizability as the main driving force of ion adsorption.[21,22] Subsequently, more nuanced descriptions of ion adsorption included factors such as size, charge, volume exclusion, hydration enthalpy, and more.[1,21,23–26] The challenge

of uncoupling these parameters makes elucidating the forces driving ions to the interface a complex task. Accordingly, details regarding the mechanism of ion adsorption are still vigorously debated in the literature.

The Saykally and Geissler groups addressed these issues by combining temperature-dependent Deep UV-Second Harmonic Generation (DUV-SHG) experiments and MD simulations to determine the Gibbs free energy of adsorption for a prototypical, chaotropic anion to the air-water interface[23]. They untangled the enthalpic and entropic components to the overall Gibbs free energy and proposed the following mechanism for anion adsorption: (1) *solvent repartitioning* provides the dominant negative enthalpic driving force. As the ion moves from the bulk to the interface, it sheds one or two of its weakly-interacting solvating waters. These waters are then free to form stronger (more favorable) water-water hydrogen bonds as part of the bulk-water network, in comparison to the weak ion-water interactions present in the solvation shell. (2) *Damping of capillary waves* (soft, collective fluctuations in surface topography) from the presence of the ion at the interface reduces entropy and impedes adsorption. This work highlighted the importance of hydration enthalpy as a main driving force for ion adsorption, and helped to explain why strongly-solvated ions, such as F^-, are largely repelled from the interfacial region whereas weakly-solvated ions, such as SCN^- and I^-, show enhanced interfacial concentrations.

An alternative mechanism of adsorption has been proposed by Wang and Das, who studied the adsorption of a monovalent cation to the air-water interface.[27] Qualitatively, they agreed that ion adsorption is an enthalpy-driven process; however, they attributed the negative enthalpy change to a decrease in pressure-volume ($P\Delta V$) work as the ion moves to the surface, and not to solvent repartitioning. They also argued that the presence of the ion at the interface *increases* capillary wave fluctuations, rather than damping them (although they still report a net reduction in entropy, as the capillary wave fluctuations shift to occupy a single mode). Other studies of the air-water interface have examined the importance of hydration structure around the ion and electric field effects[28], as well as charge asymmetry of the liquid water surface.[29]

Studies of *water condensed-hydrophobe* interfaces have also aided our understanding of the forces that drive ion adsorption. Saykally and Geissler extended their study of the air-water interface[23] by applying the same analysis to the graphene-water interface, and determined a very similar Gibb's free energy, but revealing a

qualitatively different mechanism of adsorption.[14] Liquid-liquid interfaces have been studied with nonlinear and X-ray spectroscopies[9,19,30–35] as well as with MD simulation[36–40], and in certain cases it has been shown that the structure/behavior of the air-water and water-liquid hydrophobe interfaces are quite similar[11,36]. Many of these studies have focused on ion transfer and solvent extraction, analyzing the effects that surfactants, anions, and cations have on fundamental properties such as the capillary width and ion pairing.

Based on these previous studies, we pose the question: what drives ion adsorption *to water-liquid hydrophobe interfaces*, and do these interfaces engender different mechanisms of adsorption, as compared to air-water and graphene-water? In this work, we address this question by exploiting the inherently surface-specific techniques of broadband deep-UV electronic sum frequency generation spectroscopy (DUV-ESFG) and resonantly enhanced DUV-SHG to characterize the adsorption of the thiocyanate anion (SCN^-) to two liquid hydrophobe interfaces: toluene-water and decane-water. We find that the interfacial charge transfer to solvent (CTTS) spectra for SCN^- at these interfaces are very nearly identical to that of air-water, and that the Gibbs free energies of adsorption of all three interfaces are equal within error. MD simulations reveal that SCN^- adsorption to the decane-water and toluene-water interfaces is driven by an increase in the entropy of the system as the ion approaches the interface, and that there is minimal enthalpic contribution. Thus, we reveal a strikingly different mechanism of adsorption than has been reported for the air-water and graphene-water interfaces and highlight the importance of accounting for molecular-level details when interpreting experimental data on ion adsorption.

4.2 Materials and Methods:

All glassware and sample dishes used were soaked overnight in AlNochromix (Alconox Inc.) cleaning solution and then rinsed thoroughly with 18.2 MΩ ultra-pure water. NaSCN salt (Alfa Aesar 98% minimum purity) was baked overnight in a 150°C oven to remove organic impurities prior to making salt solutions. Toluene (Thermo Fisher Scientific, HPLC grade, 99.8% minimum purity) was purified with baked silica gel for SHG experiments and used unpurified for SFG experiments. Decane (Thermo Fisher Scientific, HPLC grade, 99.8% minimum purity) was used without purification for both SHG and SFG experiments. The NaSCN-hydrophobe interfaces were

prepared by depositing NaSCN solution into a Petri dish and then depositing a thin layer of liquid hydrocarbon on top of the aqueous solution.

DUV-SHG Experimental Design:

The output of a Ti-S amplified laser system (Spectra Physics Spitfire, 2 mJ, 1kHz, 100fs) centered at 800 nm is directed through an optical parametric amplifier (TOPAS) to generate light at 386 nm for water-toluene SHG measurements, and passed through a BBO crystal to generate light at 400 nm for water-decane SHG measurements. The light is then focused onto the surface of a Petri dish containing the NaSCN solution and hydrocarbon surface layer, with input energies of 1 – 3 μJ per pulse, depending on solution concentration. The reflected SH photons are collected and spectrally filtered from the fundamental light by a Pellin-Broca prism, and detected using a gated integration system (Stanford Research Systems), a monochromator (Acton SpectraPro 2150i) and a photomultiplier (Hamamatsu, R7154PHA) for photon counting. The polarization scheme used was *pp* (*p*-polarized SH, *p*-polarized fundamental). For each SHG measurement of NaSCN at the water-toluene or water-decane interface, a measurement was made for NaSCN at the air-water interface from the same aqueous solution. All measurements of NaSCN at a water-hydrophobe surface were normalized relative to the response of the respective pure water-hydrophobe interface.

DUV-ESFG Experimental Design:

The experimental setup has been described in detail in Chapter 2.[41] Briefly, a Ti-S amplified laser system (Spectra Physics Spitfire, 4mJ, 1kHz, 100 fs) centered at 800 nm is used to generate a broadband white light continuum pulse (WLC) (600-1400 nm), and a narrowband UV pulse at 266 nm (FWHM = 2nm).

In order to access the electronic CTTS transitions of the thiocyanate anion, the narrowband UV and broadband WLC pulses are overlapped temporally and spatially at the water-hydrocarbon surface to generate a deep-UV SF photon in the phase matched direction, enabling ~30 nm of spectral width (~190 – 220 nm) to be observed in a single laser shot. SF photons are collected and sent into a spectrograph (Acton SpectraPro 300i) and CCD (Princeton Instruments PIXIS 2K) for detection. Each raw NaSCN spectrum has a corresponding background spectrum that is generated by separating the two input pulses in time. Spectra of the neat water-

hydrocarbon interface(no added thiocyanate) were also collected with spatial and temporal overlap, for background subtraction and normalization. The polarization scheme used was *ppp* (*p*-polarized SFG, *p*-polarized 266 nm, *p*-polarized WLC). All interfacial spectra of NaSCN are normalized to the non-resonant response from GaAs, which corrects for the low efficiency of optics in the short-wavelength region as well as lower intensities of the WLC on the edges of its spectrum.

Molecular Dynamics Simulations

The liquid/liquid interface is formed by placing a slab of water molecules next to a slab of toluene or decane molecules in a rectangular box and is located in the X-Y plane at $Z \approx 0$. The water phase occupies the region $Z < 0$ and the oil phase is in the $Z > 0$ region. Each liquid phase is at equilibrium with its own vapor phase, so there is only one liquid/liquid interface. Periodic boundary conditions are applied in all directions. A reflecting wall is located 5Å from the simulation box boundaries in the Z-direction to prevent mixing of the two vapor phases. The systems studied include a single SCN^- ion placed in different locations of the water/oil interface.

The potential energy functions used for water are a flexible version of the SPC model. For toluene, a fully atomistic flexible model based on the OPLS all atom description, and for decane, a united atom OPLS model is used.[42] The intermolecular interaction potentials are described as the pairwise sum of Lennard-Jones (LJ) and Coulomb terms. Standard Lorentz-Berthelot combining rules[43] are used to generate LJ parameters for the interactions between atoms located in different molecules. These parameters are given in the Supplemental Information. The intermolecular SCN^- ion potential is taken from the work of Tesei at al.[44] This model was shown to reproduce several experimental data including the air–water surface tension for a wide range of salt concentrations. In addition, we use a harmonic potential with parameters selected to reproduce the IR fundamental frequencies of this ion in solution.[45]

The simulation methodology used to examine the adsorption of ions at the liquid/liquid interface has been described in details elsewhere.[46] Briefly, the SCN^- ion is restricted by an external potential to be in N overlapping lamellas, each 2Å-wide, spanning the region from bulk water to bulk oil. In each lamella, a 5 ns constant temperature (T = 298K) Molecular Dynamics (MD) trajectory is carried out and used

to compute the ion's position probability distribution and several structural and energetic properties of the ion as a function of the distance from the interface. The free energy profile for the adsorption of the ion is determined using the umbrella sampling method[43,46] by combining the local free energy segments calculated from the ion's position probability distribution functions. All the MD simulations are performed with in-house software that uses the velocity Verlet algorithm[43] with an integration time-step of 1 fs.

4.3 Results and Discussion

4.3.1 Broadband Deep UV Electronic Sum-Frequency Generation Spectra

Figure 4.1 shows a schematic diagram of the sample design employed for the nonlinear experiments, following the procedure of Shen et. al. for preparation of liquid-liquid interfaces.[8] An energy level diagram highlights the 2-photon resonant enhancement of the CTTS band.

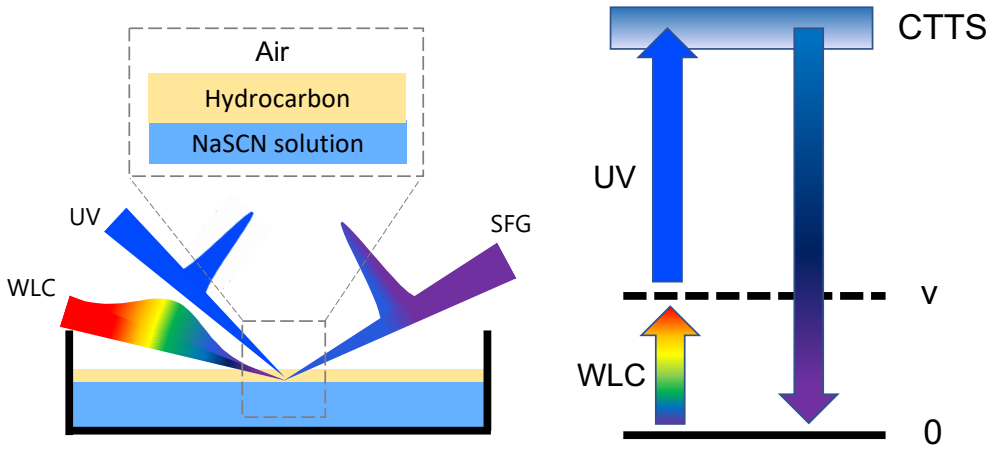

Figure 4.1: Schematic experimental design used for SHG + SFG experiments. The energy level diagram highlights the 2-photon resonance enhancement. 0 = ground state and v = virtual state

A representative unnormalized, background-subtracted DUV-ESFG spectrum of the thiocyanate anion at the interface between 3M NaSCN and a thin layer of decane at 298 K is shown in Figure 4.2a. The spectrum of thiocyanate at a water-toluene interface is identical within the noise of the measurement and is omitted for

redundancy. The spectral window obtained in a single laser shot (ca. l00 fs) can be shifted to cover a range of shorter or longer wavelengths by changing the temporal overlap of the two input pulses, due to the temporal chirp of the white light continuum (WLC). The background is measured by separating the two input pulses in time, thereby not generating any SF photons. Figure 4.2b shows the SFG spectrum of GaAs, which has no resonance at the wavelengths probed here, and is used to normalize the raw spectrum. Weak intensity in the low-wavelength region of the raw spectrum is a result of lower input energies at shorter wavelengths in the WLC, the temporal chirp of the WLC, as well as low efficiencies of the optics and detection system in the DUV. Normalization by non-resonant GaAs corrects for these inefficiencies and reveals the $|\chi^{(2)}|^2$ interfacial power spectrum.

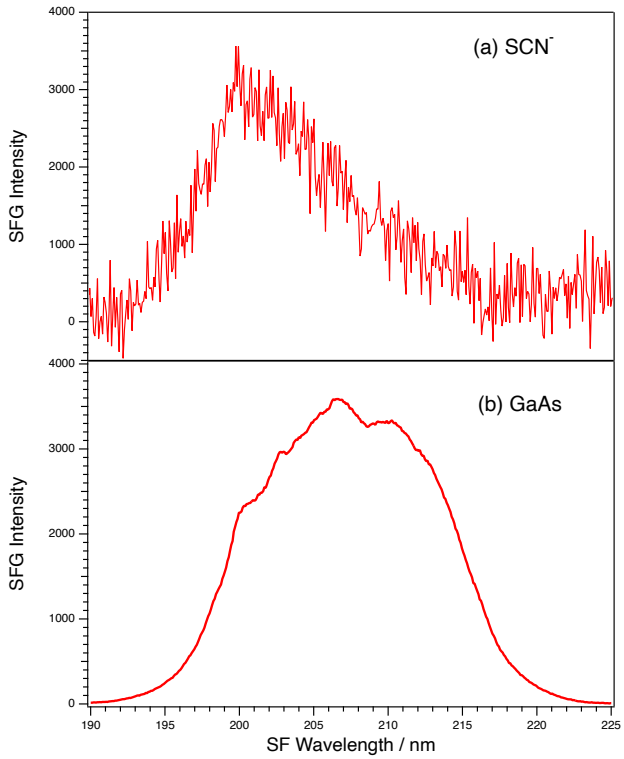

Figure 4.2: SFG spectrum of non-resonant gallium arsenide, used for normalization. (b) Unnormalized ESFG spectrum of 3M NaSCN at the water-decane interface at 298 K.

The bulk absorption spectrum of NaSCN in water, shown in Figure 4.3a in the spectral window of 195-240 nm, comprises two CTTS transitions. Fox et al. measured the far-UV absorption spectrum of tetramethylammonium thiocyanate and assigned a

lower energy transition centered at 216 nm and a higher energy transition centered at 185 nm.[47] The normalized, background-subtracted DUV-ESFG spectra of 3M NaSCN at the air-water(blue), decane-water(red), and toluene-water(black) interfaces are shown in Figure 4.3b.

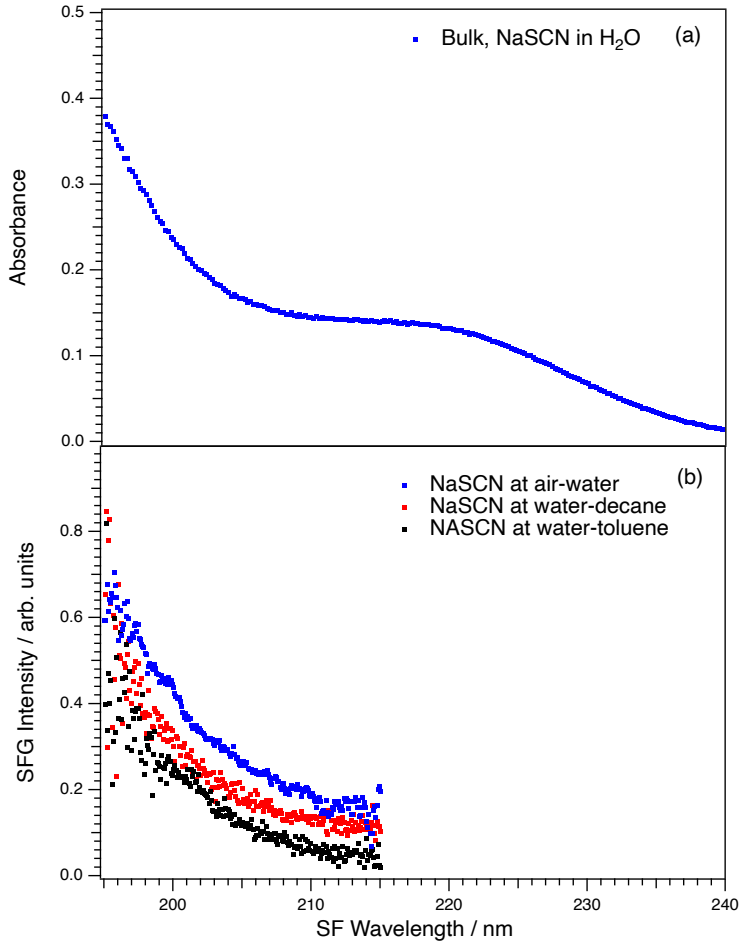

Figure 4.3: Charge transfer to solvent (CTTS) spectra of **(a)** $100\mu M$ NaSCN in bulk water and **(b)** 3M NaSCN at the air-water interface (blue dots), toluene-water interface (black dots), and decane-water interface (red dots). All three spectra in **(b)** overlap completely, but the air-water and decane-water spectra have been offset for convenient viewing. The interfacial CTTS spectra at the air-water and toluene-water interfaces have been published previously by Mizuno et al.[48] and Devlin et al.[15], respectively and are reproduced here with permission from the authors.

In the experiments described here, the $\left|\chi^{(2)}\right|^2$ vs ω_{SFG} interfacial power-spectrum (Figure 4.3b) is collected with only the generated SF photon being resonant with the

CTTS transition (referred to as one-photon off-resonance, two-photon on-resonance). The normalized SFG intensity can be written as:

$$I_{SFG} \propto \left|\chi^{(2)}\right|^2 \propto \sum_n \frac{\left|\mu_{0,n}(\alpha_{0,n})_{TPA}\right|^2}{\left(\omega_{0,n} - \omega_{SFG}\right)^2 - \Gamma_{0,n}^2} \quad (4.1)$$

Here $\chi^{(2)}$ is the second-order susceptibility, $\mu_{0,n}$ is the transition dipole matrix element, $(\alpha_{0,n})_{TPA}$ is the two-photon absorption (TPA) polarizability tensor, $\omega_{0,n}$ is the transition frequency (in this case the CTTS transition), ω_{SFG} is the frequency of the generated SF photon, and $\Gamma_{0,n}$ is the linewidth of the CTTS transition

As is evident by comparison between panels a and b, only the higher energy transition is detectable with DUV-ESFG, the lower energy transition likely being two-photon inactive (an SFG selection rule), according to Equation 4.1. This behavior has been observed for the CTTS transitions of other anions in water.[49] The details of this have been discussed in a previous publication[48] and will not be a focus of the present study.

Other complicating factors could also lead to the absence of the lower-energy CTTS transition in the interfacial spectrum. For example, a reduced dielectric constant in the interfacial region would promote ion pairing, particularly at the molar concentrations used for these experiments, which are required for sufficient S/N. Ion-ion interactions at the interface could shift the ground or excited state energy levels, making the lower energy CTTS band unobservable within our spectral window. Tesei at al. showed via MD simulations that significant ion pairing and cluster formation occur for NaSCN and KSCN salts in bulk solution (>3 mol / kg), but had little effect on their simulated surface properties.[44] Our previous experiments have shown that counter-cations have negligible effects on the spectra and adsorption free energies of ions at interfaces.

The key feature in Figure 4.1b is the lack of any spectral shift of the higher energy transition between these three unique interfaces. CTTS transitions are highly sensitive to local chemical environment and any changes in solvation engendered by the differing interfaces would be expected to shift the higher-energy CTTS transition significantly. Even modest changes in solvent polarity have been shown to shift the bulk CTTS transitions of the iodide anion by 5 nm or more, a change easily measurable within the resolution of our detection system. We expect that the

nonpolar hydrocarbons studied here would shift the transition significantly more than 5 nm. Indeed, Eisenthal has shown with SHG measurements that changes in surface polarity at liquid-liquid interfaces, such as water-chlorobenzene and water-heptane, can shift charge transfer transitions of polarity indicator molecules by as much as 40 nm, when compared to the air-water interface.[17] The lack of a spectral shift observed here implies that the solvation environments around SCN^- at the air-water, toluene-water, and decane-water interfaces are strikingly similar, and that the presence of the condensed oil phase induces very little perturbation. We support this finding through MD simulations by computing the interaction free energy of SCN^- with the water and oil molecules (Figure 4.7), and show that it is remarkably similar for both the water-decane and water-toluene systems. More details on this are included in the Molecular Dynamics Simulation section

Similar behavior for anions has been observed via other spectroscopic signatures. For example, it has been shown that the iodide and thiocyanate anions exhibit insignificant changes in vertical ionization energies (VIE) in bulk water vs. at the air-water interface, owing to the fact that these anions are asymmetrically solvated in bulk, which engenders similar solvation energetics as the geometrically constrained, asymmetric solvation environment at the interface.[50]

4.3.2 DUV-SHG and the Langmuir Adsorption Model

The use of a Langmuir adsorption model to fit spectroscopic data is well established[2,51,52], and this methodology is adopted here for extracting the Gibbs free energy of adsorption from experimental SHG intensities. A thorough derivation of this model and its application to SHG is given in Chapter 2. Here, we briefly expand that derivation to include a third term in the SH intensity, due to the hydrocarbon. The measured SH intensities ($I_{2\omega}$) are related to the Gibbs free energy through the bulk anion concentration, according to the following:

$$I_{2\omega} = \left|\chi^{(2)}_{water} + \chi^{(2)}_{hydrocarbon} + \chi^{(2)}_{SCN^-}\right|^2 I^2_{\omega} \quad (4.2)$$

Here, $\chi^{(2)}_i$is the second-order susceptibility of each species and I^2_{ω} is the fundamental intensity. $\chi^{(2)}$ is dependent on the number density, N_i, as well as the effective hyperpolarizability, β^{eff}

$$\frac{I_{SH}}{I_{\omega}^2} \propto \left|N_{water} * \beta_{water}^{eff} + N_{hydrocarbon} * \beta_{hydrocarbon}^{eff} + N_{SCN^-} * \beta_{SCN^-}^{eff}\right|^2 \quad (4.3)$$

Water and the hydrocarbons employed here did not give strong SH responses, and we assume their contributions to the signal are real. However, thiocyanate has a strong CTTS transition at the SH wavelength, and therefore has both a real and imaginary component. We can group these contributions accordingly

$$\frac{I_{SH}}{I_{\omega}^2} \propto \left(N_{water} * \beta_{water}^{eff} + N_{hydrocarbon} * \beta_{hydrocarbon}^{eff} + N_{SCN^-} * Re\{\beta_{SCN^-}^{eff}\right)^2 + \left(N_{SCN^-} * Im\{\beta_{SCN^-}^{eff}\}\right)^2 \quad (4.4)$$

and switch to using concentrations by dividing each term by N_{water}, since N_{SCN^-} / N_{water} is a concentration:

$$\frac{I_{SH}}{I_{\omega}^2} \propto \left(\beta_{water}^{eff} + \frac{N_{hydrocarbon}}{N_{water}} * \beta_{hydrocarbon}^{eff} + \frac{N_{SCN^-}}{N_{water}} * Re\{\beta_{SCN^-}^{eff}\}\right)^2 + \left(\frac{N_{SCN^-}}{N_{water}} * Im\{\beta_{SCN^-}^{eff}\}\right)^2 \quad (4.5)$$

We simplify the expression to:

$$\frac{I_{SH}}{I_{\omega}^2} \propto (A + N_s * B)^2 + (N_s * C)^2 \quad (4.6)$$

Here, the system response from water and the hydrocarbon have been grouped together in the non-resonant term, A. B is the real component of the thiocyanate susceptibility, C is the imaginary component of the thiocyanate susceptibility, and N_s is the concentration of surface-active thiocyanate anions.

In the case of decane, grouping the signal response into the non-resonant term is valid, as it has no resonances at the fundamental or SH wavelengths. Toluene, however, absorbs at 200 nm, the SH wavelength. Grouping its response into the non-resonant term is therefore not explicitly correct. However, because the surface concentration of toluene is constant in all experiments, the response from toluene is normalized from the response of the pure water-toluene interface, and therefore assuming its contributions to be real becomes a valid approximation.

We use a kinetic description to determine the concentration of surface-active species, which is derived in Chapter 2. Substituting for N_s in equation 4.6 leads to the following:

$$\frac{I_{2\omega}}{I_{\omega}^2} = \left|\chi^{(2)}\right|^2 \propto \left(A + B\frac{X_{SCN^-}}{(1-X_{SCN^-})e^{\frac{\Delta G}{RT}} + X_{SCN^-}}\right)^2 + \left(C\frac{X_{SCN^-}}{(1-X_{SCN^-})e^{\frac{\Delta G}{RT}} + X_{SCN^-}}\right)^2 \quad (4.7)$$

Here, X_{SCN^-} is the bulk concentration of SCN^-, and ΔG is the Gibb's free energy of adsorption.

It is important to consider the assumptions inherent in this Langmuir model and when they may break down in the systems studied here. First, the model assumes that only one adsorbate can bind to a specific surface "site", i.e. it describes monolayer coverage. In the low concentration limit, the formation of an electric double layer would affect the energetics of adsorption and should be considered. At higher concentrations, as appreciable anion population moves to the surface, the region of broken inversion symmetry (i.e. the interface) extends deeper into the bulk phase, and contributions from "sub-surface" ions will become SHG active. Second, the model assumes that all interfacial "sites" are treated equally, i.e. no interaction between adsorbing molecules are accounted for. Again, we expect this assumption to break down with increasing concentration; for example the Debye Length of a 1:1 electrolyte is ~1 nm for a 0.1M solution, however it quickly decays and asymptotes around 0.2 nm for concentrations above 1 M. In these regimes, close-range interactions between ions should be important.[53] To that end, Garde et al have shown with simulation that water-mediated attraction between oppositely charged ions at the air-water interface is drastically enhanced compared to in bulk water.[54] Despite these shortcomings, the Langmuir isotherm adequately models our experimental data and agrees with theoretical calculations, and we continue with its use instead of adopting a more complicated model.

Figure 4.4 shows the normalized DUV-SHG intensities for SCN^- at the air-water, toluene-water, and decane-water interfaces plotted against bulk NaSCN concentration ranging from 0 to 2.5 M. The SCN^- CTTS transition has an extinction coefficient in the Deep UV of ~10^4 M^{-1} cm^{-1}, which provides strong resonance enhancement for these inherently weak second-order signals. The air-water and toluene-water data in Figure 4.4a were collected at a second harmonic wavelength of

193 nm, resulting in Gibbs free energies of adsorption of -7.5 ± 0.7 kJ/mol and -7.3 ± 0.7 kJ/mol, respectively. The air-water and decane-water data in Figure 4.4b were collected at a second harmonic wavelength of 200 nm, yielding Gibbs free energies of adsorption of -6.9 ± 0.8 kJ/mol and -6.7 ± 0.9 kJ/mol respectively, with the uncertainties being one standard deviation in the fit. All SHG intensities are normalized to the respective neat-water-hydrophobe interface, i.e. SHG = 1 for decane-water and toluene-water with no added salt.

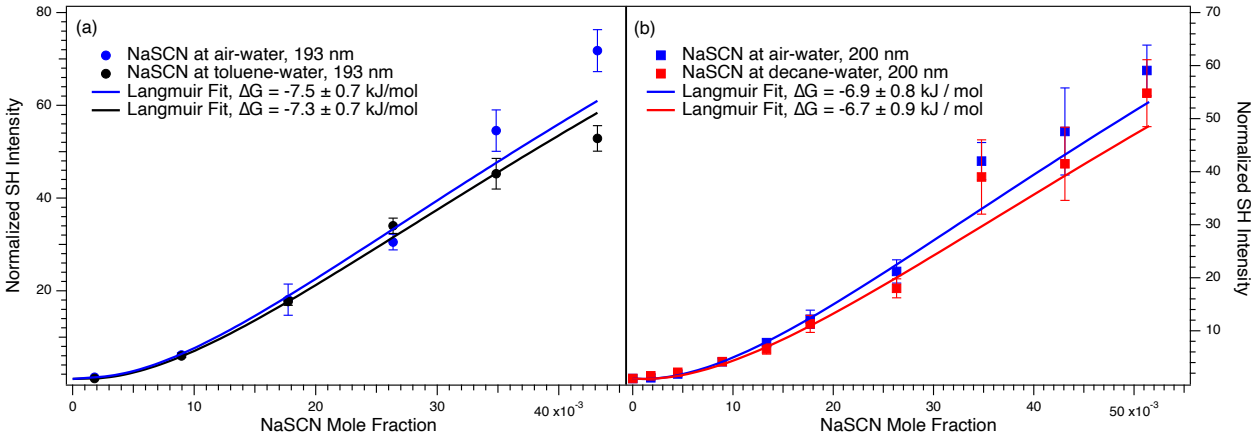

Figure 4.4: Normalized second harmonic generation (SHG) intensities versus bulk anion concentration. **(a)** Data for NaSCN at the air-water(blue circles) and toluene-water(black circles) interfaces collected at a SHG wavelength of 193 nm. **(b)** data for NaSCN at the air-water(blue squares) and decane-water(red squares) interfaces collected at a SHG wavelength of 200 nm. The lines represent the Langmuir adsorption fit to each respective data set, with the uncertainty being one standard deviation. The data in (a) have been published previously by Devlin et al. and are reproduced here with permission from the authors. [15]

The SHG intensity contains contributions from each component in the system; water, oil, and SCN^- (Equation 4.2). In the low concentration regime, the intensity increase with bulk anion concentration can be attributed to alignment of water molecules in the interfacial region, due to the static electric field from the ions.[55] At higher concentrations, resonant enhancement from the anion begins to dominate as an electric double layer forms and appreciable SCN^- is present in the SHG probing depth. The exact probing depth is difficult to quantify experimentally, however SHG is generated over the entire region with broken inversion symmetry, corresponding to roughly 1 nm for pure water and slightly deeper for electrolyte solutions.[56]

The Gibb's free energy of adsorption for SCN^- to the air-water, toluene-water, and decane-water interfaces all agree within experimental error, and are in good agreement with the free energy profiles calculated in Figure 4.6. This behavior is consistent with previous measurements of anions at hydrophobic surfaces by the Saykally and Geissler groups, wherein the reported Gibb's free energies were all within error of that for air-water.[14,19,20]

4.3.3 Molecular Dynamics Simulations – Density and Free Energy Profiles

The length scale of the ion's free energy change is determined, in part, by the density profiles of the water and oil phases. The density profiles of neat water next to neat toluene and next to neat decane are shown in Figure 4.5.

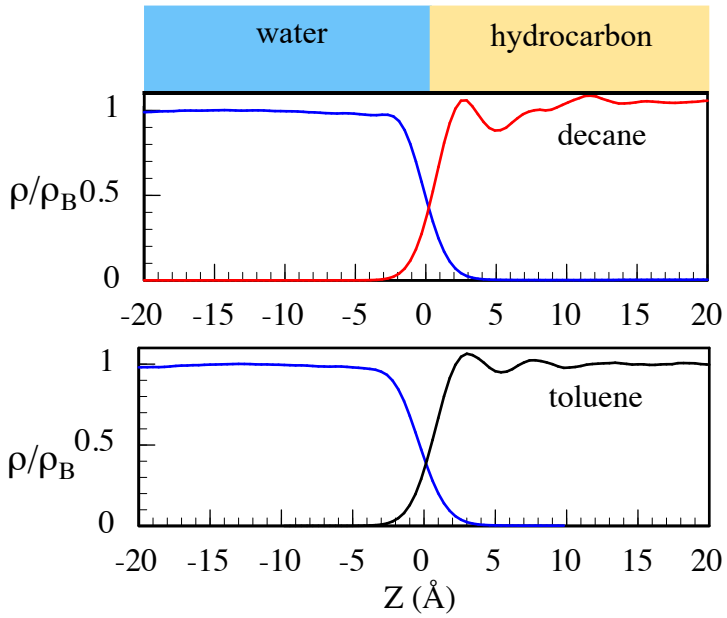

Figure 4.5: Density profiles (relative to the respective bulk values) of water (blue) and oil (red = decane, black = toluene) at T = 298K. $Z = 0$ is the location of the Gibbs dividing surface.

$Z = 0$ is the location of the Gibbs Dividing Surface (GDS), which is the plane parallel to the interface where the water density is approximately 50% of the bulk value. For an exact definition of the GDS, see Rowlinson et al.[57] The so called 90/10 interface region is defined as the distance over which the density of water declines from 90% to 10% of its bulk value, and is quite narrow, about 4-5 Å.

The free energy profiles as the ion approaches the interface are shown in Figure 4.6. The profile exhibits a small local minimum near the GDS that corresponds to a free energy of adsorption (relative to bulk water) of about -5.9 kJ/mol for both liquids, in reasonable agreement with the experimental values given above. As the ion crosses the interface, the free energy increases monotonically and rapidly (and will eventually reach a plateau significantly deep into the organic phase). The problem of ion transfer into the organic phases and the co-transfer of water molecules with the ion is outside the scope of this paper and will be described elsewhere. However, note that the more rapid rise in the free energy profile for decane, which signals a larger free energy of transfer of SCN^- across the water/decane interface than across the water/toluene interface is consistent with the higher dielectric constant of toluene (2.4 compared with 2.0).

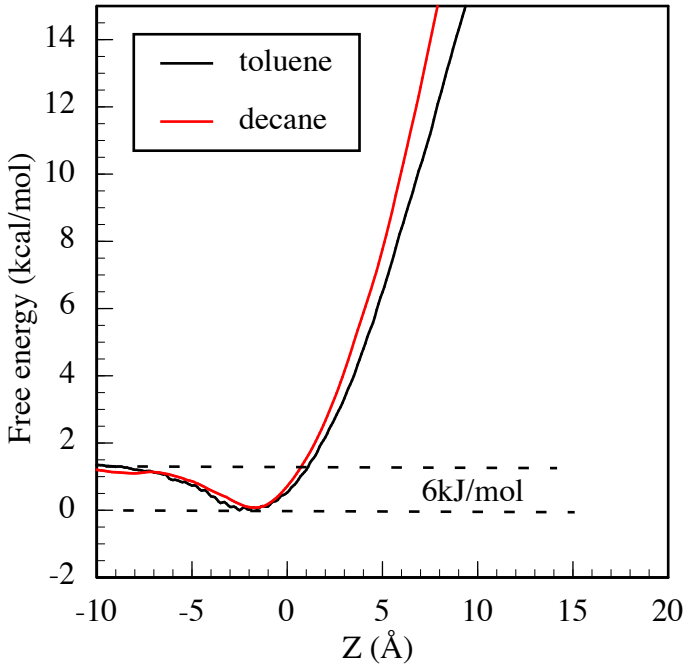

Figure 4.6: The free energy profiles for moving the SCN^- ion across the water-toluene and water-decane interface at 298K. Water-toluene data have been previously published and are reproduced here.[58]

To gain insight into the nature of the identical local free energy minima observed for the two interfaces, we show in Figure 4.7 the total interaction energy of the ion and the oil molecules.

The lack of local minima in both cases suggests that the adsorption free energy is due to entropic contributions alone. This is markedly different from the results obtained for both the air/water and graphene-water interfaces. As the ion approaches the liquid/liquid interface, the existence of significant water structural fluctuations related to the ability of the ion to keep its hydration shell[46] results in an increase in disorder and thus significant entropic contribution to the free energy of adsorption. As the ion moves deeper into the organic phase, the significant loss in the energy of water hydration reduces the enthalpic contribution and causes the eventual increase in free energy. The increase in (negative) ion-oil interactions makes some enthalpic contributions, but not enough to offset the loss in the water hydration energy.

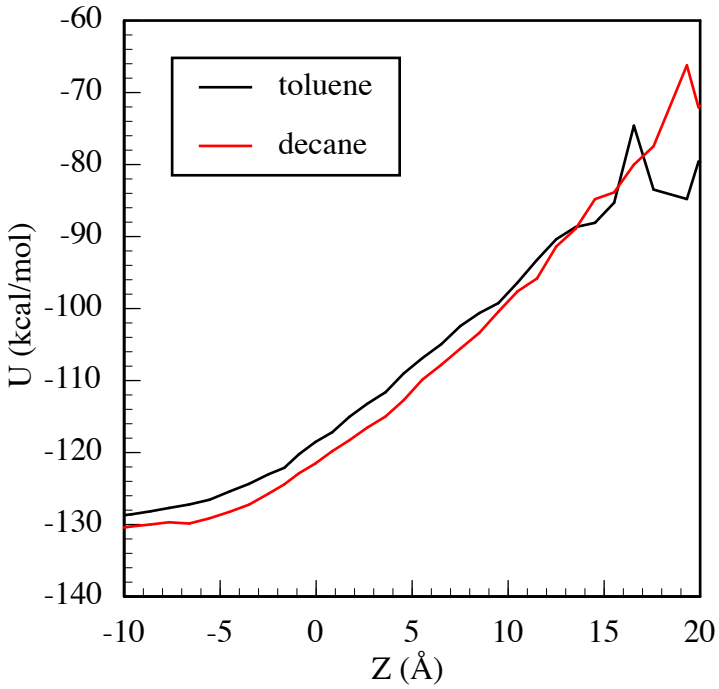

Figure 4.7: The total interaction energy of the SCN^- ion with the water and the oil molecules for decane and toluene. Water-toluene data have been previously published and are reproduced here.[58]

The free energy profiles shown in Figure 4.6 and the change in energy of adsorption depicted in Figure 4.7 suggest that the adsorption of the anion to the liquid/liquid interface is entropically driven. This can be understood as an increase in the water capillary fluctuations in the form of water "fingers" as the ion drags some of the hydration shell water molecules as it crosses the Gibbs dividing surface. This phenomenon has been extensively documented for monoatomic ion transfer across the liquid/liquid interface.[59–63] and is demonstrated in Figure 4.8.

The formation of water "fingers" and the associated increase in entropy are rationalized in terms of the increase in water density fluctuations. The ion can be stabilized at the interface by a nearly complete hydration shell. The water molecules in the hydration shell are free to rapidly exchange with other nearby water molecules.[64] Only when the ion is further pushed into the oil phase does this process become less likely, and the free energy accordingly rises rapidly.

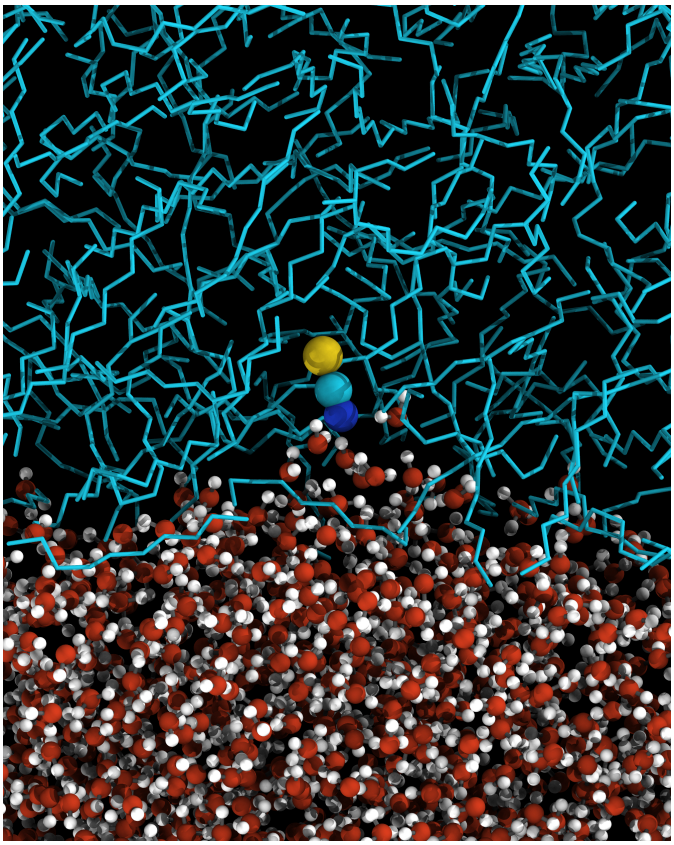

Figure 4.8: A snapshot of the SCN^- ion (blue = N, green = C, yellow = S, image enlarged) adsorbed at the water-decane interface.

4.3.4 *Discussion of Interfacial Gas Enrichment at Hydrophobic Surfaces*

The strikingly similar behavior observed here for anions at the air-water, toluene-water, and decane-water interface, in the context of additional studies of hydrophobic surfaces, seem to imply a universal nature of liquid hydrophobe-water interactions. It is indeed interesting that while the macroscopic measurables, such as the Gibbs free energy and interfacial spectra are the same, the microscopic details, such as the

mechanism of adsorption (viz. entropy and enthalpy considerations) are very different, yet always offset in equal magnitudes. We include here a brief discussion of other studies of water-hydrophobe interfaces and in particular focus on an interesting phenomenon that could indeed influence measurements such as those reported in this chapter and at other hydrophobic surfaces.

Willard and Chandler used MD simulations to study the density profiles and height fluctuations of water next to solid hydrophobic/hydrophilic substrates, and reported that a hydrophobe-water interface has very similar properties to the air-water interface, whereas a hydrophile-water interface does not.[65] Similar findings have been reported for alkane-water interfaces.[66] The study of ions at hydrophobe-water interfaces by SHG agrees with this analysis. Table 4.1 reports the Gibbs free energy of adsorption for thiocyanate and bromide anions at various water-hydrophobe interfaces measured by SHG spectroscopy. In all cases, the results obtained for the adsorption free energy agree within error with those for the air-water interface.

Table 4.1: Anion affinities for air-water and hydrophobe-water interfaces determined by DUV-SHG spectroscopy.

Ion / Interface	ΔG_{ads} (kJ/mol)	Ref.
Br^- / air-water	~ -1.4	19
Br^- / dodecanol-water	~ -2	19
SCN^- / air-water	-7.5 ± 0.1	67
SCN^- / dodecanol-water	-6.7 ± 1.1	20
SCN^- / graphene-water	-8.5 ± 1.1	14
SCN^- / toluene-water	-7.3 ± 0.7	68
SCN^- / decane-water	-6.7 ± 0.9	68

A relevant phenomenon to the study of hydrophobic surfaces is interfacial gas enrichment (IGE). In 2018, Schlesinger and Sivan showed with high resolution AFM that aqueous solutions in contact with a solid hydrophobic surface (graphite) exhibit a 2-5 nm layer of condensed gas, composed mainly of nitrogen, sandwiched between the two media.[69] This behavior has been observed for various dissolved gases[70] and been verified with different experimental techniques.[71,72] While this phenomenon has not yet been reported at liquid-liquid interfaces to the best of our knowledge, it is not unreasonable to assume that surface sensitive spectroscopies, such as we employ in this

study and in our previous study of the graphene-water interface, may be influenced by a water-condensed gas interface if the aqueous solution is not properly degassed. To test this, we measured interfacial spectra of NaSCN at the water-decane interface, wherein the NaSCN solutions had been bubbled with nitrogen gas for 30 minutes prior to measurements being taken (Figures 4.9c and 4.9d).

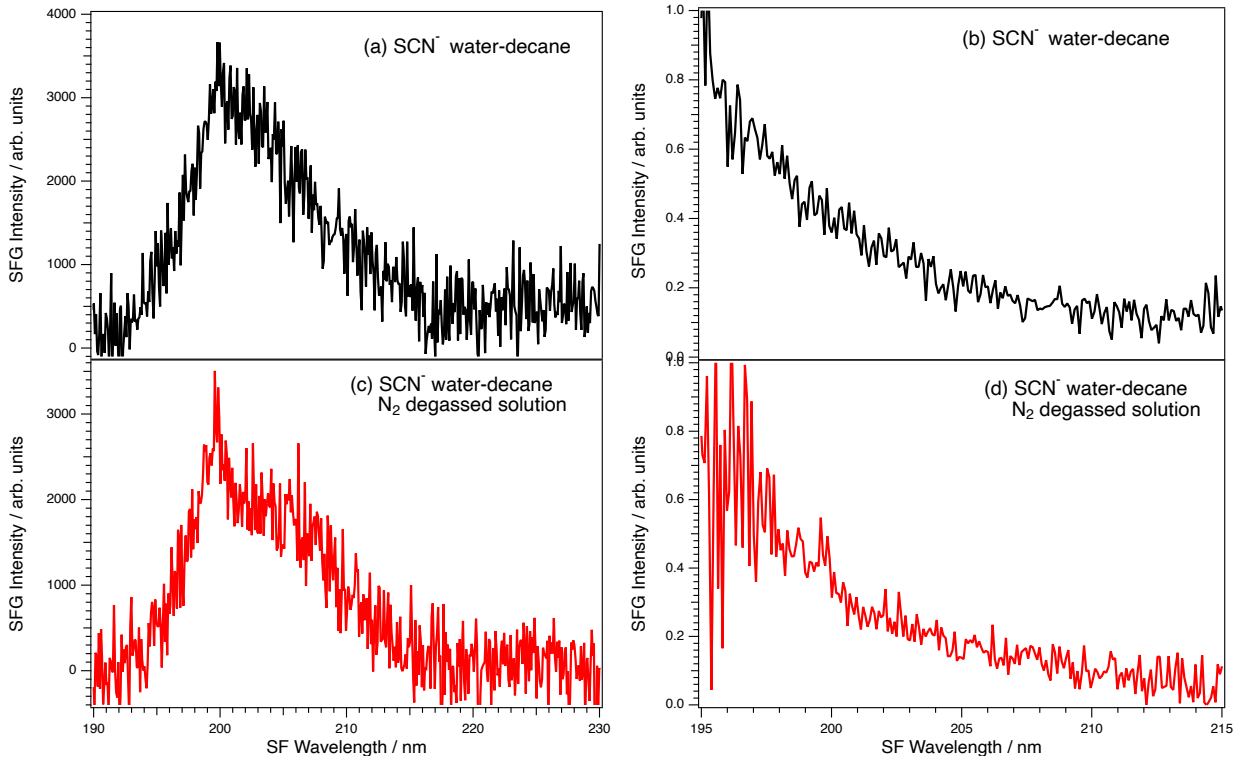

Figure 4.9: Interfacial electronic sum-frequency spectra of the thiocyanate anion at the water-decane interface. (a) and (b) show the unnormalized and normalized spectra, respectively, for thiocyanate prepared under normal conditions, while (c) and (d) show the corresponding unnormalized and normalized spectra, respectively, for thiocyanate solutions that were bubbled with N_2 gas for 30 minutes prior to the measurement.

Normal sample preparation uses ultrapure Millipore water, for which the dissolved gas concentration is expected to be minimal. To test the hypothesis that dissolved gas might influence the spectral results obtained here, we attempted to artificially develop an interfacial gas layer by saturating the solution with nitrogen. As is evident in Figure 4.9, the results of the solution with and without nitrogen gas purging are

identical within the noise of the measurement. No further testing for IGE was undertaken, however future work might test saturating the solution with different gases, such as hydrogen or oxygen. Or, alternatively, proper degassing of the solution could be undertaken, using techniques such as the freeze-thaw method. In particular, the work published by Sivan was conducted at a water-solid interface, and in light of this, it might be worthwhile to revisit our study of ion adsorption to the graphene-water interface.

While it is still unknown if IGE occurs at liquid-liquid interfaces, that this layer of condensed gas, which is 300 times denser than air,[69] might mimic the results of the air-water interface is interesting on its own account. Such dense gas layers could have profound general effects in water-hydrophobe interfaces, including those in biology.

4.4 Conclusions

The ubiquity of water-hydrophobe interactions in chemistry and biology necessitates that we develop a detailed understanding of these interfaces. In this work, we characterized the adsorption behavior of the thiocyanate anion to two water-liquid hydrophobe interfaces, water-toluene and water-decane through resonantly enhanced nonlinear spectroscopy techniques. We report that the Gibbs free energy of adsorption and the interfacial CTTS spectra are in good agreement with these same measurements for thiocyanate at the air-water and graphene-water interfaces. However, the details regarding the mechanism of ion adsorption are strikingly different. Specifically, we report that for the water-toluene and water-decane interfaces, ion adsorption is driven by an increase in entropy due to the formation of water "fingers" as the ion moves into the condensed organic phase, with very little enthalpic contribution.

Many studies have reported on the seemingly general behavior of water-hydrophobe interfaces.[20,36,66,69,70] This work, along with others[14,23], highlights the importance of accounting for specific, molecular-level details when studying ion adsorption to hydrophobic interfaces. This not only has profound impacts on our fundamental understanding of water-hydrophobe interactions, but also on how we apply this understanding to problems in chemistry, biology, atmospheric science, and other areas.

References

(1) Jungwirth, P.; Tobias, D. J. Ions at the Air/Water Interface. *The Journal of Physical Chemistry B*. ACS Publications 2002, pp 6361–6373.
(2) Petersen, P. B.; Saykally, R. J. Confirmation of Enhanced Anion Concentration at the Liquid Water Surface. *Chem. Phys. Lett.* **2004**, *397* (1–3), 51–55.
(3) Knipping, E. M.; Lakin, M. J.; Foster, K. L.; Jungwirth, P.; Tobias, D. J.; Gerber, R. B.; Dabdub, D.; Finlayson-Pitts, B. J. Experiments and Simulations of Ion-Enhanced Interfacial Chemistry on Aqueous NaCl Aerosols. *Science* **2000**, *288* (5464), 301–306.
(4) Hu, J. H.; Shi, Q.; Davidovits, P.; Worsnop, D. R.; Zahniser, M. S.; Kolb, C. E. Reactive Uptake of Cl2 (g) and Br2 (g) by Aqueous Surfaces as a Function of Br- and I-Ion Concentration: The Effect of Chemical Reaction at the Interface. *J. Phys. Chem.* **1995**, *99* (21), 8768–8776.
(5) Wellen, B. A.; Lach, E. A.; Allen, H. C. Surface p K a of Octanoic, Nonanoic, and Decanoic Fatty Acids at the Air--Water Interface: Applications to Atmospheric Aerosol Chemistry. *Phys. Chem. Chem. Phys.* **2017**, *19* (39), 26551–26558.
(6) Jubb, A. M.; Hua, W.; Allen, H. C. Organization of Water and Atmospherically Relevant Ions and Solutes: Vibrational Sum Frequency Spectroscopy at the Vapor/Liquid and Liquid/Solid Interfaces. *Acc. Chem. Res.* **2012**, *45* (1), 110–119.
(7) Tarbuck, T. L.; Richmond, G. L. Adsorption and Reaction of CO2 and SO2 at a Water Surface. *J. Am. Chem. Soc.* **2006**, *128* (10), 3256–3267.
(8) Du, Q.; Freysz, E.; Shen, Y. R. Surface Vibrational Spectroscopic Studies of Hydrogen Bonding and Hydrophobicity. *Science* **1994**, *264* (5160), 826–828.
(9) Miranda, P. B.; Shen, Y. R. Liquid Interfaces: A Study by Sum-Frequency Vibrational Spectroscopy. *J. Phys. Chem. B* **1999**, *103* (17), 3292–3307.
(10) Ma, G.; Chen, X.; Allen, H. C. Dangling OD Confined in a Langmuir Monolayer. *J. Am. Chem. Soc.* **2007**, *129* (45), 14053–14057.
(11) Scatena, L. F.; Brown, M. G.; Richmond, G. L. Water at Hydrophobic Surfaces: Weak Hydrogen Bonding and Strong Orientation Effects. *Science* **2001**, *292* (5518), 908–912.
(12) Pullanchery, S.; Kulik, S.; Roke, S. Water Structure at the Hydrophobic Nanodroplet Surface Revealed by Vibrational Sum Frequency Scattering Using Isotopic Dilution. *J. Phys. Chem. B* **2022**.

(13) Vácha, R.; Rick, S. W.; Jungwirth, P.; de Beer, A. G. F.; de Aguiar, H. B.; Samson, J.-S.; Roke, S. The Orientation and Charge of Water at the Hydrophobic Oil Droplet--Water Interface. *J. Am. Chem. Soc.* **2011**, *133* (26), 10204–10210.

(14) McCaffrey, D. L.; Nguyen, S. C.; Cox, S. J.; Weller, H.; Alivisatos, A. P.; Geissler, P. L.; Saykally, R. J. Mechanism of Ion Adsorption to Aqueous Interfaces: Graphene/Water vs. Air/Water. *Proc. Natl. Acad. Sci.* **2017**, *114* (51), 13369–13373.

(15) Devlin, S. W.; McCaffrey, D. L.; Saykally, R. J. Characterizing Anion Adsorption to Aqueous Interfaces: Toluene--Water versus Air--Water. *J. Phys. Chem. Lett.* **2021**, *13*, 222–228.

(16) Wang, H.; Borguet, E.; Eisenthal, K. B. Generalized Interface Polarity Scale Based on Second Harmonic Spectroscopy. *J. Phys. Chem. B* **1998**, *102* (25), 4927–4932.

(17) Wang, H.; Borguet, E.; Eisenthal, K. B. Polarity of Liquid Interfaces by Second Harmonic Generation Spectroscopy. *J. Phys. Chem. A* **1997**, *101* (4), 713–718.

(18) Eisenthal, K. B. Liquid Interfaces Probed by Second-Harmonic and Sum-Frequency Spectroscopy. *Chem. Rev.* **1996**, *96* (4), 1343–1360.

(19) Onorato, R. M.; Otten, D. E.; Saykally, R. J. Measurement of Bromide Ion Affinities for the Air/Water and Dodecanol/Water Interfaces at Molar Concentrations by UV Second Harmonic Generation Spectroscopy. *J. Phys. Chem. C* **2010**, *114* (32), 13746–13751.

(20) Onorato, R. M.; Otten, D. E.; Saykally, R. J. Adsorption of Thiocyanate Ions to the Dodecanol/Water Interface Characterized by UV Second Harmonic Generation. *Proc. Natl. Acad. Sci.* **2009**, *106* (36), 15176–15180.

(21) Jungwirth, P.; Tobias, D. J. Specific Ion Effects at the Air/Water Interface. *Chem. Rev.* **2006**, *106* (4), 1259–1281.

(22) Stuart, S. J.; Berne, B. J. Effects of Polarizability on the Hydration of the Chloride Ion. *J. Phys. Chem.* **1996**, *100* (29), 11934–11943.

(23) Otten, D. E.; Shaffer, P. R.; Geissler, P. L.; Saykally, R. J. Elucidating the Mechanism of Selective Ion Adsorption to the Liquid Water Surface. *Proc. Natl. Acad. Sci.* **2012**, *109* (3), 701–705.

(24) Noah-Vanhoucke, J.; Geissler, P. L. On the Fluctuations That Drive Small Ions toward, and Away from, Interfaces between Polar Liquids and Their Vapors. *Proc. Natl. Acad. Sci.* **2009**, *106* (36), 15125–15130.

(25) Chang, T.-M.; Dang, L. X. Recent Advances in Molecular Simulations of Ion Solvation at Liquid Interfaces. *Chem. Rev.* **2006**, *106* (4), 1305–1322.
(26) Levin, Y.; dos Santos, A. P. Ions at Hydrophobic Interfaces. *J. Phys. Condens. Matter* **2014**, *26* (20), 203101.
(27) Wang, Y.; Sinha, S.; Desai, P. R.; Jing, H.; Das, S. Ion at Air--Water Interface Enhances Capillary Wave Fluctuations: Energetics of Ion Adsorption. *J. Am. Chem. Soc.* **2018**, *140* (40), 12853–12861.
(28) Sun, L.; Li, X.; Tu, Y.; Ågren, H. Origin of Ion Selectivity at the Air/Water Interface. *Phys. Chem. Chem. Phys.* **2015**, *17* (6), 4311–4318.
(29) Cox, S. J.; Thorpe, D. G.; Shaffer, P. R.; Geissler, P. L. Assessing Long-Range Contributions to the Charge Asymmetry of Ion Adsorption at the Air--Water Interface. *Chem. Sci.* **2020**, *11* (43), 11791–11800.
(30) McFearin, C. L.; Beaman, D. K.; Moore, F. G.; Richmond, G. L. From Franklin to Today: Toward a Molecular Level Understanding of Bonding and Adsorption at the Oil- Water Interface. *J. Phys. Chem. C* **2009**, *113* (4), 1171–1188.
(31) Lin, L.; Chowdhury, A. U.; Ma, Y.-Z.; Sacci, R. L.; Katsaras, J.; Hong, K.; Collier, C. P.; Carrillo, J.-M. Y.; Doughty, B. Ion Pairing Mediates Molecular Organization Across Liquid/Liquid Interfaces. *ACS Appl. Mater. Interfaces* **2021**, *13* (28), 33734–33743.
(32) Lin, L.; Chowdhury, A. U.; Ma, Y.-Z.; Sacci, R. L.; Katsaras, J.; Hong, K.; Collier, C. P.; Carrillo, J.-M. Y.; Doughty, B. Ion Pairing and Molecular Orientation at Liquid/Liquid Interfaces: Self-Assembly and Function. *J. Phys. Chem. B* **2022**, *126* (11), 2316–2323.
(33) Mitrinović, D. M.; Tikhonov, A. M.; Li, M.; Huang, Z.; Schlossman, M. L. Noncapillary-Wave Structure at the Water-Alkane Interface. *Phys. Rev. Lett.* **2000**, *85* (3), 582.
(34) Mitrinovic, D. M.; Zhang, Z.; Williams, S. M.; Huang, Z.; Schlossman, M. L. X-Ray Reflectivity Study of the Water- Hexane Interface. *J. Phys. Chem. B* **1999**, *103* (11), 1779–1782.
(35) Luo, G.; Malkova, S.; Yoon, J.; Schultz, D. G.; Lin, B.; Meron, M.; Benjamin, I.; Vanysek, P.; Schlossman, M. L. Ion Distributions near a Liquid-Liquid Interface. *Science* **2006**, *311* (5758), 216–218.

(36) Willard, A. P.; Chandler, D. The Molecular Structure of the Interface between Water and a Hydrophobic Substrate Is Liquid-Vapor Like. *J. Chem. Phys.* **2014**, *141* (18), 18C519.
(37) Karnes, J. J.; Villavicencio, N.; Benjamin, I. Transfer of an Erbium Ion across the Water/Dodecane Interface: Structure and Thermodynamics via Molecular Dynamics Simulations. *Chem. Phys. Lett.* **2019**, *737*, 136825.
(38) Servis, M. J.; Clark, A. E. Surfactant-Enhanced Heterogeneity of the Aqueous Interface Drives Water Extraction into Organic Solvents. *Phys. Chem. Chem. Phys.* **2019**, *21* (6), 2866–2874.
(39) Kumar, N.; Servis, M. J.; Liu, Z.; Clark, A. E. Competitive Interactions at Electrolyte/Octanol Interfaces: A Molecular Perspective. *J. Phys. Chem. C* **2020**, *124* (20), 10924–10934.
(40) Ghadar, Y.; Christensen, S. L.; Clark, A. E. Influence of Aqueous Ionic Strength upon Liquid: Liquid Interfacial Structure and Microsolvation. *Fluid Phase Equilibria* **2016**, *407*, 126–134.
(41) Rizzuto, A. M.; Irgen-Gioro, S.; Eftekhari-Bafrooei, A.; Saykally, R. J. Broadband Deep UV Spectra of Interfacial Aqueous Iodide. *J. Phys. Chem. Lett.* **2016**, *7* (19), 3882–3885.
(42) Damm, W.; Frontera, A.; Tirado--Rives, J.; Jorgensen, W. L. OPLS All-Atom Force Field for Carbohydrates. *J. Comput. Chem.* **1997**, *18* (16), 1955–1970.
(43) Tildesley, D. J.; Allen, M. P. Computer Simulation of Liquids. Clarendon. Oxford 1987.
(44) Tesei, G.; Aspelin, V.; Lund, M. Specific Cation Effects on SCN--in Bulk Solution and at the Air--Water Interface. *J. Phys. Chem. B* **2018**, *122* (19), 5094–5105.
(45) Jones, L. H. Infrared Spectrum and Structure of the Thiocyanate Ion. *J. Chem. Phys.* **1956**, *25* (5), 1069–1072.
(46) Benjamin, I. Reaction Dynamics at Liquid Interfaces. *Annu. Rev. Phys. Chem.* **2015**, *66* (1), 165–188.
(47) Fox, M. F.; Smith, C. B.; Hayon, E. Far-Ultraviolet Solution Spectroscopy of Thiocyanate. *J. Chem. Soc. Faraday Trans. 1 Phys. Chem. Condens. Phases* **1981**, *77* (7), 1497–1502.
(48) Mizuno, H.; Rizzuto, A. M.; Saykally, R. J. Charge-Transfer-to-Solvent Spectrum of Thiocyanate at the Air/Water Interface Measured by Broadband Deep

Ultraviolet Electronic Sum Frequency Generation Spectroscopy. *J. Phys. Chem. Lett.* **2018**. https://doi.org/10.1021/acs.jpclett.8b01966.

(49) Bhattacharyya, D.; Mizuno, H.; Rizzuto, A. M.; Zhang, Y.; Saykally, R. J.; Bradforth, S. E. New Insights into the Charge-Transfer-to-Solvent Spectrum of Aqueous Iodide: Surface versus Bulk. *J. Phys. Chem. Lett.* **2020**, *11* (5), 1656–1661.

(50) Paul, S.; Herbert, J. Probing Interfacial Effects on Ionization Energies: The Surprising Banality of Anion-Water Hydrogen Bonding at the Air/Water Interface. **2021**.

(51) Okur, H. I.; Chen, Y.; Wilkins, D. M.; Roke, S. The Jones-Ray Effect Reinterpreted: Surface Tension Minima of Low Ionic Strength Electrolyte Solutions Are Caused by Electric Field Induced Water-Water Correlations. *Chem. Phys. Lett.* **2017**, *684*, 433–442.

(52) Wren, S. N.; Donaldson, D. J. Glancing-Angle Raman Spectroscopic Probe for Reaction Kinetics at Water Surfaces. *Phys. Chem. Chem. Phys.* **2010**, *12* (11), 2648–2654.

(53) Tesei, G.; Aspelin, V.; Lund, M. Specific Cation Effects on SCN^- in Bulk Solution and at the Air–Water Interface. *J. Phys. Chem. B* **2018**, *122* (19), 5094–5105. https://doi.org/10.1021/acs.jpcb.8b02303.

(54) Venkateshwaran, V.; Vembanur, S.; Garde, S. Water-Mediated Ion--Ion Interactions Are Enhanced at the Water Vapor--Liquid Interface. *Proc. Natl. Acad. Sci.* **2014**, *111* (24), 8729–8734.

(55) Petersen, P. B.; Saykally, R. J. Evidence for an Enhanced Hydronium Concentration at the Liquid Water Surface. *J. Phys. Chem. B* **2005**, *109* (16), 7976–7980.

(56) SOKHAN, B. V. P.; Tildesley, D. J. The Free Surface of Water: Molecular Orientation, Surface Potential and Nonlinear Susceptibility. *Mol. Phys.* **1997**, *92* (4), 625–640.

(57) Rowlinson, J. S.; Widom, B. *Molecular Theory of Capillarity*; Courier Corporation, 2013.

(58) Benjamin, I. Structure, Thermodynamics, and Dynamics of Thiocyanate Ion Adsorption and Transfer across the Water/Toluene Interface. *J. Phys. Chem. B* **2022**.

(59) Benjamin, Ilan. Mechanism and Dynamics of Ion Transfer across a Liquid-Liquid Interface. *Science* **1993**, *261* (5128), 1558–1560.

(60) Kornyshev, A. A.; Kuznetsov, A. M.; Urbakh, M. Coupled Ion--Interface Dynamics and Ion Transfer across the Interface of Two Immiscible Liquids. *J. Chem. Phys.* **2002**, *117* (14), 6766–6779.
(61) Kikkawa, N.; Wang, L.; Morita, A. Microscopic Barrier Mechanism of Ion Transport through Liquid--Liquid Interface. *J. Am. Chem. Soc.* **2015**, *137* (25), 8022–8025.
(62) Karnes, J. J.; Benjamin, I. Geometric and Energetic Considerations of Surface Fluctuations during Ion Transfer across the Water-Immiscible Organic Liquid Interface. *J. Chem. Phys.* **2016**, *145* (1), 14701.
(63) Morita, A.; Koizumi, A.; Hirano, T. Recent Progress in Simulating Microscopic Ion Transport Mechanisms at Liquid--Liquid Interfaces. *J. Chem. Phys.* **2021**, *154* (8), 80901.
(64) Benjamin, I. Molecular Dynamics Studies on the Effect of Surface Roughness and Surface Tension on the Thermodynamics and Dynamics of Hydronium Ion Transfer across the Liquid/Liquid Interface. *J. Phys. Chem. B* **2020**, *124* (39), 8711–8718.
(65) Willard, A. P.; Chandler, D. The Molecular Structure of the Interface between Water and a Hydrophobic Substrate Is Liquid-Vapor Like. *J. Chem. Phys.* **2014**, *141* (18), 18C519. https://doi.org/10.1063/1.4897249.
(66) Bresme, F.; Chacón, E.; Tarazona, P.; Tay, K. Intrinsic Structure of Hydrophobic Surfaces: The Oil-Water Interface. *Phys. Rev. Lett.* **2008**, *101* (5), 56102.
(67) Petersen, P. B.; Saykally, R. J.; Mucha, M.; Jungwirth, P. Enhanced Concentration of Polarizable Anions at the Liquid Water Surface: SHG Spectroscopy and MD Simulations of Sodium Thiocyanide. *J. Phys. Chem. B* **2005**, *109* (21), 10915–10921.
(68) Devlin, S. W.; Benjamin, I.; Saykally, R. J. On the Mechanisms of Ion Adsorption to Aqueous Interfaces: Air-Water vs. Oil-Water. *Proc. Natl. Acad. Sci.* **2022**, *119* (42), e2210857119. https://doi.org/10.1073/pnas.2210857119.
(69) Schlesinger, I.; Sivan, U. Three-Dimensional Characterization of Layers of Condensed Gas Molecules Forming Universally on Hydrophobic Surfaces. *J. Am. Chem. Soc.* **2018**, *140* (33), 10473–10481.
(70) Nguyen, N. N.; Nguyen, A. V; Steel, K. M.; Dang, L. X.; Galib, M. Interfacial Gas Enrichment at Hydrophobic Surfaces and the Origin of Promotion of Gas

Hydrate Formation by Hydrophobic Solid Particles. *J. Phys. Chem. C* **2017**, *121* (7), 3830–3840.

(71) Doshi, D. A.; Watkins, E. B.; Israelachvili, J. N.; Majewski, J. Reduced Water Density at Hydrophobic Surfaces: Effect of Dissolved Gases. *Proc. Natl. Acad. Sci.* **2005**, *102* (27), 9458–9462.

(72) Teshima, H.; Li, Q.-Y.; Takata, Y.; Takahashi, K. Gas Molecules Sandwiched in Hydration Layers at Graphite/Water Interfaces. *Phys. Chem. Chem. Phys.* **2020**, *22* (24), 13629–13636.

Chapter 5: Probing Aqueous Interfaces With Planar Liquid Sheets

This work was completed in collaboration with Dr. Jake Koralek and Dr. David Hoffman from the SLAC National Accelerator Laboratory.

5.1 Introduction

The importance that liquids and their interfaces play in governing the chemistry and physics of the natural world cannot be overstated. To that end, spectroscopies that probe species in solution have been crucial for developing a detailed understanding of myriad important processes. Despite this, there are limitations on what types of spectroscopy can be used to study chemical systems in solution. In particular, the infrared (IR) and Xray regions of the electromagnetic spectrum are absorbed strongly by water, which makes IR and Xray studies *through* bulk liquids challenging. The development of ultrathin planar liquid sheets has allowed spectroscopic access of IR, Xray, and electron beam radiation to aqueous samples, and has already been used to address many important scientific questions.[1–4] Additionally, planar liquid sheet technology has recently been used to generate liquid-liquid interfaces[5], which offers exciting new methods to study buried surfaces, which have been difficult to probe experimentally due to the sophisticated spectroscopic techniques required to separate the surface signal from the much-larger bulk response.

Liquid sheet technology generates optically smooth layered heterostructures with the advantage that the thickness of individual layers can be controlled, making them optically accessible, even in the case of absorbing media. Liquid microjets and other sheet jets have been used previously in spectroscopic studies, including both Xray techniques[6,7] and nonlinear spectroscopy[8]. The use of a continuously-flowing planar liquid jet system offers several additional benefits to surface sensitive spectroscopy. For example, inherently weak signal strengths of nonlinear experiments often necessitates long acquisition times. A sample that is open to ambient conditions therefore is susceptible to accumulate contaminants from the atmosphere. Long acquisition times also allows for the accumulation of photoproducts generated during the measurement. These contaminants and photoproducts tend to reside on the liquid surface and influence spectral measurements. In addition, chemicals from manufacturers often contain trace amounts of organic contaminants, unless ultra-pure

samples are purchased, which are prohibitively expensive. The planar liquid sheet avoids these problems, with a continuous flow of solution.

Here, we apply the use of planar liquid sheets to study air-water and water-hydrocarbon interfaces with deep UV second harmonic generation spectroscopy (DUV-SHG). First, we demonstrate the feasibility of using this new methodology for extracting meaningful information from SHG measurements by reproducing previous measurements from our laboratory, namely measuring temperature dependent Langmuir isotherms for NaSCN adsorption to the air-water interface. Second, we apply this technique to study a more complicated system, the buried water-heptane and NaSCN-heptane interfaces as a function of temperature. Previous studies have indicated that the mechanism of adsorption for a weakly hydrated anion to the oil-water interface is driven by an increase in entropy.[9] Using our new methodology, we attempt to experimentally confirm these results from theory.

5.2 Materials and Methods

Materials:

NaSCN salt (>98% purity) and anhydrous heptane were purchased from Sigma Aldrich and used without purification. Water used for solution preparation and liquid sheet generation was ultra-pure Millipore water ($18.2\ \Omega,\ < 3\ ppb\ organic\ content$). NaSCN solutions were prepared without Nochromix-cleaned glassware, as was described for solution preparation in earlier chapters.

Flat-jet:

A borosilicate microfluidic flat-jet device developed at the SLAC National Accelerator Laboratory and manufactured by Micronit Microtechnologies was used for planar liquid sheet generation.[2] The flat-jet chip was connected to a syringe pump (Teledyne ISCO Model 260 D) and an HPLC Pump (Shimadzu LC-20AD) via 1/16" PEEK tubing. In-line fritz filters with 20 μm pores were used to filter solutions and prevent clogging of the nozzle. Additionally, pressure dampeners, constructed from an in-line T-connection containing ~2-3 mL of air, were used to reduce pressure fluctuations and ensure stable sheet generation. Liquid from the flat-jet chip was collected in a catcher connected to a solvent trap and was not recycled. For pure water and pure heptane sheets, liquid flow rates of ~4mL /min were used. For liquid-liquid sheets, the outer liquid flow rate was between 3.5-4.3 mL/min, and the inner

liquid flow rate was between 0.5 – 0.9 mL/min. Specific flowrates are indicated in figures and figure captions.

Temperature control of the liquid sheets was achieved through the use of 1/16" stainless steel tubing submerged in a reservoir of temperature-controlled water. The temperature differential between the set temperature and the temperature of the liquid emerging from the nozzle was ~7 °C.

Deep UV Second Harmonic Generation:

The experimental setup employed for the study of aqueous interfaces from planar liquid sheets is very similar to that described in Chapter 2, and only a brief overview is given here.

The output of a Ti:S amplified laser (800 nm, 1 kHz, 100 fs, 4 mJ/pulse) was frequency doubled through a nonlinear BBO crystal to generate the fundamental wavelength at 400 nm. A half-wave plate and polarizer controlled the input polarization. A rotating neutral density filter wheel modulated the input power during scans, and a 10% beam sampler monitored the input intensity. The fundamental light was focused onto the planar liquid sheet with a UV fused silica 50 mm focusing lens. The colinear second harmonic and fundamental were collimated with a UV fused silica lens and spectrally filtered using a Pellin-Broca prism. The SH signal was sent into a monochromator and PMT for photon counting.

The flat-jet device was mounted on a linear 3-axis motorized stage, as well as a 360° rotation mount. The normal to the liquid sheet interface was contained within the xz plane. To determine the centerline of the liquid sheet and ensure it was aligned perpendicular to the plane of the laser table prior to SHG measurements, the locations of the sheet rims were found at 3 distances away from the nozzle (y-direction). The average of these rim locations was then used as the center of the sheet and set as the z position for the scan. The sheet was oriented at a 53° angle of incidence relative to the fundamental beam, which reduced the amount of reflection from the surface and prevented thin-film interference modulations in the SH signal. A scan of the planar liquid sheet was conducted by holding the z and x positions of the sheet constant, and scanning the y position. Individual SH measurements at a given y position were typically collected for 120 s.

Thin Film Interference Images:

Images and thin-film interference patterns were captured using a Dino-Lite Edge Digital Microscope (AM73515MZTL). For thin-film interference patterns, the planar liquid sheet was illuminated with a Thor Labs red LED lamp (LIU630A) or a white light LED source. In order to capture the specular reflection, the microscope was oriented ~30° from the angle of incidence of the LED lamp. Thin film interference patterns were analyzed using a MATLAB software package written by DJ Hoffman.

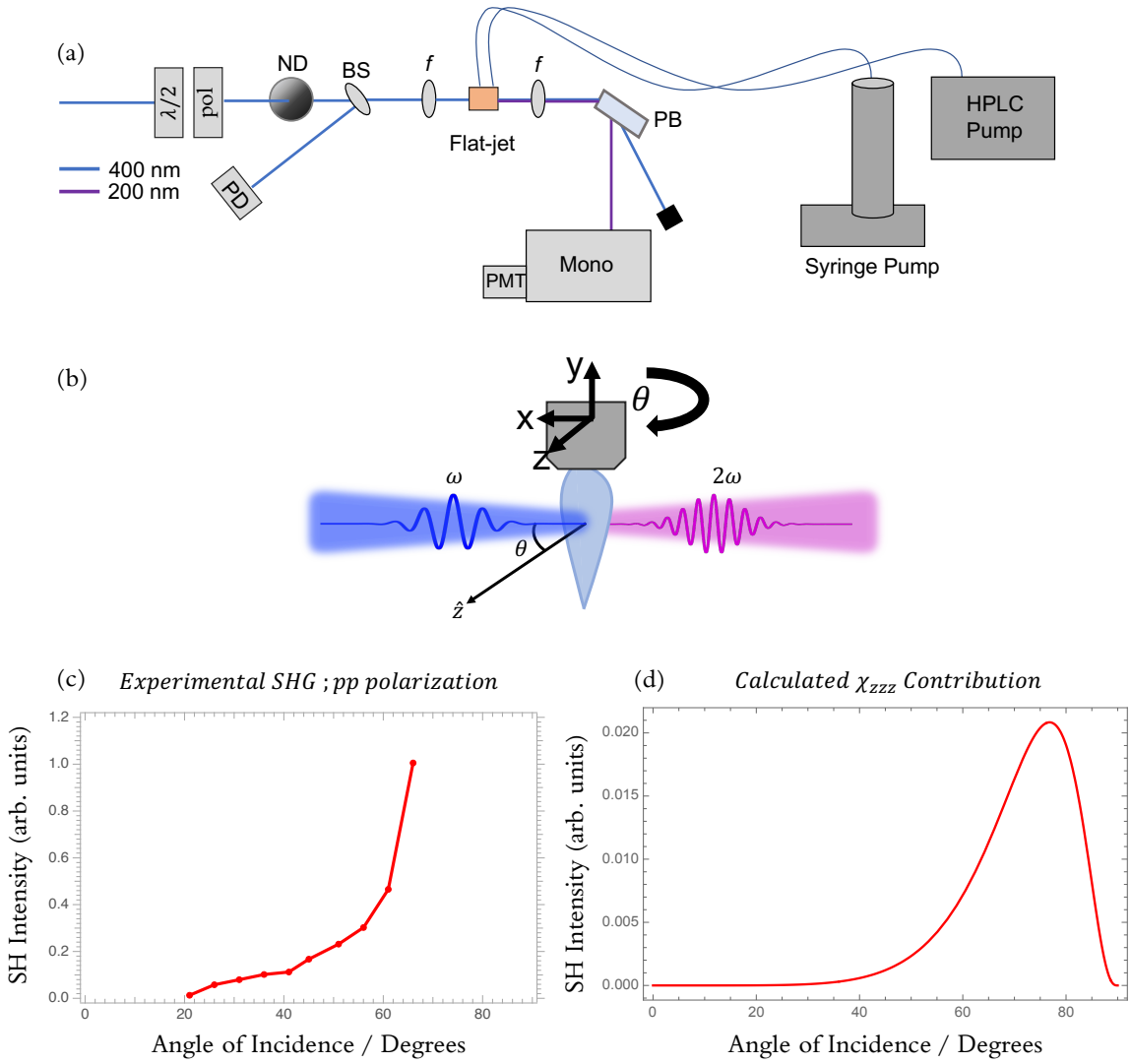

Figure 5.1 – (a) Simplified diagram of the experimental setup. (b) Schematic diagram of SHG from the planar liquid sheet. (c) and (d) Experimental and calculated SH intensities from the planar liquid sheet as a function of angle of incidence of the fundamental beam.

5.3 Planar Liquid Sheet Characteristics

A detailed description of the generation and characterization of the planar liquid sheets is available in the literature.[2,5] Here, only a brief description is given.

The liquid sheets are enabled through the fabrication of a borosilicate chip, which has microfluidic channels (ca. 50 μm) inside and which converge down to the nozzle exit. The channels are supplied with liquid from an appropriate pumping source, such as an HPLC or syringe pump. The controlled collision of the liquid jet channels at the nozzle exit imparts radial momentum to the liquid and causes it to spread into a thin sheet perpendicular to the plane of the channels, with a thick rim around the edge. Eventually, the surface tension of the liquid out-competes the radial momentum from the collision, and the sheet reconverges, forming a second, smaller sheet that is perpendicular to the first. The thickness of the sheet decreases as a function of the distance away from the nozzle, with the dependence scaling as approximately 1/r. With the use of this device, planar sheets can be generated which broadly fall into two categories: (1) ultrathin planar sheets, which are generated by flowing an accelerating gas through the outer microfluidic channels, and which impinge on the liquid (2) thicker planar sheets, which are generated by flowing liquids at higher flow rates and with no accelerating gas. Liquid sheets of type (2) are the ones used in this thesis. An image of a water liquid sheet is shown in Figure 5.2.

Figure 5.2 – Image of a water planar liquid sheet, generated by flowing water from an HPLC pump through the device at 3.75 mL/min. The scale bar is 500 μm.

The thickness of the liquid sheets, d, has been shown to take the form[10,11]:

$$d = \frac{a * R^2}{r} \quad (5.1)$$

Here R is the radius of the colliding jet (i.e. the microfluidic channel radius), a is a scaling factor, and r is the distance away from the nozzle exit. Alternate forms of Equation 5.1 account for the collision angles of the impinging jets, which are held constant in this fabricated chip. The thickness can be experimentally characterized using thin-film interference patterns, which is a well-established procedure in the literature.[12] Figure 5.3 highlights this process for a series of pure water sheets at 3 different flow rates.

Thin-film interference results from reflections inside of the thin water sheet, which gives rise to regions of constructive and destructive interference, and thus the fringe patterns observed in panels (a) in Figure 5.3.

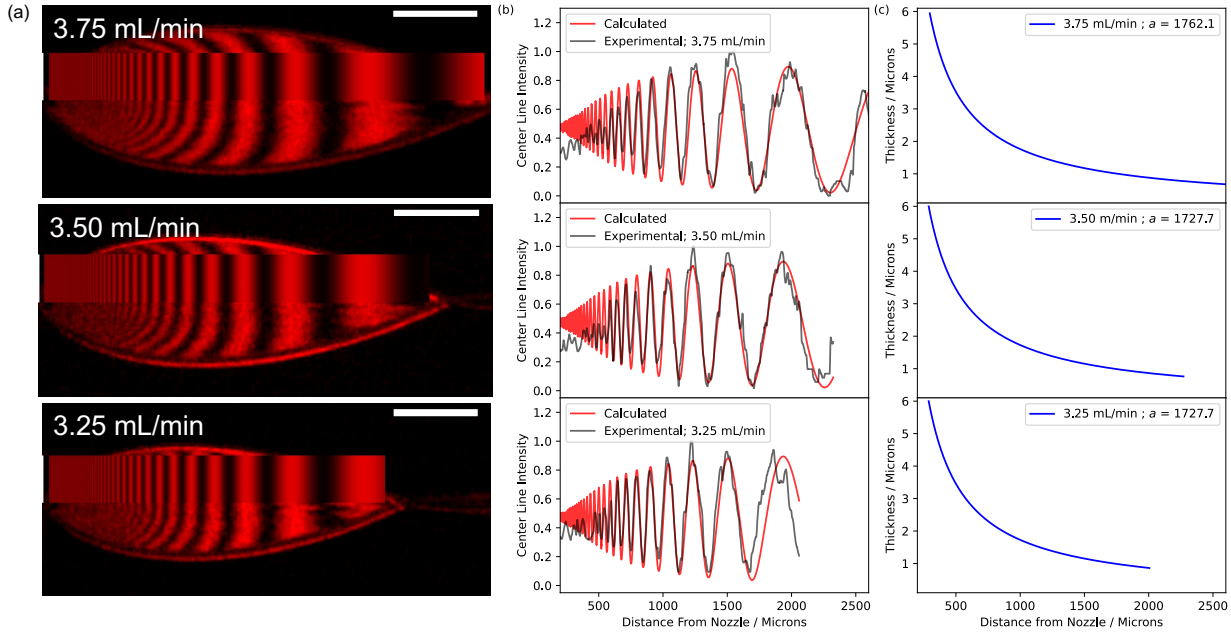

Figure 5.3 – Thin-film interference of pure water sheets. **(a)** Processed images of water sheets. The simulated intensity pattern is shown in the box adjacent to the center line of the sheet. All scale bars are 500 μm **(b)** Centerline intensity for both the experimental (grey) and calculated (red) fringe patterns plotted as a function of distance from the nozzle. **(c)** Thickness profile as a function of distance from the

nozzle. The parameter a contains both the scaling factor and the radius of the microfluidic channel, R^2.

In a single fluid sheet, the fringes all have the same relative intensity. The fringe pattern becomes more complex when a second liquid is introduced into the sheet, a scenario which will be discussed later, in section 5.6. Figure 5.3(b) compares the experimental centerline intensity (grey) of the interference pattern with the calculated intensity pattern (red) as a function of the distance away from the nozzle for water sheets running at 3.75, 3.50, and 3.25 mL/min. Aligning the maxima and minima of the two fringe patterns allows the scaling factor to be determined, which generates the thickness profiles shown in Figure 5.3(c). A useful feature of the liquid sheets is that the sheet thickness as a function of distance from the nozzle is independent of the liquid flow velocity. This can be realized by comparing the calculated centerline intensities for the three different flow rates in Figure 5.3(a) and observing that the dark and bright fringes line up at the same distances from the nozzle. Increasing flowrate generates a larger sheet and therefore allows smaller thicknesses to be accessed at greater distances from the nozzle exit, as is noticeable in comparing the 3.25 and 3.75 mL/min data sets. As can be seen from the thickness profile, liquid sheets employed here typically have thicknesses of 1-5 μm.

5.4 SHG Measurements of Single Liquid Sheets

Typical SHG experiments on liquid surfaces exploit a reflection geometry design.[13–15] This methodology simplifies analysis as the response comes from 1 interface and effects such as attenuation and phase oscillation can be ignored. Due to periodic fluctuations of the planar sheets, a reflection geometry requires frequent optical realignment after the sample to steer the SH signal into the detector. To avoid this problem, SHG measurements of the planar liquid sheets were made in transmission geometry (Figure 5.4).

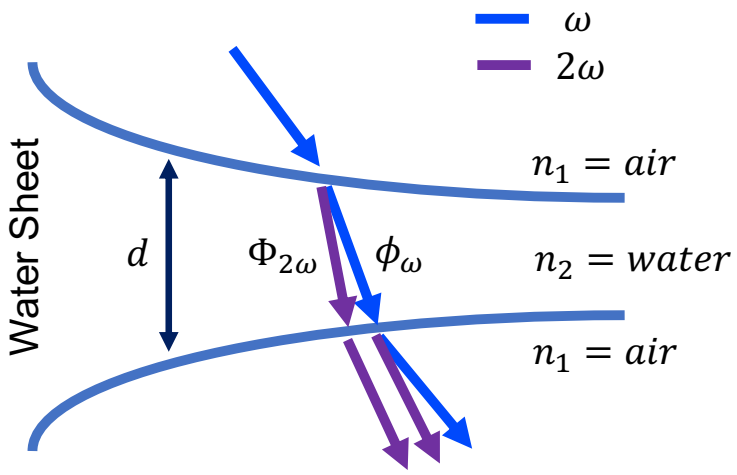

Figure 5.4 – Schematic diagram of SHG through a planar liquid sheet in transmission geometry.

This experimental geometry introduces a second interface where SHG can be generated, and therefore careful consideration of the phase effects between the two interfaces must be considered for properly evaluating the SH signal. There exists a large body of work on optical SHG from solid thin film systems , which has been useful for developing the methodology we employ below.[16–18]

The normal SH intensity from a single interface can be written as:

$$\frac{I_{2\omega}}{I_\omega^2} = |\chi^{(2)}|^2 \quad (5.2)$$

In the case of two interfaces, we add in a second $\chi^{(2)}$ term to account for the generation of SHG at the back surface. Additionally, each $\chi^{(2)}$ term has an associated complex phase factor:

$$\frac{I_{2\omega}}{I_\omega^2} = |\chi^{(2)} e^{i\Phi_{2\omega}} - \chi^{(2)} e^{i2\phi_\omega}|^2 \quad (5.3)$$

Here $\Phi_{2\omega}$ and ϕ_ω are the associated phase factors for the propagation of the SH and the fundamental fields through the liquid. We represent the phase factors as:

$$\Phi_{2\omega} = \frac{2 * \pi * d}{\lambda_{2\omega}} n_{2\omega} \cos(\theta_{2\omega}) \quad ; \quad \phi_\omega = \frac{2 * \pi * d}{\lambda_\omega} n_\omega \cos(\theta_\omega) \quad (5.4)$$

Here d is the thickness of the liquid sheet, λ_i is the wavelength, n_i is the complex, wavelength-dependent refractive index, and θ_i is the angle of incidence relative to the surface normal, for both the SH and fundamental fields. Inserting the phase factors from Equation 5.4 into Equation 5.3, and including the complex refractive index ($n_i = n_i + ik_i$), we can then write the SH intensity as:

$$\frac{I_{2\omega}}{I_{\omega}^2} = |\chi^{(2)}|^2 * (T_{\omega}^2 + T_{2\omega} - 2T_{\omega}T_{2\omega}^{\frac{1}{2}} \cos\left(\frac{4 * \pi * d}{\lambda_{\omega}} \Delta n_{eff}\right) \quad (5.5)$$

$$T_i = 10^{-\varepsilon_i * c * d/\cos(\theta_i)} \quad (5.6)$$

$$\Delta n_{eff} = n_{2\omega} \cos(\theta_{2\omega}) - n_{\omega} \cos(\theta_{\omega}) \quad (5.7)$$

Here the factor T_i represents the transmitted intensity of the fundamental and SH beams, expressed in terms of the molar extinction coefficient, ε_i , concentration, c, and path-length, $d/\cos(\theta_i)$, and $d\Delta n_{eff}$ is the effective difference in refractive index.

From Equation 5.5, one can appreciate that fully coherent oscillations in the SH intensity can be observed as a function of the sheet thickness, d. In the case of a medium that does not absorb at the fundamental or SH wavelengths (for example, water), each T_i term becomes 1 and oscillations of 0 – 4 times the value of $\chi^{(2)}$ from a single interface are observed. As can be seen in Figure 5.5, zero SH intensity is measured at a sheet thickness of 2.5 μm, which corresponds to the thickness where the photons from the front and back interface are 180° out of phase, and the signal is completely nulled. At sheet thicknesses of ~ 1.5 μm and 3.75 μm, maxima in the SH intensity are observed. These thicknesses correspond to the SH photons from the front and back surface being completely in-phase. Because the photons are coherent, the sum of the two electric fields results in a factor of 4 increase in the measured intensity. To determine $|\chi^{(2)}|^2$, SH measurements are taken at various distances away from the nozzle; see Figure 5.5 for a schematic representation.

(a)

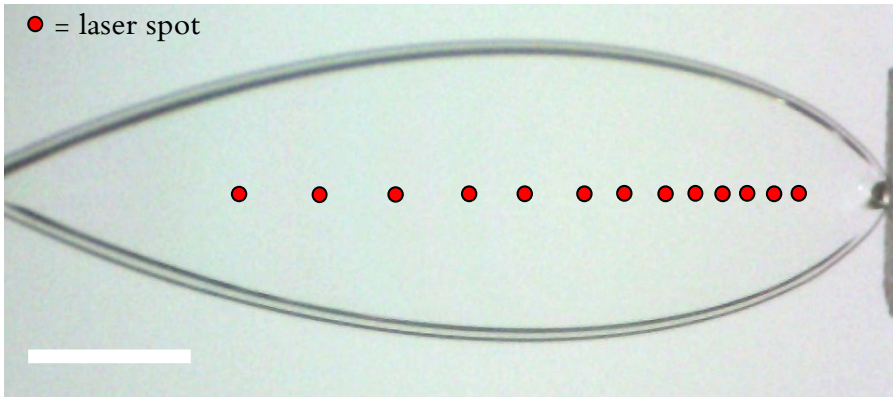

(b)

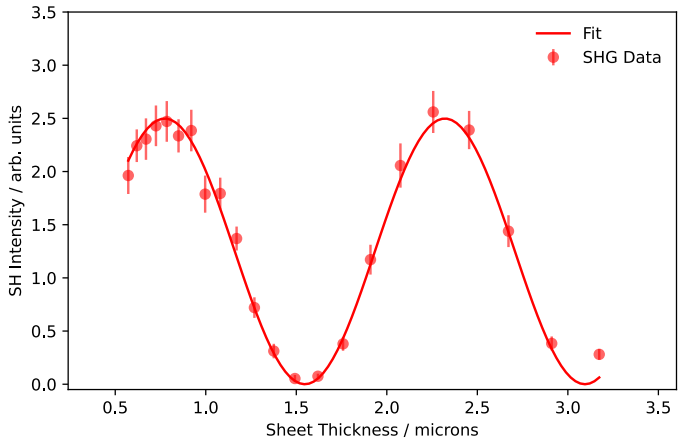

Figure 5.5 – SHG from a pure water planar sheet. **(a)**: Image of a water sheet, running at 3.75 mL/min flow rate. **(b)**: SH intensity of a pure water sheet, measured as a function of sheet thickness, by scanning down the water sheet at increasing step sizes, relative to the nozzle. Laser spots designated on the image are schematic, and do not directly correlate with the thicknesses shown in the SH plot.

Equation 5.5 also reveals that measuring the SH intensity as a function of the sheet thickness provides a sensitive way to measure the refractive index of a liquid at the SH wavelength of 200 nm. Figure 5.6(a) plots example SH intensity oscillations for a range of refractive index values of water at 200 nm (assuming that the refractive index at 400 nm is 1.3436), based on Equation 5.5. It is clear that even subtle changes in the refractive index engender large shifts in the positions of the maxima and minima in the SH intensity. This is most obvious at larger sheet thicknesses, since the effective refractive index difference becomes greater for longer path lengths. For example, a change from $n_{2\omega} = 1.399$ to $n_{2\omega} = 1.409$ for water shifts the maxima by 100 nm for sheet thicknesses around 1.3 μm and by 300 nm for sheet thicknesses

around 3.6 μm, indicated by the vertical lines in Figure 5.4(a). This implies that for correctly extracting refractive index values from SH oscillations, it is important to capture multiple maxima and minima, particularly at larger sheet thicknesses.

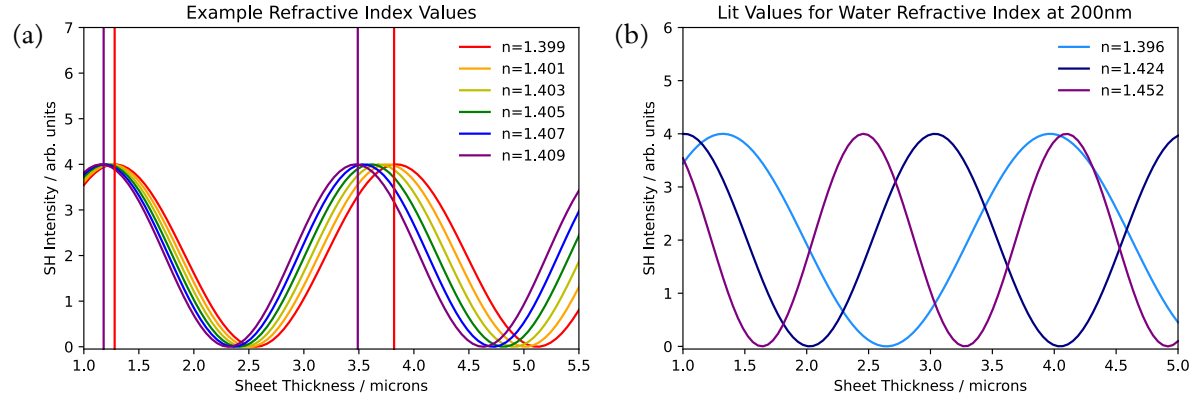

Figure 5.6 – Model SH oscillations as a function of refractive index for water at 200 nm. **(a)** Subtle changes in refractive index engender large shifts in local maxima and minima **(b)** Literature values of refractive index at 200 nm, taken from the following references[19–21]. $\chi^{(2)}$ = 1 in the model fitting.

Figure 5.6(b) plots various values of the refractive index of water at 200 nm (assuming that the refractive index at 400 nm is 1.3436), and highlights the large degree of uncertainty in the refractive index at short wavelengths. Modeling the SH oscillations provides a highly sensitive way to determine the refractive index at 200 nm for a variety of liquids. However, extracting accurate values of the refractive index at 200 nm also requires precise knowledge of the refractive index of the liquid at 400 nm. For that reason, it often useful to when using Equation 5.5 to fit for the effective refractive index difference.

In the case of a solution which absorbs at the fundamental or SH wavelength, large differences in the oscillation behavior are observed, see Figure 5.7. NaSCN serves as a useful prototype solution for understanding the behavior of the liquid sheets under these conditions, as NaSCN absorbs strongly at 200 nm, via a charge-transfer-to-solvent (CTTS) transition, but not at 400 nm. Additionally, the SCN^- anion is among the most surface-active anions from the Hofmeister series, which makes it a useful chromophore for studying ion adsorption phenomena. Figure 5.7 shows a concentration series from pure water to 3.0 M NaSCN solution.

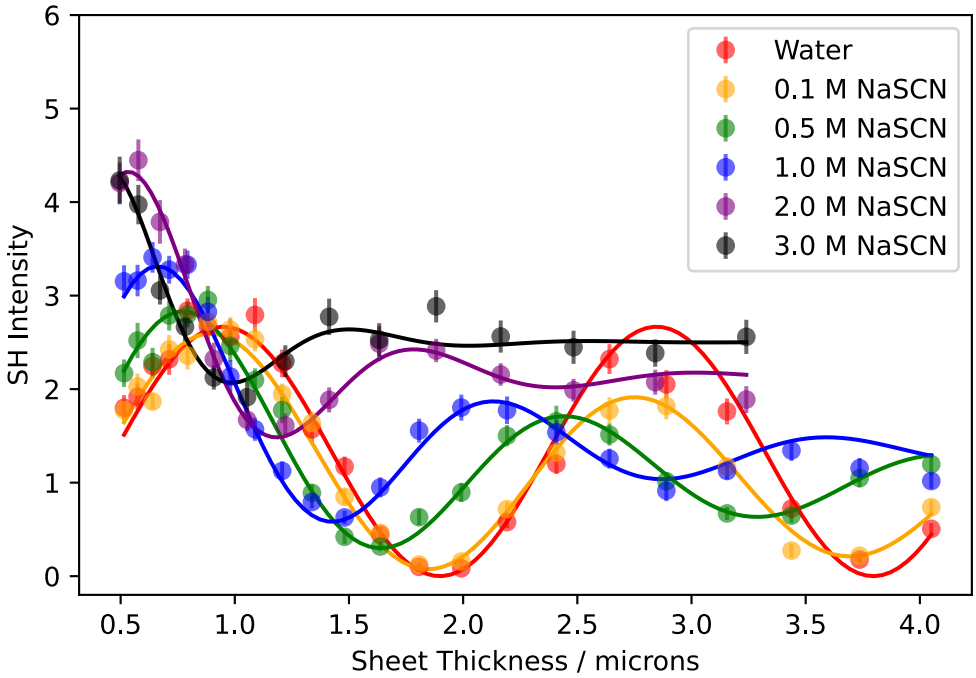

Figure 5.7 – Planar liquid sheet NaSCN concentration series. Concentrations range from pure water to 3.0 M NaSCN solution. Flow rates used were 4.3 mL/min.

There are two major features to keep track of when comparing the SH oscillations of water to NaSCN solutions: (1) the shift in the location of the maxima and minima of the SH oscillations, resulting from a change in the refractive index with salt concentration. Specifically, the refractive index increases with increasing salt concentration, which has the result of shifting the maxima and minima to smaller values of sheet thickness. (2) The magnitude of the SH oscillations decreases with increasing salt concentration. As mentioned above, NaSCN solution absorbs strongly at 200 nm, meaning that the SH photons generated at the front interface are attenuated as they travel through the liquid. At appreciable salt concentration and/or long path lengths, very few photons from the front surface make it all the way through the liquid, essentially damping out any observed coherence. In this case, the SH response is from a single (the back) interface and the observed SH response changes very little with sheet thickness. For instance, in the case of 3.0 M NaSCN (black), very little change in the SH intensity is observed between 3.5 – 1.5 micron sheet thicknesses. However, below 1 micron, oscillations in the SH intensity begin to recover, as the attenuation diminishes and more photons from the front surface penetrate through the sheet.

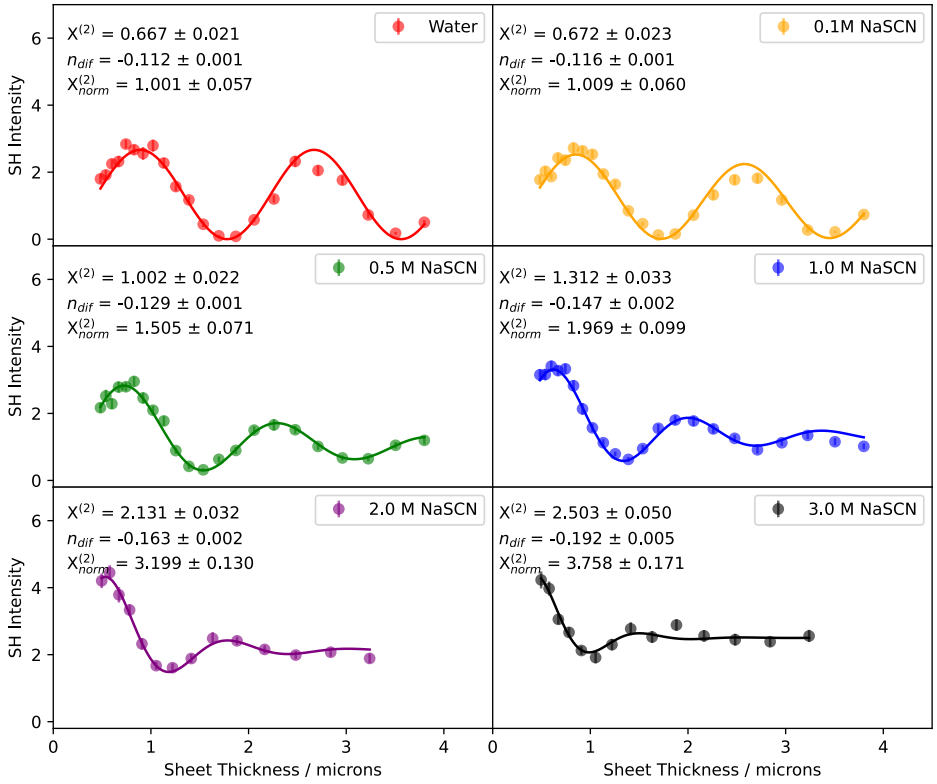

Figure 5.8 – Model fittings and parameters for SH oscillations for pure water to 3.0 M NaSCN at 20°C.

Applying the fitting model (Equation 5.5) to each set of data from water to 3.0 M NaSCN (Figure 5.8) allows for the value of $|\chi^{(2)}|^2$ to be determined, as well as the effective refractive index difference. By normalizing the response of $|\chi^{(2)}|^2$ for each concentration by the response of pure water, the normalized SH response can then be plotted against the bulk concentration of NaSCN and fit to a Langmuir adsorption model (Equation 5.8), as in Figure 5.9(a), yielding the Gibbs free energy of adsorption.

$$\left|\chi^{(2)}\right|^2 \propto \left(A + B\frac{X_{anion}}{(1-X_{anion})e^{\frac{\Delta G}{RT}} + X_{anion}}\right)^2 + \left(C\frac{X_{anion}}{(1-X_{anion})e^{\frac{\Delta G}{RT}} + X_{anion}}\right)^2 \quad (5.8)$$

Here, A represents the non-resonant response from water (normalized to 1), B is the real, non-resonant response of the anion, and C is the imaginary, resonant response of the anion. The methodology and derivation of Equation 5.8 has already been

discussed in detail in Chapter 2, and we refer the reader there for more information. The Gibbs free energy for NaSCN adsorption to the air-water interface via planar liquid sheets was determined to be -7.1 ± 0.9 kJ/mol, in good agreement with the free energy values reported from reflection geometry measurements.[9,22] Figure 5.9(b) plots the effective refractive index difference from the model fitting for each concentration. As is evident, the refractive index difference has a positive, linear correlation with salt concentration. A linear regression to the data in Figure 5.9(b) yields y = -0.0294 – 0.106. Additionally, the refractive index difference provides a useful constraint for the model as well as a check for the "goodness of fit" for any given concentration.

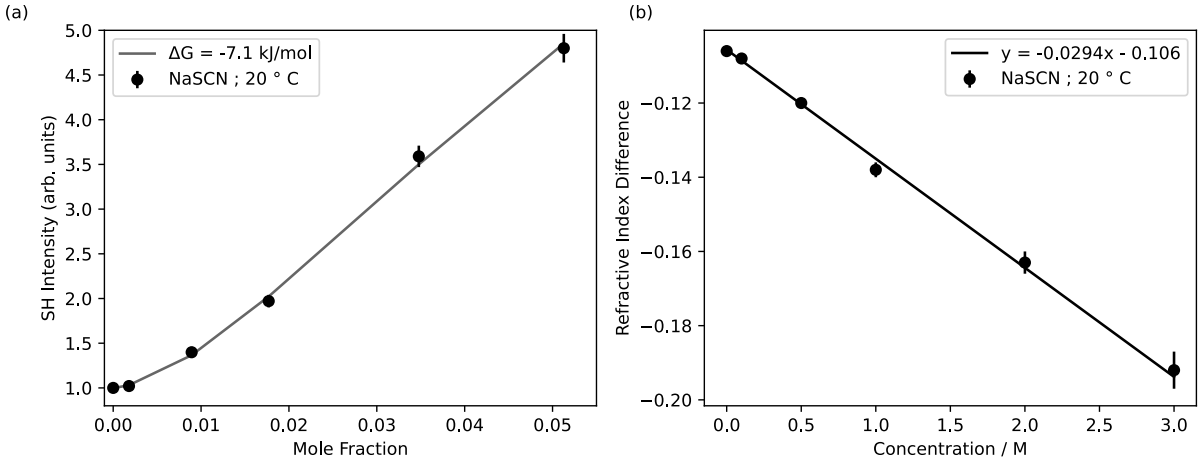

Figure 5.9 – NaSCN fitting parameters. **(a)** Normalized SH intensities for 0 – 3 M NaSCN (0 – 0.055 mole fraction). The data are fit to a Langmuir adsorption isotherm. **(b)** Refractive index difference from the model fitting for pure water to 3.0 M NaSCN, fit to a linear regression. The uncertainties are one standard deviation.

Thus, we have demonstrated a reliable method for determining the magnitude of $|\chi^{(2)}|^2$ from liquid-vapor interfaces in a transmission geometry, and present the framework for modeling spectroscopic SH data in the case of both non-absorbing and absorbing media. This method has been shown to reasonably reproduce measurements made in a reflection geometry.

5.4.1 Temperature-Dependent SHG of Single Liquid Sheets

A useful feature of the planar liquid sheets is that they provide an easy method for controlling the temperature of the liquid delivered to the nozzle. Our experimental setup features a stainless steel 1/16" coil located just before the nozzle, which is submerged in a temperature-controlled water bath. The temperature gradient was determine to be ~7 °C from the stainless steel coil to the liquid coming out of the nozzle for both heating and cooling events. This method provides a much-improved experimental design as compared to heating water in a Petri dish, which is plagued by evaporation and constant monitoring of the sample height for good optical alignment.

In this section, we describe temperature-dependent measurements of NaSCN to the air-water interface. Analysis of the Langmuir isotherms as a function of temperature allows for the Gibbs free energy to be decomposed into the contributing enthalpic and entropic components, yielding vital mechanistic information regarding ion adsorption. Figure 5.10 plots the SH response of pure water at 8 $°C$, 20 $°C$, and 35 $°C$.

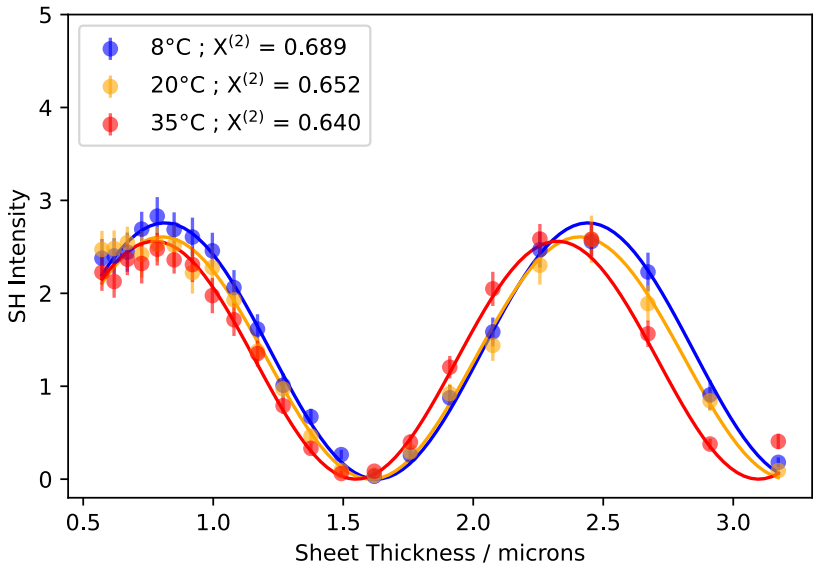

Figure 5.10 – SH intensity of pure water liquid sheets as a function of temperature.

It is observed that the $|\chi^{(2)}|^2$ response of the neat air-water surface decreases with increasing temperature. Increasing temperature from 8 $°C$ to 35 $°C$ decreases the SH response by ~10%. The Eisenthal group reported a significantly larger change in the response of water over a similar temperature range[23], however more recent studies have observed a change in the SH response that is of the same magnitude observed

here[24]. The second harmonic intensity is dependent on both the number density, N_{water}, and the orientation of the species being probed:

$$I_{2\omega} \propto \left|\chi^{(2)}\right|^2 \propto |N_{water} * \langle\beta_{water}\rangle|^2 \quad (5.9)$$

Here, $\langle\beta_{water}\rangle$ is the orientationally averaged hyperpolarizability of water molecules at the interface. Since the change in number density (i.e. the liquid density) of the air-water interface should be small over the temperatures probed here, the observed response is mainly a function of change in the net orientation of water molecules at the surface. Decreasing temperature decreases thermal fluctuation of the liquid and increases net alignment of water dipoles, thus increasing the SHG response. Increasing temperature has the opposite effect.

In the case of an ion adsorbing to the air-water interface, in addition to orientation effects, changes in the resonant response of the chromophore as a function of temperature need to be considered. In Figures 5.11 and 5.12, we plot

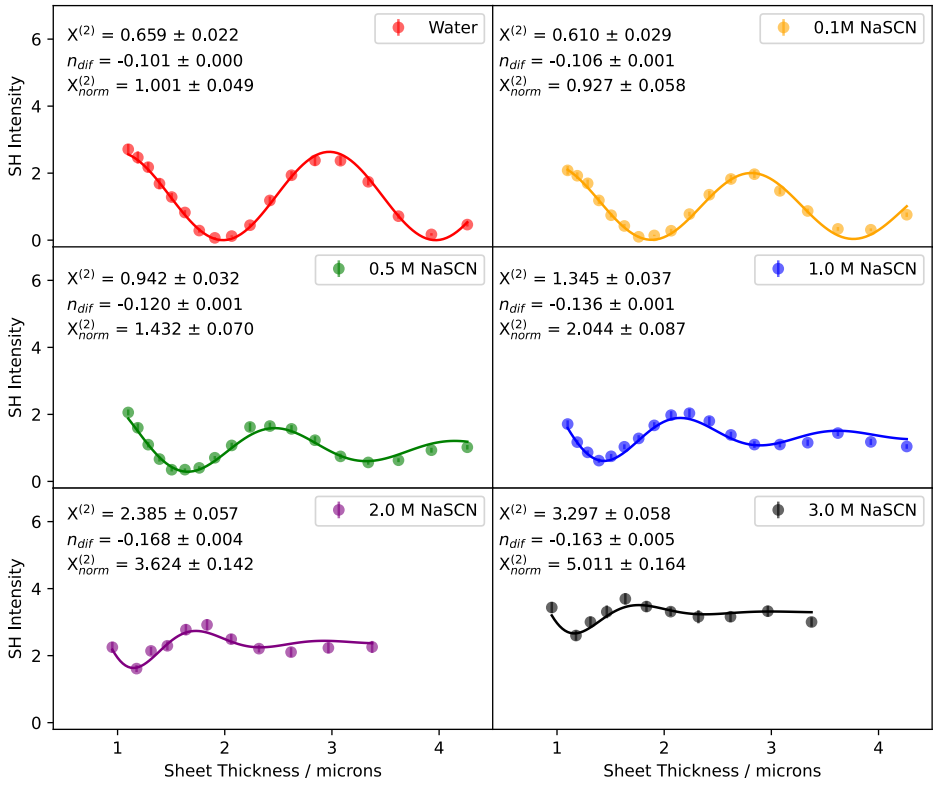

Figure 5.11 - Model fittings and parameters of SH oscillations for pure water to 3.0 M NaSCN at 8°C.

the SH response of NaSCN at 8 °C and 35 °C, respectively. The CTTS band in NaSCN solution exhibits a red shift with an increase in temperature, and because the CTTS peak maximum is located at ~180 nm, we expect the absorption coefficient at 200 to increase with increasing temperature.[25] This should have the result of damping oscillations to a larger extent at a given concentration, when compared to the same concentration at lower temperatures.

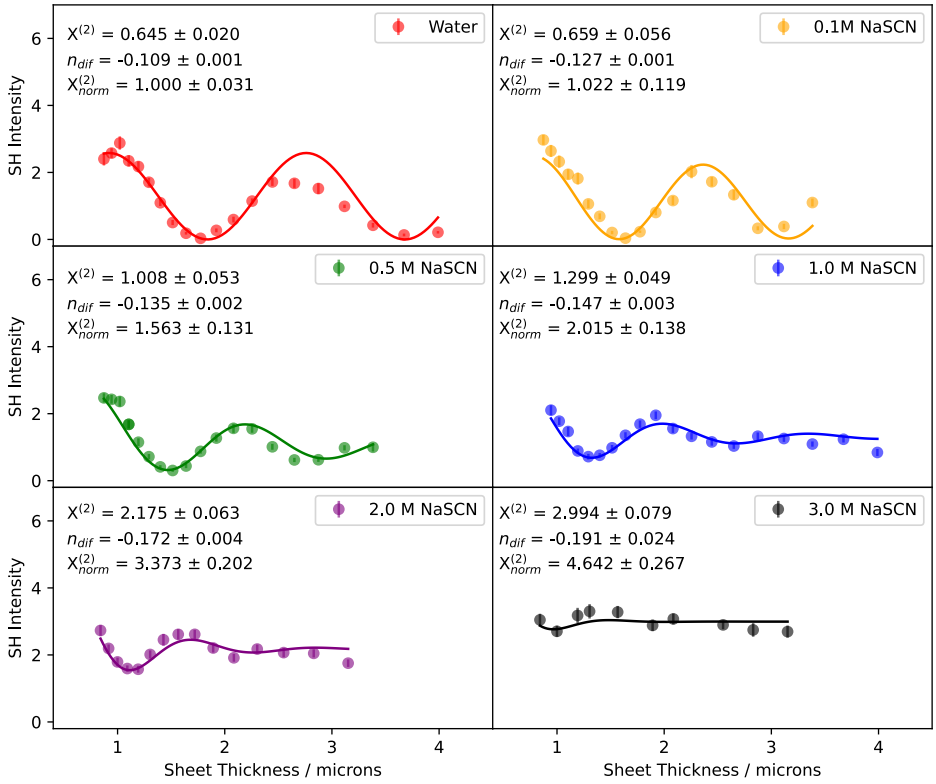

Figure 5.12 - Model fittings and parameters of SH oscillations for pure water to 3.0 M NaSCN at 35°C.

The temperature dependent fitting parameters are shown in Figure 5.13. Figure 5.13(a) plots the normalized SH intensity against bulk anion concentration for 8°C, 20°C, and 35°C. In fitting the temperature-dependent data, we find that a decrease in solution temperature results in larger normalized values of $|\chi^{(2)}|^2$ for NaSCN and an increase in temperature leads to smaller values of $|\chi^{(2)}|^2$, consistent with previously published results from our group[13]. As mentioned above, the absorption coefficient at 200 nm should increase with temperature. We therefore expect that the resonant response of NaSCN at the air-water interface to increase with temperature as well.

However, the opposite trend is observed, which implies that the loss of dipole orientations near the interface from increased thermal fluctuations reduces the signal to a larger degree than the bathochromic shift increases it.

Each data set in Figure 5.13(a) was first fit to an unconstrained Langmuir adsorption model, yielding Gibbs free energies of $\Delta G(8°C) = -6.86 \pm 0.8$ kJ/mol, $\Delta G(20°C) = -7.05 \pm 0.9$ kJ/mol, $\Delta G(35°C) = -7.29 \pm 0.9$ kJ/mol. The resulting parameters of the Langmuir model are summarized in Table 5.1. Interestingly, in the unconstrained model, the effect of temperature on the Gibbs free energy is the opposite of that reported previously by our group.

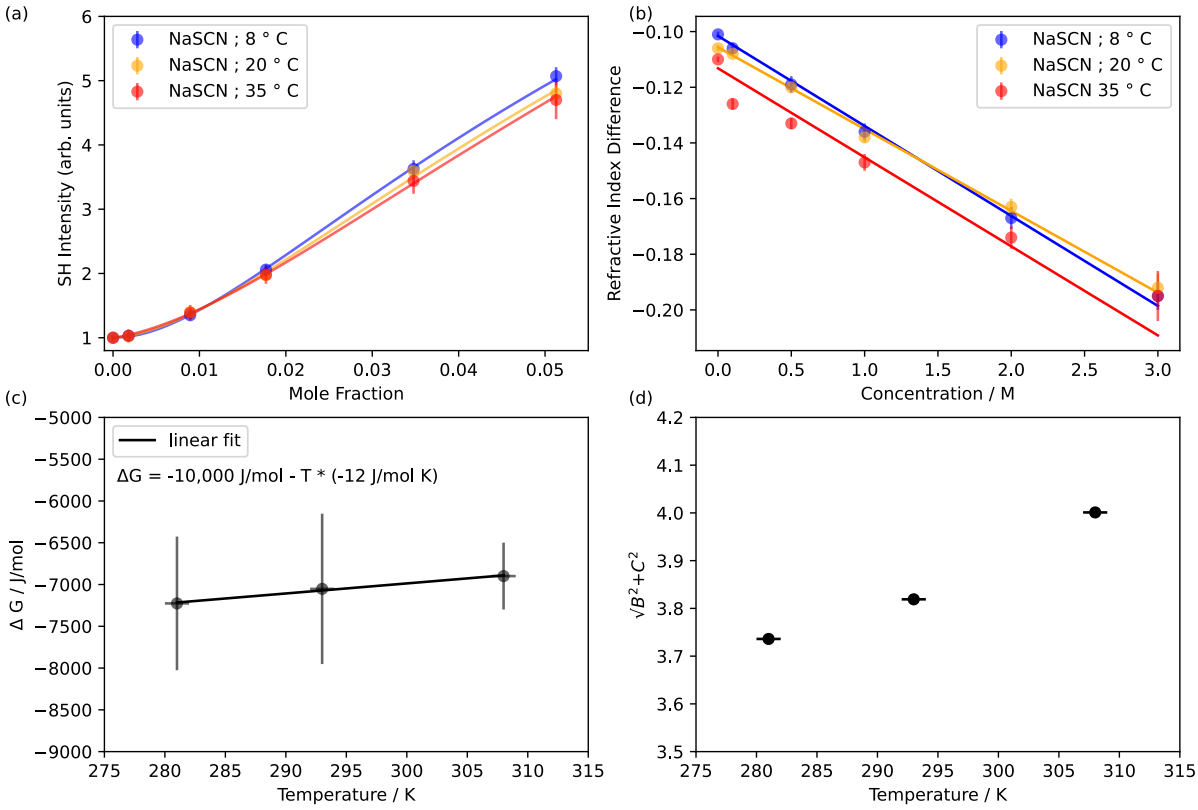

Figure 5.13 – (a) Normalized SH intensities plotted against bulk anion concentration at $8°C$, $20°C$, and $35°C$. Each data set is fit to a constrained Langmuir adsorption model. **(b)** Effective refractive index difference at $8°C$, $20°C$, and $35°C$. **(c)** Gibbs free energies of adsorption plotted against temperature. A linear fit yields the enthalpic and entropic components of the Gibbs free energy. **(d)** Effective susceptibility of thiocyanate as a function of temperature, determined from the "B" and "C" fitting parameters in Table 5.2, plotted against temperature. Uncertainties are one standard deviation

However, this is likely a result of the large uncertainties in the normalized values of $\left|\chi^{(2)}\right|^2$ in the presented data. An analysis of the parameters in Table 5.1 gives insight into this. As mentioned above, the bathochromic shift with increasing temperature should increase the resonant response of the anion. Parameter "C" in Equation 5.8 describes the imaginary(i.e. resonant) component of the thiocyanate susceptibility, and thus we expect this parameter to increase with increasing temperature. In the unconstrained Langmuir fits, parameter "C" was observed to decrease with increasing temperature. If instead, we fit the data to a constrained Langmuir model, given that $C(35°C) > C(20°C) > C(8°C)$, we indeed recover the expected trend that the free energy of adsorption becomes more favorable at lower temperatures and less favorable at higher temperatures. Specifically, we find that $\Delta G(8°C) =$ -7.22 $\pm$ 0.9 kJ/mol, $\Delta G(20°C) =$ - 7.05 $\pm$ 0.9 kJ/mol, and $\Delta G(35°C) =$ - 6.89 $\pm$ 1.1 kJ/mol. The constrained and unconstrained Langmuir fits are essentially identical in shape, and only the constrained fits are plotted in Figure 5.13(a) for clarity. The resulting parameters from the constrained Langmuir fitting model are given in Table 5.2. In Figure 5.13(c), we plot the Gibbs free energy of adsorption versus temperature from the constrained fitting model. This permits the enthalpic(ΔH) and entropic (ΔS) components of ΔG to be determined, by fitting a linear regression to:

$$\Delta G = \Delta H - T\Delta S \quad (5.10)$$

The linear fit yields $\Delta H = -10{,}000 \pm 500$ J/mol and $\Delta S = -12 \pm 2$ J/mol K. Previous measurements from our group reported $\Delta H = -11{,}800 \pm 800$ J/mol and $\Delta S =$ -17 $\pm$ 3 J/mol K.[13] The discrepancy between our reported values stems from large uncertainty in the normalized $\left|\chi^{(2)}\right|^2$, which propagates through to the final entropy and entropy determinations.

However, the important takeaway is that in using a new liquid sheet methodology, we have been able to reproduce that the mechanism of adsorption of NaSCN to the air-water interface is primarily an enthalpy-driven process and is impeded by a reduction in entropy. These results are in good agreement with our groups previously published work and for further discussion of the mechanism of adsorption we refer the reader to the original paper.[13] We now proceed with applying this methodology to the study of liquid-liquid interfaces.

Table 5.1 – Langmuir adsorption model parameters as a function of temperature. No constraint was applied to any parameters in the fitting

Temperature (K)	A	B	C	$\Delta G\ (J\ /\ mol)$
281	1.009	0.0908	3.945	-6860 $\pm$ 800
293	0.998	0.2927	3.808	-7050 $\pm$ 900
308	0.999	0.4348	3.735	-7297 $\pm$ 900

Table 5.2 – Langmuir adsorption model parameters as a function of temperature. The constraint that $C(35°C) > C(20°C) > C(8°C)$ was applied

Temperature (K)	A	B	C	$\Delta G\ (J\ /\ mol)$
281	1.002	-0.0992	3.735	-7226 $\pm$ 800
293	0.998	0.2927	3.808	-7050 $\pm$ 900
308	0.999	0.6712	3.945	-6899$\pm$ 1100

5.5 SHG Measurements of Liquid-Liquid Heterostructures

The use of planar liquid sheet technology, for reliable generation of liquid-liquid heterostructures, has made spectroscopic measurements of buried interfaces optically accessible.[5] To our knowledge, the methodology for extracting SHG from buried interfaces in a transmission geometry has not been presented in the literature. In the following section, we present preliminary temperature-dependent SH data for NaSCN adsorption to the water-heptane interface, with the goal of experimentally determining the enthalpic and entropic components to the overall Gibbs free energy of adsorption.

The liquid-liquid heterostructures are generated by flowing an inner liquid(in our case, heptane) through the center channel of the microfluidic chip, at low flow rates, and an outer liquid(water or NaSCN) through the outer channel, at higher flow rates. The inner liquid is compressed and laterally spreads to create a well-defined layered structure. The thickness of each layer is tunable by adjusting the flowrate of the respective liquid, however, the inner liquid is generally much thinner than the outer one. A representative liquid-liquid heterostructure, water-heptane, is shown in Figure 5.14.

There is an obvious difference in comparing the fringe pattern between pure-water (Figure 5.3) and water-heptane sheets (Figure 5.14). In the water-heptane sheets, there is a clear modulation in the intensity of the fringe pattern, which does

not exist in the single-liquid sheets. This is a result of the additional two interfaces within the sheet from the heptane layer, both of which reflect light inside of the sheet. Both the water layer and heptane layer change in thickness as a function of distance away from the nozzle, resulting in multiple sets of thin-film interference effects, which cause the observed intensity modulation. Calculating the thin-film interference pattern yields the scaling factors needed to determine the thickness of the outer and inner layers. In the case of the water-heptane sheet in Figure 5.13, the outer water layer ranges from 1 - 3 μm (on each side) and the heptane layer ranges from 200 – 900 nm.

As described earlier, in order to understand the SH signal in a transmission geometry, careful consideration of the coherence between the interfaces must be considered.

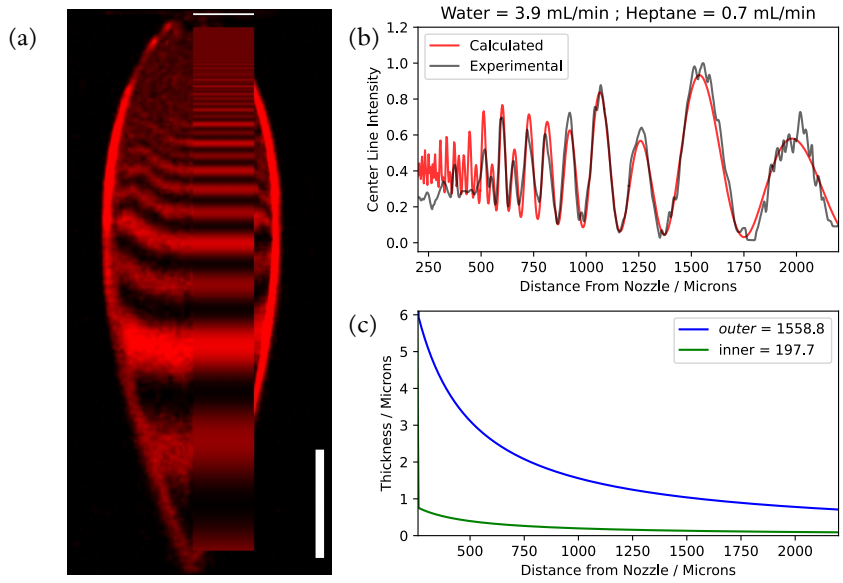

Figure 5.14 – Water-heptane liquid sheet. **(a)** Processed image of a water-heptane sheet, generated by flowing water as the outer liquid at 3.9 mL/min and heptane as the inner liquid at 0.7 mL/min. The scale bar is 500 μm. **(b)** Center line intensity for the calculated (red) and experimental (gray) fringe pattern of the water-heptane sheet. **(c)** Thickness profiles for the outer liquid (water, blue line) and inner liquid (heptane, green line) as a function of distance away from the nozzle.

For liquid-liquid sheets, the coherence becomes more complex, as all 4 interfaces need to be accounted for. Figure 5.15 shows a schematic diagram of the liquid-liquid sheets and the generation of SHG from each surface.

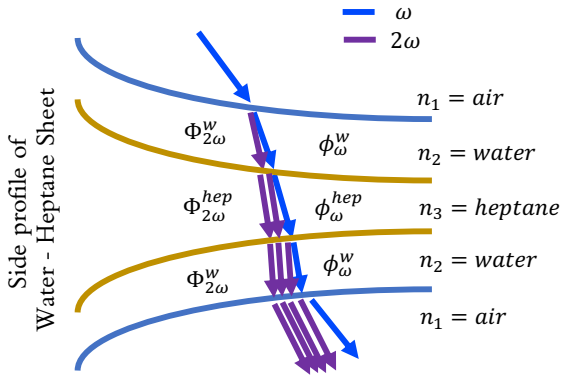

Figure 5.15 – Schematic diagram of SHG from a water-heptane sheet in transmission geometry.

We begin again with the equation for the SH Intensity from a single interface:

$$\frac{I_{2\omega}}{I_{\omega}^{2}} = |\chi^{(2)}|^{2} \quad (5.11)$$

In the case of a water-heptane liquid sheet, the air-water and water-heptane interfaces each have a distinct $|\chi^{(2)}|^{2}$ response. We designate $\chi_0^{(2)}$ as the signal from the outer interfaces (air-water) and $\chi_i^{(2)}$as the signal from the inner interfaces (heptane-water). Each signal has an associated phase factor, resulting in:

$$\frac{I_{2\omega}}{I_{\omega}^{2}} = |\chi_0^{(2)}\left(e^{i\left(2\Phi_{2\omega}^{\mathrm{w}}+\Phi_{2\omega}^{\mathrm{hep}}\right)} - e^{2i\left(\phi_{\omega}^{hep}+2\phi_{\omega}^{w}\right)}\right) + \chi_i^{(2)}\left(e^{i\left(\Phi_{2\omega}^{\mathrm{w}}+2\phi_{\omega}^{w}+2\phi_{\omega}^{hep}\right)} - e^{i\left(\Phi_{2\omega}^{\mathrm{w}}+\Phi_{2\omega}^{\mathrm{hep}}+2\phi_{\omega}^{w}\right)}\right)|^{2} \quad (5.12)$$

Here, $\Phi_{2\omega}^{\mathrm{w}}$ *and* $\Phi_{2\omega}^{\mathrm{hep}}$ correspond to the phase factors of the SH propagating through the water and heptane layers, respectively, and ϕ_{ω}^{w} *and* ϕ_{ω}^{hep} correspond to the phase factors of the fundamental propagating through the water and heptane layers, respectively. The exact form of the phase factors is the same as those in Equation 5.4, with the appropriate refractive indexes inserted. The terms in Equation 5.12 are grouped according to the interface where the signal is generated. Term 1 corresponds to the first interface (air-water), and term 2 corresponds to the last interface (air-

water). Terms 3 and 4 correspond to the inner two interfaces (heptane-water). Since $\chi^{(2)}$ itself is complex-valued, we rewrite Equation 5.12 as:

$$\frac{I_{2\omega}}{I_{\omega}^{2}} = |\chi_0^{(2)}\left(e^{i\left(2\Phi_{2\omega}^{\mathrm{w}}+\Phi_{2\omega}^{\mathrm{hep}}\right)} - e^{2i\left(\phi_{\omega}^{hep}+2\phi_{\omega}^{w}\right)}\right) + fe^{i\theta}\left(e^{i\left(\Phi_{2\omega}^{\mathrm{w}}+2\phi_{\omega}^{w}+2\phi_{\omega}^{hep}\right)} - e^{i\left(\Phi_{2\omega}^{\mathrm{w}}+\Phi_{2\omega}^{\mathrm{hep}}+2\phi_{\omega}^{w}\right)}\right)|^2 \quad (5.13)$$

Where f = $\frac{\left|\chi_i^{(2)}\right|}{\left|\chi_0^{(2)}\right|}$ and $\theta = \arg\left(\frac{\chi_i^{(2)}}{\chi_0^{(2)}}\right)$. In rewriting the equation this way, we can account for the optical phase of the imaginary(resonant) component of the second-order susceptibility, arising from the response of a resonant chromophore (NaSCN). In the case of pure water-heptane sheets, because both liquids do not absorb at the fundamental or SH wavelengths, the response is purely real and $\theta = 0$.

A full expansion of Equation 5.13 to model the SH intensity is difficult, as the model is under-constrained without precise knowledge of many of the optical parameters at a given wavelength and temperature. Instead, we adopt a reduced-parameter approach:

$$\frac{I_{2\omega}}{I_{\omega}^{2}} = \chi_0^{(2)}\big(1 + T_{2\omega}^{4} + T_{2\omega}^{2}(f^2(2 - 2\cos(2\Delta Bh)) - 2\cos(2\Delta Sh)) + 4fsin(\Delta Bh)(T_{2\omega}^{3}\sin(\Delta Sh + \theta) + T_{2\omega}\sin(\Delta Sh - \theta))\big) \quad (5.14)$$

Here $T_{2\omega}$ is the absorption of the SH through the sheet, as in Equation 5.6, and

$$\Delta B = \mathrm{a_{hep}}(\Phi_{2\omega}^{\mathrm{hep}} - 2\phi_{\omega}^{hep})\ ;\ \Delta S = \mathrm{a_{w}}(\Phi_{2\omega}^{\mathrm{w}} - 2\phi_{\omega}^{w}) \quad (5.15)$$

where a_{hep} & a_w are the thicknesses scaling parameters of the heptane and water layers, respectively, and h is the thickness, defined as $h = \frac{1}{y - y_{off}}$, with y being the distance from the nozzle.

Figure 5.16(a) shows the SH intensity oscillations of a pure water-heptane sheet, running water through the outer channel at 3.9 mL/min and heptane through the inner channel at 0.7 mL/min.

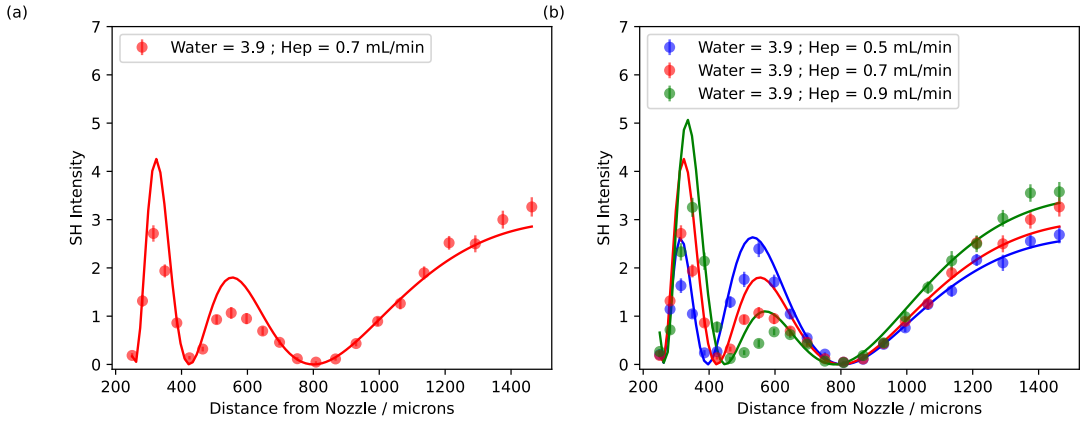

Figure 5.16 – SH oscillations from water – heptane sheets. **(a)** Water – heptane sheet at water = 3.9 mL/min and heptane = 0.7 mL/min flowrates. **(b)** SH oscillations of water – heptane sheets at variable inner heptane flowrates.

The intensity oscillation for the water-heptane sheet is clearly more complex than in the single liquid case. Adjusting the flowrate of the heptane layer in the center of the sheet allows us to sample different thicknesses of the inner layer and to move in and out of phase coherence between the outer and inner interfaces, as can be seen in Figure 5.16(b). For example, a flowrate of water = 3.9 mL/min and heptane = 0.9 mL/min (green line, Figure 5.16(b)), corresponds to an inner layer thickness where the signal between the outer air-water interfaces is amplified from constructive phase coherence, while the signal from the inner heptane-water interface is reduced from destructive phase coherence. Reducing the inner(heptane) flowrate to 0.5 mL/min changes the thickness at a given distance from the nozzle and therefore the resulting constructive and destructive phase interference pattern (blue line, Figure 5.16(b).

Flowing an electrolyte solution through the outer channel allows us to study the adsorption behavior of ions to the water-heptane interface. In Figure 5.17, the SH intensity through NaSCN-heptane sheets is plotted for a series of NaSCN concentrations, measured at $20°C$. As in the NaSCN data presented in the previous section, there is a clear dependence of the oscillation structure on the salt concentration. It is observed that increasing the salt concentration shifts the location of the maxima and minima to larger distances away from the nozzle (smaller sheet thicknesses), as the refractive index of the solution increases with concentration, as expected.

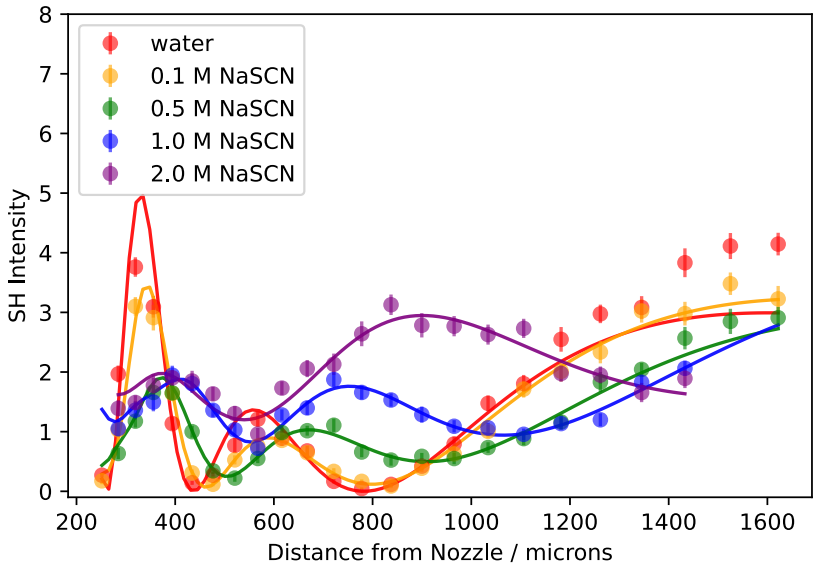

Figure 5.17 – SH oscillations for water-heptane and NaSCN-heptane sheets at 20°C. Flowrates used were water/NaSCN = 3.9mL/min outer flowrate and heptane = 0.7 mL/min for the inner flowrate.

Additionally, the amplitude ratio of the first and second oscillation (located at ~350 and ~550 microns in the case of pure water) begins to shift as a function of concentration. This not only arises due to absorption of the SH propagating through the outer NaSCN layers, but also because the magnitude and phase of the resonant $\chi_i^{(2)}$signal from NaSCN at the water-heptane interface changes with concentration.

Fitting the data in Figure 5.17 with Equation 5.14 allows us to extract the values of $\chi_0^{(2)}$ & $\chi_i^{(2)}$, among other parameters, which are shown in Figure 5.18. In Figure 5.18(a) and 5.18(b), the normalized SH intensities for NaSCN adsorption to the air-water and water-heptane interface are plotted. Each data set is fit to a Langmuir adsorption model, yielding preliminary Gibbs free energies of ~ -2 kJ/mol and ~ -4 kJ/mol for the air-water and heptane-water interfaces. However, significantly more statistics need to be collected before quantitative determination of the Gibbs free energy can be presented with the current fitting model. The fact that extracting $\chi_0^{(2)}$ from the water-heptane fits does not reproduce the normalized intensities from single liquid sheets is an indication that other parameters in the fitting model are not constrained properly.

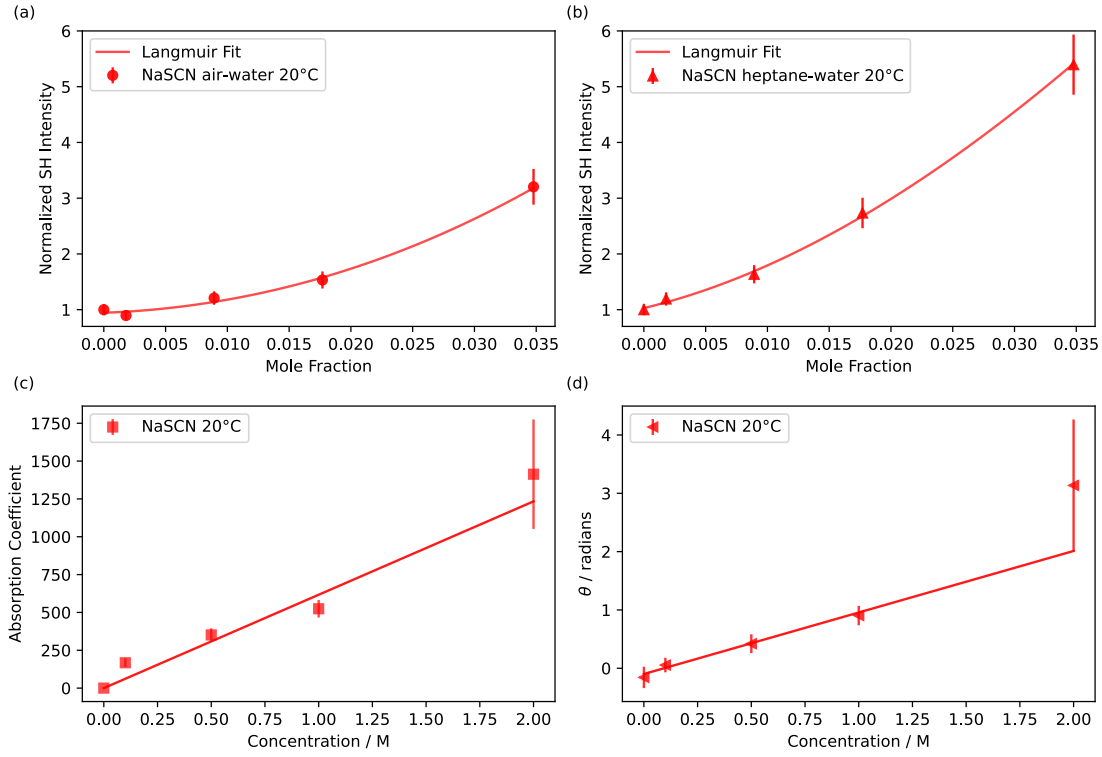

Figure 5.18 – Fitting parameters from NaSCN-heptane sheets. Normalized second harmonic intensities for **(a)** NaSCN adsorption to the air-water interface and **(b)** NaSCN adsorption to the water-heptane interface. Concentration dependence of **(c)** the absorption coefficient for NaSCN and **(d)** phase of the second-order susceptibility, θ.

As can be seen in Figure 5.18 (c) and (d), there is significant deviation of several fitting parameters from the expected trend, which skews the extracted value of $\chi_0^{(2)}$ & $\chi_i^{(2)}$. Nonetheless, the ability to measure and separate $\chi_0^{(2)}$ & $\chi_i^{(2)}$ simultaneously, as well as the phase of the susceptibility is a significant step forward in improving experimental measurements of buried interfaces.

5.5.1 – Temperature Dependent SHG of Liquid-Liquid Heterostructures

Recent experimental work has investigated the adsorption of NaSCN to the water-toluene and water-decane interface, and found that the Gibbs free energy for both of these interfaces agreed within error of each other, and were within error of previous measurements to the air-water and water-graphene interface.[9,13,26] MD simulations, however, found that the mechanism of adsorption to water-toluene and water-decane

was driven by an increase in entropy, rather than being driven by enthalpy. Our goal is to experimentally determine the enthalpic and entropic components to the overall Gibbs free energy, by measuring adsorption isotherms as a function of temperature, as was done in the previous section.

Figure 5.19 shows SH oscillations of a water-heptane sheet at 8°C, 20°C, and 35°C.

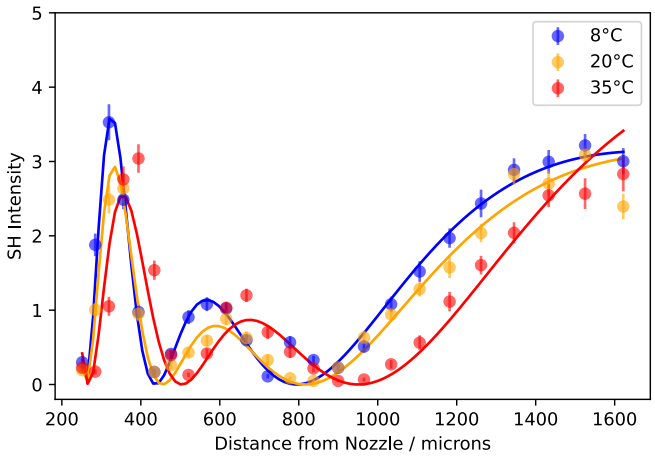

Figure 5.19 – Temperature dependence of SH oscillations for water-heptane sheets. The flowrate used were water = 4.3 mL/min and heptane = 0.7 mL/min

The magnitude of the SH oscillations in the water-heptane sheets has a weak dependence on temperature, which is most noticeable in the first oscillation at ~350 microns down the sheet. The more noticeable difference comes in the shift of each peak location, due to the change in refractive index with temperature.

The temperature dependence of NaSCN-heptane sheets is plotted in Figure 5.20 for 8°C and 35°C. The model fits well to the low concentration data between water and 1.0 M NaSCN solutions. As can be seen in the case of the 8°C and 35°C data sets, the fits to higher concentration (2.0 and 3.0 M) are not as good. This is a result of the loss of the oscillation patterns due to absorption, which makes constraining the fitting parameters difficult. Specifically, there is no upper bound on many of the fitting parameters, since the oscillation patterns at high concentrations all look the same (mostly flat). Measuring more concentrations in the 0-1.5 M regime might improve the fitting for higher concentrations, as we will have a better method for constraining the parameters once we have a quantitative understanding of how all the parameters vary with concentration.

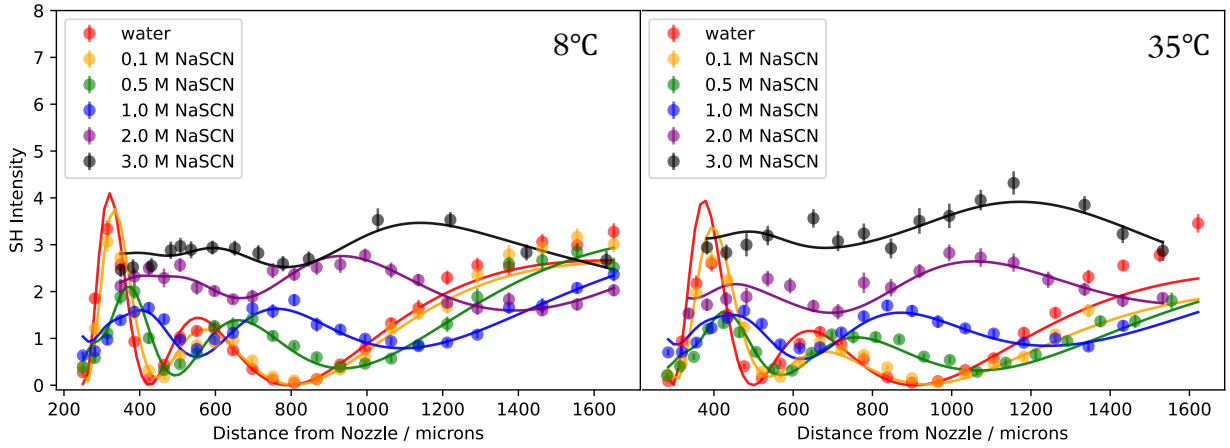

Figure 5.20 - SH oscillations of NaSCN – heptane sheets at 8°C and 35°C.

The temperature-dependent fitting parameters are shown in Figure 5.21. Panel (a) shows the normalized $|\chi_0^{(2)}|^2$ for NaSCN adsorption to the air-water interface and panel (b) shows the normalized $|\chi_i^{(2)}|^2$ for NaSCN adsorption to the heptane-water interface. Interestingly, the temperature dependence for the air-water interface is opposite of what we observed in the case of single-liquid sheets. It is possible that this is a result of the $\chi_0^{(2)}$ and $\chi_i^{(2)}$ parameters being highly correlated. A fitting method that could alleviate this problem is to constrain the values of $\chi_0^{(2)}$ with the information from the single liquid sheets. An even better approach, but more difficult experimentally, would be to measure $\chi_0^{(2)}$ from the jet in a reflection geometry while simultaneously measuring the SH oscillations in transmission mode.

Recent experiments and theory from our group have indicated that the mechanism of adsorption for a weakly hydrated anion to the oil-water interface (water-toluene and water-decane) is driven by an increase in entropy as the ion approaches the surface. The data presented in Figure 5.21(b) qualitatively agree with this mechanistic understanding. However, quantitative determination of the Gibbs free energy at each temperature is currently unsupported, as the uncertainty in the fitting parameters indicates the statistics need to be improved. Experiments are currently on-going to reduce the uncertainty in the normalized values of $|\chi_0^{(2)}|^2$ and $|\chi_i^{(2)}|^2$ in order to quantitatively decompose the Gibbs free energy into its enthalpic and entropic components.

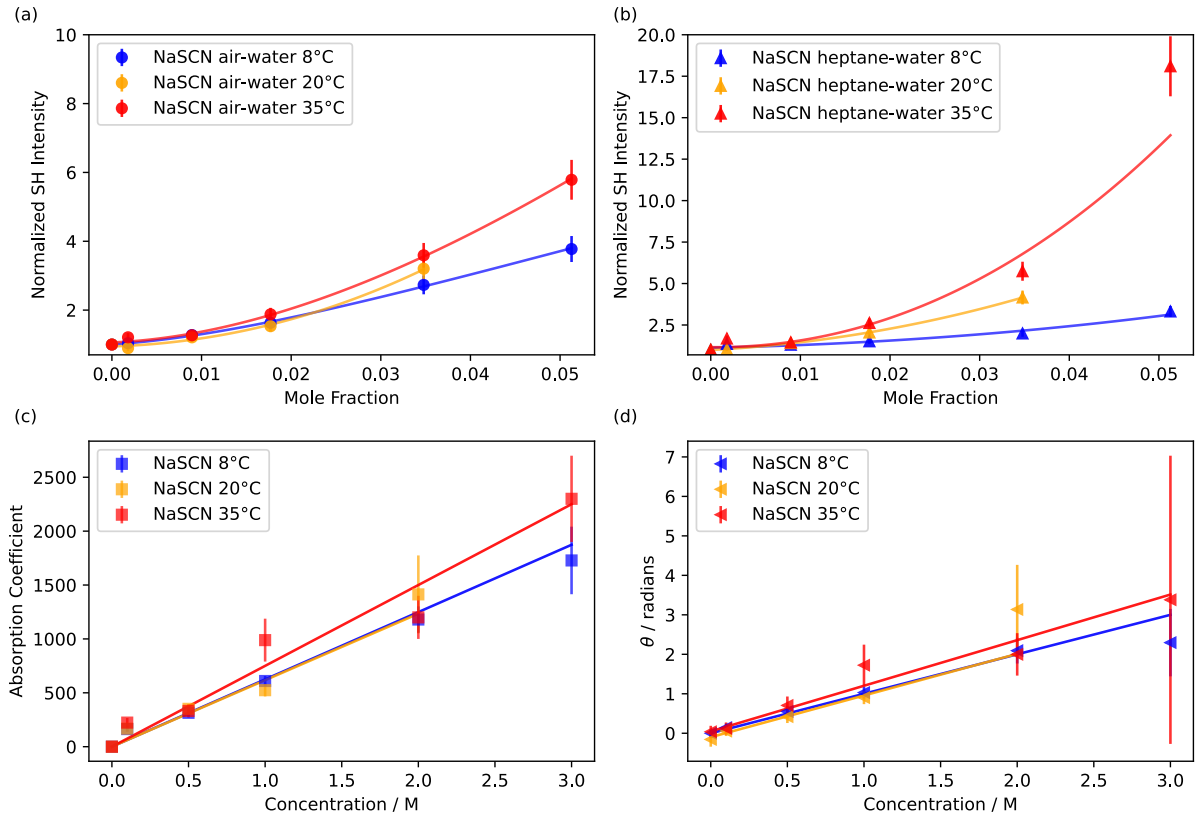

Figure 5.21 – Fitting parameters for temperature dependent NaSCN-heptane sheets.

5.6 Conclusions

We have combined new, planar liquid sheet technology with DUV-SHG spectroscopy to measure ion adsorption to the air-water and water-liquid hydrocarbon interfaces. Using the modeling framework presented herein, we have determined the Gibbs free energy of adsorption for NaSCN to the air-water interface as a function of temperature, and experimentally confirmed that the mechanism of adsorption is driven by enthalpy and impeded by entropy, in agreement with current ion adsorption models. We have also applied this methodology to study a more complicated system, viz. the buried water-liquid hydrocarbon interface. Experimental data for NaSCN adsorption to the water-heptane interface as a function of temperature were presented. These preliminary measurements agree qualitatively with recent theoretical work, in that the mechanism of adsorption to the oil-water interface is driven by an increase in entropy. Experiments to quantitatively determine the enthalpy and entropy components of the overall Gibbs free energy are currently underway. We anticipate this new technology will promote further study of buried

liquid-liquid interfaces, and will thus further develop the detailed understanding of ion adsorption phenomena.

References

(1) Loh, Z.-H.; Doumy, G.; Arnold, C.; Kjellsson, L.; Southworth, S. H.; Al Haddad, A.; Kumagai, Y.; Tu, M.-F.; Ho, P. J.; March, A. M.; Schaller, R. D.; Bin Mohd Yusof, M. S.; Debnath, T.; Simon, M.; Welsch, R.; Inhester, L.; Khalili, K.; Nanda, K.; Krylov, A. I.; Moeller, S.; Coslovich, G.; Koralek, J.; Minitti, M. P.; Schlotter, W. F.; Rubensson, J.-E.; Santra, R.; Young, L. Observation of the Fastest Chemical Processes in the Radiolysis of Water. *Science* **2020**, *367* (6474), 179–182. https://doi.org/10.1126/science.aaz4740.

(2) Koralek, J. D.; Kim, J. B.; Brůža, P.; Curry, C. B.; Chen, Z.; Bechtel, H. A.; Cordones, A. A.; Sperling, P.; Toleikis, S.; Kern, J. F.; Moeller, S. P.; Glenzer, S. H.; DePonte, D. P. Generation and Characterization of Ultrathin Free-Flowing Liquid Sheets. *Nat. Commun.* **2018**, *9* (1), 1353. https://doi.org/10.1038/s41467-018-03696-w.

(3) Lin, M.-F.; Singh, N.; Liang, S.; Mo, M.; Nunes, J. P. F.; Ledbetter, K.; Yang, J.; Kozina, M.; Weathersby, S.; Shen, X.; Cordones, A. A.; Wolf, T. J. A.; Pemmaraju, C. D.; Ihme, M.; Wang, X. J. Imaging the Short-Lived Hydroxyl-Hydronium Pair in Ionized Liquid Water. *Science* **2021**, *374* (6563), 92–95. https://doi.org/10.1126/science.abg3091.

(4) Yang, J.; Dettori, R.; Nunes, J. P. F.; List, N. H.; Biasin, E.; Centurion, M.; Chen, Z.; Cordones, A. A.; Deponte, D. P.; Heinz, T. F.; Kozina, M. E.; Ledbetter, K.; Lin, M.-F.; Lindenberg, A. M.; Mo, M.; Nilsson, A.; Shen, X.; Wolf, T. J. A.; Donadio, D.; Gaffney, K. J.; Martinez, T. J.; Wang, X. Direct Observation of Ultrafast Hydrogen Bond Strengthening in Liquid Water. *Nature* **2021**, *596* (7873), 531–535. https://doi.org/10.1038/s41586-021-03793-9.

(5) Hoffman, D. J.; Bechtel, H. A.; Huyke, D. A.; Santiago, J. G.; DePonte, D. P.; Koralek, J. D. Liquid Heterostructures: Generation of Liquid–Liquid Interfaces in Free-Flowing Liquid Sheets. *Langmuir* **2022**, *38* (42), 12822–12832. https://doi.org/10.1021/acs.langmuir.2c01724.

(6) Wilson, K. R.; Rude, B. S.; Catalano, T.; Schaller, R. D.; Tobin, J. G.; Co, D. T.; Saykally, R. J. X-Ray Spectroscopy of Liquid Water Microjets. *J. Phys. Chem. B* **2001**, *105* (17), 3346–3349. https://doi.org/10.1021/jp010132u.

(7) Lam, R. K.; Smith, J. W.; Rizzuto, A. M.; Karslıoğlu, O.; Bluhm, H.; Saykally, R. J. Reversed Interfacial Fractionation of Carbonate and Bicarbonate Evidenced by X-Ray Photoemission Spectroscopy. *J. Chem. Phys.* **2017**, *146* (9), 094703. https://doi.org/10.1063/1.4977046.

(8) Smolentsev, N.; Chen, Y.; Jena, K. C.; Brown, M. A.; Roke, S. Sum Frequency and Second Harmonic Generation from the Surface of a Liquid Microjet. *J. Chem. Phys.* **2014**, *141* (18), 18C524. https://doi.org/10.1063/1.4896996.

(9) Devlin, S. W.; Benjamin, I.; Saykally, R. J. On the Mechanisms of Ion Adsorption to Aqueous Interfaces: Air-Water vs. Oil-Water. *Proc. Natl. Acad. Sci.* **2022**, *119* (42), e2210857119. https://doi.org/10.1073/pnas.2210857119.

(10) Choo, Y. J.; Kang, B. S. Parametric Study on Impinging-Jet Liquid Sheet Thickness Distribution Using an Interferometric Method. *Exp. Fluids* **2001**, *31* (1), 56–62. https://doi.org/10.1007/s003480000258.

(11) Formation of Thin Flat Sheets of Water. *Proc. R. Soc. Lond. Ser. Math. Phys. Sci.* **1960**, *259* (1296), 1–17. https://doi.org/10.1098/rspa.1960.0207.

(12) Stenzel, O.; others. *The Physics of Thin Film Optical Spectra*; Springer, 2015.

(13) Otten, D. E.; Shaffer, P. R.; Geissler, P. L.; Saykally, R. J. Elucidating the Mechanism of Selective Ion Adsorption to the Liquid Water Surface. *Proc. Natl. Acad. Sci.* **2012**, *109* (3), 701–705. https://doi.org/10.1073/pnas.1116169109.

(14) Devlin, S. W.; Chen, A. A.; Jamnuch, S.; Xu, Q.; Qian, J.; Pascal, T. A.; Saykally, R. J. Agglomeration Drives the Reversed Fractionation of Aqueous Carbonate and Bicarbonate at the Air-Water Interface. **2023**. https://doi.org/10.48550/ARXIV.2301.05786.

(15) Petersen, P. B.; Saykally, R. J. Confirmation of Enhanced Anion Concentration at the Liquid Water Surface. *Chem. Phys. Lett.* **2004**, *397* (1–3), 51–55. https://doi.org/10.1016/j.cplett.2004.08.049.

(16) Dean, J. J.; van Driel, H. M. Graphene and Few-Layer Graphite Probed by Second-Harmonic Generation: Theory and Experiment. *Phys. Rev. B* **2010**, *82* (12), 125411. https://doi.org/10.1103/PhysRevB.82.125411.

(17) Byrnes, S. J. Multilayer Optical Calculations. **2016**. https://doi.org/10.48550/ARXIV.1603.02720.

(18) Gielis, J. J. H.; Gevers, P. M.; Aarts, I. M. P.; van de Sanden, M. C. M.; Kessels, W. M. M. Optical Second-Harmonic Generation in Thin Film Systems. *J. Vac. Sci. Technol. Vac. Surf. Films* **2008**, *26* (6), 1519–1537. https://doi.org/10.1116/1.2990854.

(19) Daimon, M.; Masumura, A. Measurement of the Refractive Index of Distilled Water from the Near-Infrared Region to the Ultraviolet Region. *Appl. Opt.* **2007**, *46* (18), 3811. https://doi.org/10.1364/AO.46.003811.

(20) David J. Segelstein. The Complex Refractive Index of Water. *Masters Thesis* **1981**.

(21) Hale, G. M.; Querry, M. R. Optical Constants of Water in the 200-Nm to 200-Mm Wavelength Region. *Appl. Opt.* **1973**, *12* (3), 555. https://doi.org/10.1364/AO.12.000555.

(22) Petersen, P. B.; Saykally, R. J.; Mucha, M.; Jungwirth, P. Enhanced Concentration of Polarizable Anions at the Liquid Water Surface: SHG Spectroscopy and MD Simulations of Sodium Thiocyanide. *J. Phys. Chem. B* **2005**, *109* (21), 10915–10921. https://doi.org/10.1021/jp050864c.

(23) Goh, M. C.; Hicks, J. M.; Kemnitz, K.; Pinto, G. R.; Heinz, T. F.; Eisenthal, K. B.; Bhattacharyya, K. Absolute Orientation of Water Molecules at the Neat Water Surface. *J. Phys. Chem.* **1988**, *92* (18), 5074–5075. https://doi.org/10.1021/j100329a003.

(24) Fordyce, A. J.; Bullock, W. J.; Timson, A. J.; Haslam, S.; Spencer-Smith, R. D.; Alexander, A.; Frey, J. G. The Temperature Dependence of Surface Second-Harmonic Generation from the Air-Water Interface. *Mol. Phys.* **2001**, *99* (8), 677–687. https://doi.org/10.1080/00268970010030022.

(25) Blandamer, M. J.; Fox, M. F. Theory and Applications of Charge-Transfer-to-Solvent Spectra. *Chem. Rev.* **1970**, *70* (1), 59–93. https://doi.org/10.1021/cr60263a002.

(26) McCaffrey, D. L.; Nguyen, S. C.; Cox, S. J.; Weller, H.; Alivisatos, A. P.; Geissler, P. L.; Saykally, R. J. Mechanism of Ion Adsorption to Aqueous Interfaces: Graphene/Water vs. Air/Water. *Proc. Natl. Acad. Sci.* **2017**, *114* (51), 13369–13373. https://doi.org/10.1073/pnas.1702760114.

Chapter 6: DUV-ESFG of Phenol at the Air-water Interface

This work is adapted from: Mizuno, H.; New Advances in Spectroscopy: Applications to Aqueous Interfaces and Liquid Carbon, **2021,** *UC Berkeley Dissertation*. and is included here with permission from Hikaru Mizuno Shivalee Dey, Katherine J. Oosterbaan, Nathan Odendahl, Dirk R. Rehn, Andreas Dreuw, Phillip L. Geissler, Martin Head-Gordon, Stephen E. Bradforth, and Richard J. Saykally.
Two-photon absorption spectra were measured by the Bradforth Group at University of Southern California, molecular dynamics simulations were performed by the Geissler Group at UC Berkeley, and electronic structure calculations were performed by the M. Head-Gordon Group at UC Berkeley and the Dreuw Group at Heidelberg University.

6.1 Introduction

Surface chemistry is vital to a wide range of chemical processes, spanning the formation of aerosol droplets in the atmosphere to protein-membrane interactions. So far, the contents of this thesis have focused on the adsorption of ions to the air-water and water-liquid hydrophobe interfaces. While these systems are key to understanding the underlying physics of many chemical and physical processes, an understanding of the adsorption behavior of larger, organic molecules is crucial for a full development of surface chemistry. Recent advances in spectroscopy have facilitated the measurement of electronic spectra of ions and molecules at the air-water interface by broadband deep ultraviolet electronic sum frequency generation (DUV-ESFG) spectroscopy.[1–4] Here, we apply this surface-sensitive tool to the study of a prototypical aromatic molecule, phenol (C_6H_5OH), to investigate its solvation structure at the air-water interface.

Phenol is an amphiphilic organic molecule with a hydrophilic hydroxyl group and a hydrophobic phenyl ring. Phenol is of central importance in many biochemical systems, as the phenol motif drives the photochemistry of many larger biochemical structures. The most prominent example is the amino acid tyrosine, which plays a vital role in the water-splitting reaction in photosynthesis.[5] In atmospheric aerosol chemistry, phenol contributes to secondary organic aerosol formation via oxidation

by ozone and NO_x compounds, which can contribute to air quality and climate issues.[6]

The bulk absorption spectrum of aqueous phenol exhibits two main transitions, the first near 4.6 eV (270 nm) and the second near 5.9 eV (210 nm), which correspond to the two lowest $^1\pi\pi^*$ excited states. In addition, there is a $^1\pi\sigma^*$ state that lies between the two $^1\pi\pi^*$ states. The $S_2(1^1\pi\sigma^*)$ potential energy surface (PES) of phenol is dissociative with respect to the O–H bond stretching coordinate, and crosses the bound PESs of the electronic ground state (S_0) and first excited state $S_1(1^1\pi\pi^*)$ to produce two conical intersections (CIs).[7,8] Previous pump-probe studies in the gas phase[9,10] and in cyclohexane[11,12] have reported phenoxy radical and hydrogen atom products on a femtosecond timescale upon directly populating the dissociative $S_2(1^1\pi\sigma^*)$ state by photoexcitation above the $1^1\pi\pi^*/1^1\pi\sigma^*$ CI. In aqueous solution, Oliver et al.[13] reported phenoxy radical and solvated electron formation, but with orders of magnitude difference in timescales for photoexcitation of the higher energy $2^1\pi\pi^*$ state (~200 fs timescale) compared to below the $1^1\pi\pi^*/1^1\pi\sigma^*$ CI (~2 ns time scale), and they proposed a near-threshold autoionization mechanism. Upon photoexcitation above the $1^1\pi\pi^*/1^1\pi\sigma^*$ CI, Riley et al.[10] observed a proton-coupled electron transfer mechanism leading to solvated electron formation. In a recent cluster study, Sandler et al.[14] proposed a sequential proton-coupled electron transfer mechanism where the solvent reorganization stabilizes the charge-transfer state in addition to O–H bond elongation.

At the air/water interface, monolayer formation with no concentration dependence on the molecular orientation has been reported for bulk concentrations below 200 mM.[15–17] Electronic second harmonic generation (ESHG) spectroscopy experiments have reported a highly favorable adsorption free energy to the air/water interface ($\Delta G° = -14.7 \pm 0.4$ kJ mol^{-1})[18] with a favorable orientation, tilted 50 ± 5° relative to the surface normal.[17] Recent work by Tahara et al. showed that photoionization of phenol occurs ca. 10^4 times faster at the air/water interface than in bulk, reflecting the different solvation environment at the interface.[19] Hence, studying the behavior of organic molecules at aqueous interfaces is of central current interest.

Herein, we present the surface-specific electronic $|\chi^{(2)}|^2$-spectrum of phenol at the air/water interface in the deep UV (ca. 5.4-6.2 eV), preliminary two-photon absorption spectral data, and employ MD simulations and electronic structure calculations to elucidate the effects of aqueous solvation in the bulk and at the

interface. Phenol serves as our first prototype molecular system due to its high surface affinity, as well as the importance of its photophysical properties in biological processes.

6.2 Materials and Methods

Phenol (99%, ACROS Organics) was used without further purification. 100 mM phenol solutions were prepared in glassware cleaned with Al-Nochromix and concentrated sulfuric acid solution overnight, then rinsed with copious amounts of ultrapure water (18.2 MΩ.cm at 25 °C, TOC < 5 ppb, Milli-Q, EMD Millipore). Sample solutions were prepared immediately before measurements.

The bulk absorption spectrum was measured in a spectrophotometer (UV-2600, SHIMADZU) in a 10-mm pathlength quartz cuvette at a bulk concentration of 100 μM.

The broadband DUV-ESFG spectrum of phenol at the air/water interface was measured with *ssp*-polarization (*s*-polarized SFG, *s*-polarized 285 nm, and *p*-polarized white light continuum) using the experimental setup described in Chapter 2. The bulk concentration of phenol (100 mM) used corresponds to a surface concentration of ca. 4.4 M.[17] Here, a commercial optical parametric amplifier (Spectra Physics, TOPAS Prime) is used to generate the UV narrowband pulse at ω_1 = 285 nm (4.35 eV, 8 μJ/pulse, FWHM = 2 nm), which is then spatially and temporally overlapped with a spectrally broad white light continuum pulse (50 μJ/pulse, $\omega_2 \approx$ 600-1400 nm) at the solution surface. The generated SF photon is reflected in the phase-matched direction and is spatially and spectrally filtered before being directed into a spectrograph and CCD detector. Samples were contained in a Teflon Petri dish and measured at 293 K.

Bulk two-photon absorption spectra were measured by the Bradforth Group at University of Southern California by mixing 673 nm (1.84 eV) pump with the visible portion of the white light continuum (~300-600 nm) to cover the spectral range of the lowest energy excitations. Both pump and probe beams were overlapped spatially and temporally in a 1-mm flow cell. Differential absorbance (ΔA) of the broadband continuum probe was recorded with and without the pump pulse using a 256-channel silicon photodiode array. The detailed experimental design is described elsewhere.[20,21]

Computational Methods

To examine the effects of aqueous solvation on the electronic transitions of phenol, molecular dynamics simulations were performed by the Geissler Group and electronic structure calculations were performed by the M. Head-Gordon Group and the Dreuw Group. Computing the transition energies of phenol requires equilibrium configurations of the non-electronic degrees of freedom, *i.e.*, the atomic nuclei, as a starting point. Using empirical interaction potentials, such configurations from MD simulations were harvested.

A series of configurations were taken of one phenol molecule surrounded by 267 SPC/E[1] molecules. The LAMMPS molecular dynamics package[22] was used to simulate a likely molecular geometry of a phenol in either bulk liquid or near an air-water interface. The phenol was parameterized with the Amber ff99[23] force field and was kept rigid and planar (*i.e.*, CCOH dihedral angle = 0°, point group: C_s). SPC/E molecules were kept rigid using the SHAKE[24] algorithm, while the phenol was kept rigid using the LAMMPS rigid/nvt command.[25]

"Bulk-like" and "interface-like" configurations were both generated by using a spring relative to the center of mass to secure the phenol either to the center or to the edge of the water droplet. The atomic coordinates of the phenol and nearest water molecules were extracted for deeper electronic structure analysis.

In aqueous solution, there are three dominant phenol-water interactions: phenol can act as a hydrogen bond donor and/or hydrogen bond acceptor, and a weaker OH–φ interaction can occur between water and the π-electron cloud of the ring.[26] At the air/water interface, a highly specific hydration structure is predicted by Tahara and co-workers wherein one water molecule forms a weak OH–φ bond with the phenol π-ring and a second water molecule accepts a hydrogen bond from the phenol –OH group,[27] consistent with the partial hydration proposed by Girault and co-workers.[18] In order to harvest "bulk-like" and "interface-like" configurations for electronic structure calculations, snapshots where phenol was donating, accepting, or donating and accepting hydrogen bonds were selected from the simulation results. A water-phenol contact was classified as a hydrogen bond if the oxygen-oxygen distance was less than 3.5 Å and the angle made by the O–H bond vector with the oxygen-oxygen displacement vector was less than 30°.

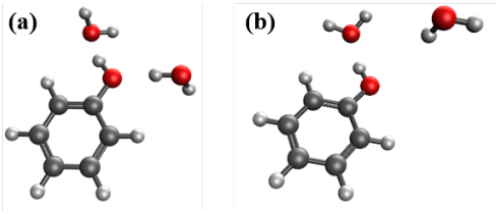

Figure 6.1 - Representative snapshots of (a) bulk-like solvation and (b) interfacial solvation configurations used for ADCMAN electronic structure calculations. The main difference comes from the H-bonding around the -OH moiety.

To limit the computational cost of the electronic structure calculations, only two water molecules nearest to the phenol –OH group were taken into account. The OH–φ interaction was found to not significantly affect the transition energies and the water molecule interacting with the ring was not explicitly included in the electronic structure calculations to limit the computational cost of those calculations. Algebraic Diagrammatic Construction (ADC)[28–30] calculations were performed for an isolated phenol in the gas phase, bulk-like solvated, and interface-like solvated phenol configurations to obtain one-photon oscillator strengths and two-photon cross-sections for degenerate excitation, 3.64 eV + broadband, and 4.35 eV + broadband energies to match experimental conditions. ADC was chosen because of its high accuracy where TDDFT calculations had failed, and because it is one of the few methods in Q-Chem currently capable of calculating the 2PA cross-sections. Calculations were performed in the Def2-TZVPD basis set.

6.3 Results / Discussion

In the bulk absorption spectra, a band centered at 270 nm (4.6 eV) assigned to the $S_0 \rightarrow S_1(1^1\pi\pi^*)$ transition is observed in both the gas phase and aqueous phenol (Figure 6.2, red circles) . The bulk 2-photon-absorption spectrum measured by the Bradforth group (Figure 6.2, black circles), reveals weak intensity in the 4.5 eV region compared to the linear absorption spectrum. The $S_0 \rightarrow S_1(^1\pi\pi^*)$ transition was not observed in in our interfacial broadband DUV-ESFG measurements due to signal interference from bulk fluorescence.

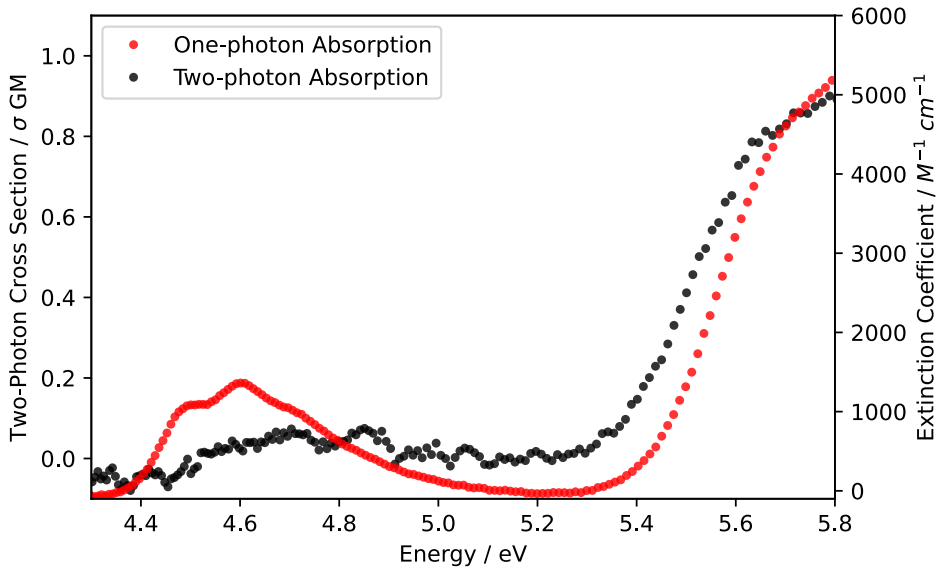

Figure 6.2 - One-photon (red) and two-photon (black) absorption spectra of bulk aqueous phenol. One-photon was measured at a concentration of 100 μM. Two-photon data were measured by the Bradforth Group, using 673 nm pump and ~300-600 nm continuum pulses at a concentration of 850 mM.

In the case of the two-photon (*i.e.* sum frequency) on-resonance and one-photon off-resonance homodyne-detection condition employed here, the normalized ESFG signal intensity is proportional to $|\chi^{(2)}|^2$, where $\chi^{(2)}$ is the second-order nonlinear susceptibility:

$$I_{\mathrm{ESFG}} \propto \left|\chi^{(2)}\right|^2 \propto \sum_n \frac{|\mu_{0n}(\alpha_{0n})_{2\mathrm{PA}}|^2}{(\omega_n - \omega_{\mathrm{SFG}})^2 + \Gamma_n^2} \qquad (6.1)$$

Here, μ_{0n} is the one-photon absorption transition dipole matrix element and $(\alpha_{0n})_{2PA}$ is the two-photon absorption polarizability tensor element connecting the ground state to excited state n, Γ_n is the linewidth of the transition, ω_n is the transition energy between the ground state and excited state, and ω_{SFG} is the sum frequency of the input photons.[31,32] The selection rules for interface specific ESFG spectroscopy under this condition require a transition to be simultaneously one-photon and two-photon active.[3,31,32] The low absorption of the $S_0 \rightarrow S_1(^1\pi\pi^*)$ transition in the two-photon and broadband DUV-ESFG spectra suggests a weak two-photon cross-section for the lowest electronic excitation.

The absorption spectra at higher energies are shown in Figure 6.3(a). No fine structure is observed in the bulk aqueous absorption spectrum, due to inhomogeneous broadening, as solvent fluctuations create a continuum of possible

local solvation environments.[33] A shoulder arising from higher energy transitions is present; however, measuring one-photon absorption at these higher energies in aqueous solution presents a challenge experimentally because the water electronic absorption onset begins near ~6.4 eV (194 nm). Further experiments are underway to measure two-photon spectra at these higher energies by mixing 340 nm (3.64 eV) and a continuum pulse.

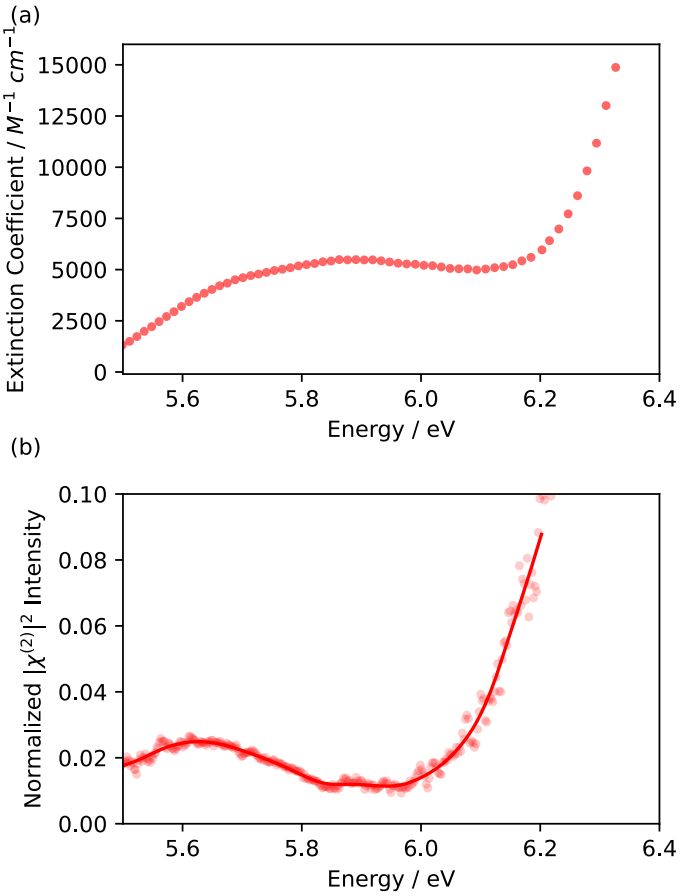

Figure 6.3 - Electronic spectra of aqueous phenol. (a) bulk one-photon absorption spectrum of aqueous phenol measured at 100 μM and (b) $|\chi^{(2)}|^2$-interfacial spectrum measured with broadband DUV-ESFG spectroscopy at a concentration of 100 mM. All spectra were measured at room temperature (293 K).

Compared to the bulk one-photon absorption spectra, the interfacial $|\chi^{(2)}|^2$-spectrum (Figure 6.3(b)) measured with broadband DUV-ESFG spectroscopy appears to exhibit a redshift and a slight change in the spectral shape. The spectral differences

likely arise from the differences in selection rules in the spectroscopy techniques as well as a change in the solvation environment.

As presented above, ESFG intensity is proportional to the product of the one-photon and two-photon cross-sections. The two-photon spectra at higher energies (ca. 5.7-6.3 eV) have yet to be measured so we cannot definitively say whether the differences in the spectral shape in the 5.4-6.2 eV region are purely due to selection rules. However, we can elucidate the effects of solvation by comparing with MD simulations and electronic structure calculations. The highly specific hydration structure at the interface and differences in local solvation environment relative to bulk will lead to some shifts in the electronic spectra. In 4-methylphenol (*p*-cresol), Fornander et al. found that discrete hydrogen bonding motifs (viz. phenol as a hydrogen bond donor vs. acceptor, or both) can cause small spectral shifts (~2-4 nm, ~0.05-0.1 eV) in the $S_0 \rightarrow S_1(1^1\pi\pi^*)$ and $S_0 \rightarrow S_3(2^1\pi\pi^*)$ transitions.[34] Molecular orbitals from the ADC calculations of phenol in representative solvation environments are presented in Figure 6.4 and the transition energies and associated oscillator strengths and two-photon cross-sections are presented in Tables 6.1 and 6.2.

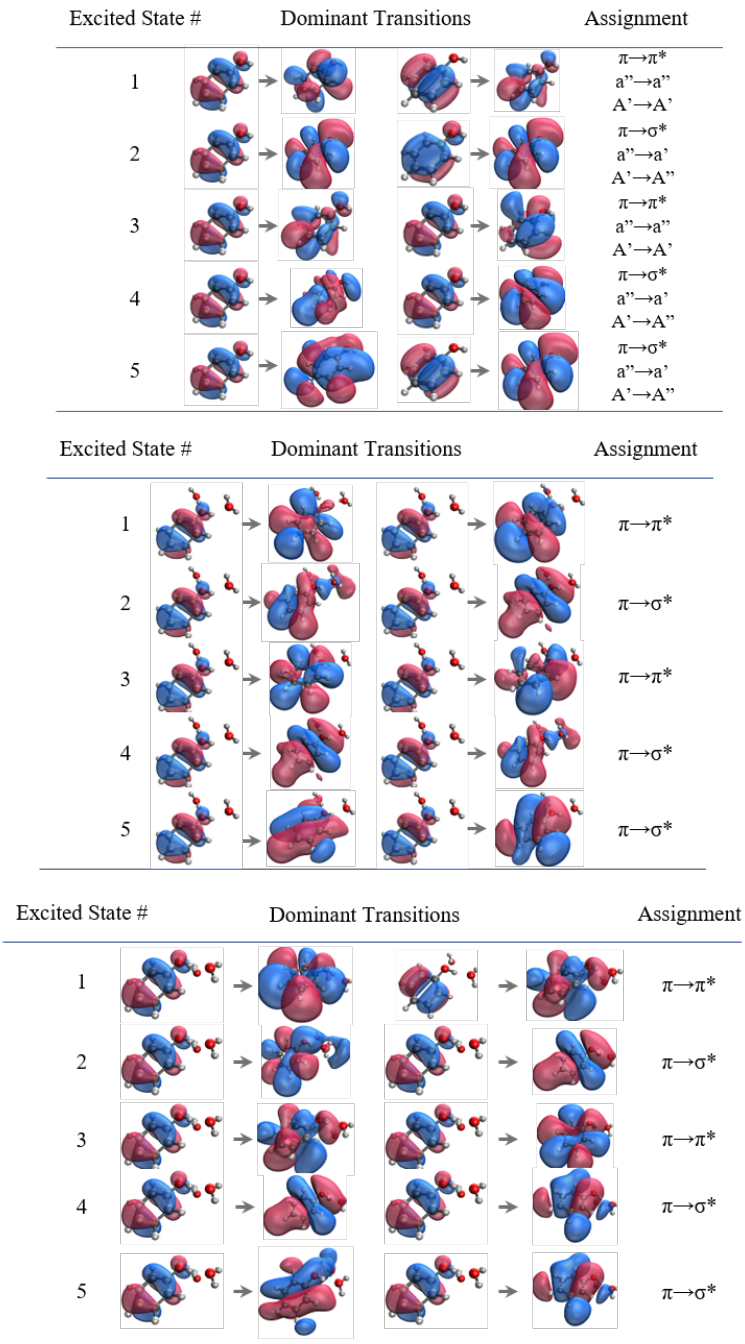

Figure 6.4 - Molecular orbitals of dominant transitions and assignments for phenol in gas phase (top), bulk-like solvation (middle), and interface-like solvation (bottom) environments. The symmetry labels for the orbitals and excitations in the gas phase are in the C_s point group.

Table 6.1 - Gas phase electronic transition energies and associated one-photon absorption oscillator strengths and two-photon absorption cross-sections for (a) degenerate 2PA excitation, (b) 3.64 eV + broadband excitation, and (c) 4.35 eV + broadband excitation.

(a)

Exc State #	Transition Energy (eV)	1PA Osc	2PA (par)	2PA (per)	pol. ratio	Assignment
1	4.9	0.0295	8.59	6.39	1.34	$\pi\rightarrow\pi^*$ a"→a" A'→A'
2	5.8	0.0002	0.57	0.42	1.33	$\pi\rightarrow\sigma^*$ a"→a' A'→A"
3	6.1	0.0970	110.78	38.05	2.91	$\pi\rightarrow\pi^*$ a"→a" A'→A'
4	6.4	0.0032	36.91	27.68	1.33	$\pi\rightarrow\sigma^*$ a"→a' A'→A"
5	6.8	0.0000	11.80	8.85	1.33	$\pi\rightarrow\sigma^*$ a"→a' A'→A"

(b)

Exc State #	Transition Energy (eV)	1PA Osc	2PA (par)	2PA (per)	pol. ratio	Assignment
1	4.9	0.0295	12.08	9.53	1.27	$\pi\rightarrow\pi^*$
2	5.8	0.0002	0.75	0.85	0.88	$\pi\rightarrow\sigma^*$
3	6.1	0.0970	118.12	40.40	2.92	$\pi\rightarrow\pi^*$
4	6.4	0.0032	38.22	28.86	1.32	$\pi\rightarrow\sigma^*$
5	6.8	0.0000	11.90	8.93	1.33	$\pi\rightarrow\sigma^*$

(c)

Exc State #	Transition Energy (eV)	1PA Osc	2PA (par)	2PA (per)	pol. ratio	Assignment
1	4.9	0.0283	25.70	23.68	1.09	$\pi \rightarrow \pi^*$
2	5.8	0.0003	2.82	3.95	0.71	$\pi \rightarrow \sigma^*$
3	6.1	0.0983	151.64	50.15	3.02	$\pi \rightarrow \pi^*$
4	6.3	0.0029	48.74	38.41	1.27	$\pi \rightarrow \sigma^*$
5	6.8	0.0001	12.89	9.89	1.30	$\pi \rightarrow \sigma^*$

Table 6.2 - Electronic transition energies and associated one-photon absorption oscillator strengths and two-photon absorption cross-sections for (a) bulk-like solvated 3.64 eV + broadband excitation, (b) bulk-like solvated 4.35 eV + broadband excitation, and (c) interface-like solvated 4.35 eV + broadband excitation.

(a)

Exc State #	Transition Energy (eV)	1PA Osc	2PA (par)	2PA (per)	pol. ratio	Assignment
1	4.9	0.0257	10.9	8.5	1.28	$\pi \rightarrow \pi^*$
2	5.9	0.0013	2.9	1.5	1.92	$\pi \rightarrow \sigma^*$
3	6.1	0.0977	118.6	38.6	3.07	$\pi \rightarrow \pi^*$
4	6.4	0.0039	42.4	31.9	1.33	$\pi \rightarrow \sigma^*$
5	6.8	0.0002	13.5	9.4	1.44	$\pi \rightarrow \sigma^*$

(b)

Exc State #	Transition Energy (eV)	1PA Osc	2PA (par)	2PA (per)	pol. ratio	Assignment
1	4.9	0.0257	22.5	20.1	1.12	$\pi \rightarrow \pi^*$
2	5.9	0.0013	5.9	5.9	0.99	$\pi \rightarrow \sigma^*$
3	6.1	0.0977	153.9	48.0	3.21	$\pi \rightarrow \pi^*$
4	6.4	0.0039	52.5	40.6	1.29	$\pi \rightarrow \sigma^*$
5	6.8	0.0002	21.5	14.7	1.46	$\pi \rightarrow \sigma^*$

(c)

Exc State #	Transition Energy (eV)	1PA Osc	2PA (par)	2PA (per)	pol. ratio	Assignment
1	4.8	0.0368	54.6	56.1	0.97	$\pi \rightarrow \pi^*$
2	5.4	0.0011	12.2	15.4	0.79	$\pi \rightarrow \sigma^*$
3	5.9	0.1367	256.7	78.1	3.29	$\pi \rightarrow \pi^*$
4	6.1	0.0035	69.2	46.6	1.49	$\pi \rightarrow \sigma^*$
5	6.2	0.0006	36.4	25.4	1.43	$\pi \rightarrow \sigma^*$

The ADC results predict redshifts in the excitation energies for phenol in the "interface-like" configuration wherein phenol acts as a hydrogen bond donor relative

to bulk-like configurations wherein phenol is both a hydrogen bond donor and acceptor. These results align with our measured broadband DUV-ESFG spectra that shows an apparent redshift in the $|\chi^{(2)}|^2$-spectrum and are also consistent with theoretical results of Fornander et al.[34]

6.4 Conclusions

The results of our broadband DUV-ESFG spectroscopy measurements of phenol at the air/water interface, combined with measured bulk two-photon spectra, suggest that the lowest electronic excitation ($1^1\pi\pi^*$) has a weak two-photon extinction coefficient, and is therefore not SF active. At higher energies, corresponding to $1^1\pi\sigma^*$and $2^1\pi\pi^*$ transitions, the highly specific hydration structure at the interface leads to an apparent redshift in the interfacial spectrum. Further work is necessary to elucidate the exact role of selection rules on the interfacial $|\chi^{(2)}|^2$-spectrum of phenol.

References

(1) Rizzuto, A. M.; Irgen-Gioro, S.; Eftekhari-Bafrooei, A.; Saykally, R. J. Broadband Deep UV Spectra of Interfacial Aqueous Iodide. *J. Phys. Chem. Lett.* **2016**, *7* (19), 3882–3885. https://doi.org/10.1021/acs.jpclett.6b01931.

(2) Mizuno, H.; Rizzuto, A. M.; Saykally, R. J. Charge-Transfer-to-Solvent Spectrum of Thiocyanate at the Air/Water Interface Measured by Broadband Deep Ultraviolet Electronic Sum Frequency Generation Spectroscopy. *J. Phys. Chem. Lett.* **2018**, *9* (16), 4753–4757. https://doi.org/10.1021/acs.jpclett.8b01966.

(3) Bhattacharyya, D.; Mizuno, H.; Rizzuto, A. M.; Zhang, Y.; Saykally, R. J.; Bradforth, S. E. New Insights into the Charge-Transfer-to-Solvent Spectrum of Aqueous Iodide: Surface versus Bulk. *J. Phys. Chem. Lett.* **2020**, *11* (5), 1656–1661. https://doi.org/10.1021/acs.jpclett.9b03857.

(4) Mizuno, H.; Oosterbaan, K. J.; Menzl, G.; Smith, J.; Rizzuto, A. M.; Geissler, P. L.; Head-Gordon, M.; Saykally, R. J. Revisiting the $\Pi\rightarrow\pi^*$ Transition of the Nitrite Ion at the Air/Water Interface: A Combined Experimental and Theoretical Study. *Chem. Phys. Lett.* **2020**, *751* (March), 137516. https://doi.org/10.1016/j.cplett.2020.137516.

(5) Barry, B. A. THE ROLE OF REDOX-ACTIVE AMINO ACIDS IN THE PHOTOSYNTHETIC WATER-OXIDIZING COMPLEX. *Photochem. Photobiol.* **1993**, *57* (1), 179–188. https://doi.org/10.1111/j.1751-1097.1993.tb02275.x.

(6) Niegowski, S. J. Destruction of Phenols by Oxidation of Ozone. *Ind. Eng. Chem.* **1953**, *45* (3), 632–634. https://doi.org/10.1021/ie50519a046.
(7) Sobolewski, A. L.; Domcke, W.; Dedonder-Lardeux, C.; Jouvet, C. Excited-State Hydrogen Detachment and Hydrogen Transfer Driven by Repulsive 1πσ* States: A New Paradigm for Nonradiative Decay in Aromatic Biomolecules. *Phys. Chem. Chem. Phys.* **2002**, *4* (7), 1093–1100. https://doi.org/10.1039/b110941n.
(8) Ashfold, M. N. R.; King, G. A.; Murdock, D.; Nix, M. G. D.; Oliver, T. A. A.; Sage, A. G. Πσ* Excited States in Molecular Photochemistry. *Phys Chem Chem Phys* **2010**, *12* (6), 1218–1238. https://doi.org/10.1039/B921706A.
(9) Iqbal, A.; Cheung, M. S. Y.; Nix, M. G. D.; Stavros, V. G. Exploring the Time-Scales of H-Atom Detachment from Photoexcited Phenol- h 6 and Phenol- d 5 : Statistical vs Nonstatistical Decay. *J. Phys. Chem. A* **2009**, *113* (29), 8157–8163. https://doi.org/10.1021/jp9031223.
(10) Riley, J. W.; Wang, B.; Woodhouse, J. L.; Assmann, M.; Worth, G. A.; Fielding, H. H. Unravelling the Role of an Aqueous Environment on the Electronic Structure and Ionization of Phenol Using Photoelectron Spectroscopy. *J. Phys. Chem. Lett.* **2018**, *9* (4), 678–682. https://doi.org/10.1021/acs.jpclett.7b03310.
(11) Harris, S. J.; Murdock, D.; Zhang, Y.; Oliver, T. A. A.; Grubb, M. P.; Orr-Ewing, A. J.; Greetham, G. M.; Clark, I. P.; Towrie, M.; Bradforth, S. E.; Ashfold, M. N. R. Comparing Molecular Photofragmentation Dynamics in the Gas and Liquid Phases. *Phys. Chem. Chem. Phys.* **2013**, *15* (18), 6567–6582. https://doi.org/10.1039/c3cp50756d.
(12) Zhang, Y.; Oliver, T. A. A.; Ashfold, M. N. R.; Bradforth, S. E. Contrasting the Excited State Reaction Pathways of Phenol and Para-Methylthiophenol in the Gas and Liquid Phases. *Faraday Discuss.* **2012**, *157*, 141–163. https://doi.org/10.1039/c2fd20043k.
(13) Oliver, T. A. A.; Zhang, Y.; Roy, A.; Ashfold, M. N. R.; Bradforth, S. E. Exploring Autoionization and Photoinduced Proton-Coupled Electron Transfer Pathways of Phenol in Aqueous Solution. *J. Phys. Chem. Lett.* **2015**, *6* (20), 4159–4164. https://doi.org/10.1021/acs.jpclett.5b01861.
(14) Sandler, I.; Nogueira, J. J.; González, L. Solvent Reorganization Triggers Photo-Induced Solvated Electron Generation in Phenol. *Phys. Chem. Chem. Phys.* **2019**, *21* (26), 14261–14269. https://doi.org/10.1039/C8CP06656F.

(15) Harkins, W. D.; Grafton, E. H. Monomolecular Films on Water: The Oriented Adsorption of Derivatives of Benzene. *J. Am. Chem. Soc.* **1925**, *47* (5), 1329–1335. https://doi.org/10.1021/ja01682a017.

(16) Filek, M.; Paluch, M.; Waligóra, B. Electrical Properties of the Monolayers of P-Phenol Derivatives. *J. Colloid Interface Sci.* **1982**, *89* (1), 166–169. https://doi.org/10.1016/0021-9797(82)90130-8.

(17) Hicks, J. M.; Kemnitz, K.; Eisenthal, K. B.; Heinz, T. F. Studies of Liquid Surfaces by Second Harmonic Generation. *J. Phys. Chem.* **1986**, *90* (4), 560–562. https://doi.org/10.1021/j100276a015.

(18) Tamburello-Luca, A. A.; Hébert, P.; Brevet, P. F.; Girault, H. H. Resonant-Surface Second-Harmonic Generation Studies of Phenol Derivatives at Air/Water and Hexane/Water Interfaces. *J Chem Soc Faraday Trans* **1996**, *92* (17), 3079–3085. https://doi.org/10.1039/FT9969203079.

(19) Kusaka, R.; Nihonyanagi, S.; Tahara, T. The Photochemical Reaction of Phenol Becomes Ultrafast at the Air–Water Interface. *Nat. Chem.* **2021**, 1–7. https://doi.org/10.1038/s41557-020-00619-5.

(20) Bhattacharyya, D.; Zhang, Y.; Elles, C. G.; Bradforth, S. E. Electronic Structure of Liquid Methanol and Ethanol from Polarization-Dependent Two-Photon Absorption Spectroscopy. *J. Phys. Chem. A* **2019**, *123* (27), 5789–5804. https://doi.org/10.1021/acs.jpca.9b04040.

(21) Elles, C. G.; Rivera, C. A.; Zhang, Y.; Pieniazek, P. A.; Bradforth, S. E. Electronic Structure of Liquid Water from Polarization-Dependent Two-Photon Absorption Spectroscopy. *J. Chem. Phys.* **2009**, *130* (8), 084501. https://doi.org/10.1063/1.3078336.

(22) Plimpton, S. Fast Parallel Algorithms for Short-Range Molecular Dynamics. *J. Comput. Phys.* **1995**, *117* (1), 1–19. https://doi.org/10.1006/jcph.1995.1039.

(23) Spasic, A.; Serafini, J.; Mathews, D. H. The Amber Ff99 Force Field Predicts Relative Free Energy Changes for RNA Helix Formation. *J. Chem. Theory Comput.* **2012**, *8* (7), 2497–2505. https://doi.org/10.1021/ct300240k.

(24) Andersen, H. C. Rattle: A "Velocity" Version of the Shake Algorithm for Molecular Dynamics Calculations. *J. Comput. Phys.* **1983**, *52* (1), 24–34. https://doi.org/10.1016/0021-9991(83)90014-1.

(25) Kamberaj, H.; Low, R. J.; Neal, M. P. Time Reversible and Symplectic Integrators for Molecular Dynamics Simulations of Rigid Molecules. *J. Chem. Phys.* **2005**, *122* (22), 224114. https://doi.org/10.1063/1.1906216.

(26) Scheiner, S.; Kar, T.; Pattanayak, J. Comparison of Various Types of Hydrogen Bonds Involving Aromatic Amino Acids. *J. Am. Chem. Soc.* **2002**, *124* (44), 13257–13264. https://doi.org/10.1021/ja027200q.

(27) Kusaka, R.; Ishiyama, T.; Nihonyanagi, S.; Morita, A.; Tahara, T. Structure at the Air/Water Interface in the Presence of Phenol: A Study Using Heterodyne-Detected Vibrational Sum Frequency Generation and Molecular Dynamics Simulation. *Phys. Chem. Chem. Phys.* **2018**, *20* (5), 3002–3009. https://doi.org/10.1039/C7CP05150F.

(28) Schirmer, J. Beyond the Random-Phase Approximation: A New Approximation Scheme for the Polarization Propagator. *Phys. Rev. A* **1982**, *26* (5), 2395–2416. https://doi.org/10.1103/PhysRevA.26.2395.

(29) Schirmer, J.; Trofimov, A. B. Intermediate State Representation Approach to Physical Properties of Electronically Excited Molecules. *J. Chem. Phys.* **2004**, *120* (24), 11449–11464. https://doi.org/10.1063/1.1752875.

(30) Shao, Y.; Gan, Z.; Epifanovsky, E.; Gilbert, A. T. B.; Wormit, M.; Kussmann, J.; Lange, A. W.; Behn, A.; Deng, J.; Feng, X.; Ghosh, D.; Goldey, M.; Horn, P. R.; Jacobson, L. D.; Kaliman, I.; Khaliullin, R. Z.; Kuś, T.; Landau, A.; Liu, J.; Proynov, E. I.; Rhee, Y. M.; Richard, R. M.; Rohrdanz, M. A.; Steele, R. P.; Sundstrom, E. J.; Woodcock, H. L.; Zimmerman, P. M.; Zuev, D.; Albrecht, B.; Alguire, E.; Austin, B.; Beran, G. J. O.; Bernard, Y. A.; Berquist, E.; Brandhorst, K.; Bravaya, K. B.; Brown, S. T.; Casanova, D.; Chang, C. M.; Chen, Y.; Chien, S. H.; Closser, K. D.; Crittenden, D. L.; Diedenhofen, M.; Distasio, R. A.; Do, H.; Dutoi, A. D.; Edgar, R. G.; Fatehi, S.; Fusti-Molnar, L.; Ghysels, A.; Golubeva-Zadorozhnaya, A.; Gomes, J.; Hanson-Heine, M. W. D.; Harbach, P. H. P.; Hauser, A. W.; Hohenstein, E. G.; Holden, Z. C.; Jagau, T. C.; Ji, H.; Kaduk, B.; Khistyaev, K.; Kim, J.; Kim, J.; King, R. A.; Klunzinger, P.; Kosenkov, D.; Kowalczyk, T.; Krauter, C. M.; Lao, K. U.; Laurent, A. D.; Lawler, K. V.; Levchenko, S. V.; Lin, C. Y.; Liu, F.; Livshits, E.; Lochan, R. C.; Luenser, A.; Manohar, P.; Manzer, S. F.; Mao, S. P.; Mardirossian, N.; Marenich, A. V.; Maurer, S. A.; Mayhall, N. J.; Neuscamman, E.; Oana, C. M.; Olivares-Amaya, R.; Oneill, D. P.; Parkhill, J. A.; Perrine, T. M.; Peverati, R.; Prociuk, A.; Rehn, D.

R.; Rosta, E.; Russ, N. J.; Sharada, S. M.; Sharma, S.; Small, D. W.; Sodt, A.; Stein, T.; Stück, D.; Su, Y. C.; Thom, A. J. W.; Tsuchimochi, T.; Vanovschi, V.; Vogt, L.; Vydrov, O.; Wang, T.; Watson, M. A.; Wenzel, J.; White, A.; Williams, C. F.; Yang, J.; Yeganeh, S.; Yost, S. R.; You, Z. Q.; Zhang, I. Y.; Zhang, X.; Zhao, Y.; Brooks, B. R.; Chan, G. K. L.; Chipman, D. M.; Cramer, C. J.; Goddard, W. A.; Gordon, M. S.; Hehre, W. J.; Klamt, A.; Schaefer, H. F.; Schmidt, M. W.; Sherrill, C. D.; Truhlar, D. G.; Warshel, A.; Xu, X.; Aspuru-Guzik, A.; Baer, R.; Bell, A. T.; Besley, N. A.; Chai, J. Da; Dreuw, A.; Dunietz, B. D.; Furlani, T. R.; Gwaltney, S. R.; Hsu, C. P.; Jung, Y.; Kong, J.; Lambrecht, D. S.; Liang, W.; Ochsenfeld, C.; Rassolov, V. A.; Slipchenko, L. V.; Subotnik, J. E.; Van Voorhis, T.; Herbert, J. M.; Krylov, A. I.; Gill, P. M. W.; Head-Gordon, M. Advances in Molecular Quantum Chemistry Contained in the Q-Chem 4 Program Package. *Mol. Phys.* **2015**, *113* (2), 184–215. https://doi.org/10.1080/00268976.2014.952696.

(31) Moad, A. J.; Simpson, G. J. A Unified Treatment of Selection Rules and Symmetry Relations for Sum-Frequency and Second Harmonic Spectroscopies. *J. Phys. Chem. B* **2004**, *108* (11), 3548–3562. https://doi.org/10.1021/jp035362i.

(32) Lin, C.-K.; Hayashi, M.; Lin, S. H. Theoretical Formulation and Simulation of Electronic Sum-Frequency Generation Spectroscopy. *J. Phys. Chem. C* **2013**, *117* (45), 23797–23805. https://doi.org/10.1021/jp407881a.

(33) Gerrard, D. L. L.; Maddams, W. F. F. Solvent Effects in u.v. Absorption Spectra. I. Phenol in Cyclohexane Ethanol Mixtures. *Spectrochim. Acta Part Mol. Spectrosc.* **1978**, *34* (12), 1205–1211. https://doi.org/10.1016/0584-8539(78)80081-6.

(34) Fornander, L. H.; Feng, B.; Beke-Somfai, T.; Nordén, B. UV Transition Moments of Tyrosine. *J. Phys. Chem. B* **2014**, *118* (31), 9247–9257. https://doi.org/10.1021/jp5065352.